

Lagrangian transport and chaotic advection in three-dimensional laminar flows

Michel Speetjens

Energy Technology & Fluid Dynamics
Eindhoven University of Technology
PO Box 513, 5600 MB Eindhoven
The Netherlands
m.f.m.speetjens@tue.nl

Guy Metcalfe

School of Engineering
Swinburne University of Technology
Hawthorn VIC 3122
Australia
gmetcalfe@swin.edu.au

Murray Rudman

Mechanical & Aerospace Engineering
Monash University
Clayton VIC 3800
Australia
murray.rudman@monash.edu

Transport and mixing of scalar quantities in fluid flows is ubiquitous in industry and Nature. Turbulent flows promote efficient transport and mixing by their inherent randomness. Laminar flows lack such a natural mixing mechanism and efficient transport is far more challenging. However, laminar flow is essential to many problems and insight into its transport characteristics of great importance. Laminar transport, arguably, is best described by the Lagrangian fluid motion (“advection”) and the geometry, topology and coherence of fluid trajectories. Efficient laminar transport being equivalent to “chaotic advection” is a key finding of this approach.

The Lagrangian framework enables systematic analysis and design of laminar flows. However, the gap between scientific insights into Lagrangian transport and technological applications is formidable primarily for two reasons. First, many studies concern two-dimensional (2D) flows yet the real world is three dimensional (3D). Second, Lagrangian transport is typically investigated for idealised flows yet practical relevance requires studies on realistic 3D flows.

The present review aims to stimulate further development and utilisation of know-how on 3D Lagrangian transport and its dissemination to practice. To this end 3D practical flows are categorised into canonical problems. First, to expose the diversity of Lagrangian transport and create awareness of its broad relevance. Second, to enable knowledge transfer both within and between scientific disciplines. Third, to reconcile practical flows with fundamentals on Lagrangian transport and chaotic advection. This may be a first incentive to structurally integrate the “Lagrangian mindset” into the analysis and design of 3D practical flows.

1 Introduction

The scope of this review is transport and mixing of scalar quantities such as additives, chemical species, heat and nutrients in realistic three-dimensional (3D) fluid flows under *laminar flow conditions*. This flow regime sets in for a Reynolds number $Re = UL/\nu$ below the threshold of turbulence and is common to many systems and processes in industry and Nature due to high fluid viscosities ν , small length scales L and/or low velocities U . Industrial examples are found abundantly in fluids processing and span a wide range of scales from conventional food or polymer processing [1, 2, 3, 4, 5] to emerging technologies as e.g process intensification and micro-fluidics [6, 7, 8, 9, 10, 11, 12, 13, 14, 15, 16, 17, 18, 19]. Further technological applications include (at first glance) less obvious systems as Darcy representations of flow and transport in porous media, relevant e.g. for *in situ* mining, enhanced oil recovery, geothermal energy extraction or groundwater remediation [20, 21, 22, 23, 24, 25], as well as continuum descriptions of granular flows [26, 27, 28].

Scalar transport in laminar flows is also key to many systems beyond industry and technology. Consider, for example, transport of oxygen or pathogens in physiological flows [29, 30, 31, 32, 33, 34] and geophysical flow problems as plate tectonics driven by mantle convection [35] and dispersion of nutrients or spreading of pollutants in oceans [36, 37, 38, 39].¹

Scalar transport in flows generically involves an interplay of the physical motion of the fluid (“advection”) with

¹Oceanographic flows typically are turbulent yet often admit approximation by Euler flows or spatio-temporal averaged flows obtained via e.g. RANS or LES. Such approximations are *deterministic* in the sense of being robustly reproducible and thus effectively behave as laminar flows. The underlying turbulent flows, on the other hand, are *stochastic* in being realisations from an ensemble of states and thus are inherently unpredictable.

molecular mechanisms as diffusion and chemical reactivity. Advection is, given its pivotal role in scalar transport, the focus of this review and for laminar flow conditions, arguably, best viewed from the Lagrangian perspective of the motion of individual fluid parcels. The stochastic nature of *turbulent* flows gives rise to Brownian motion of fluid parcels that typically admits expression as an effective diffusion (“turbulent diffusion”) [40]. This is absent in *laminar* flows and, in consequence, the structure of Lagrangian fluid trajectories is essential to the transport characteristics. Moreover, the connection between Eulerian velocity field and Lagrangian motion may be non-trivial and counter-intuitive in that extremely tangled fluid trajectories can coexist with very simple velocity fields. Hence transport studies in laminar flows should on account of these fundamental characteristics concentrate on the *Lagrangian* transport of fluid parcels.

The most striking disconnect between flow and Lagrangian transport is the intriguing phenomenon of “chaotic advection” that, in a “rough-and-ready” definition, concerns the rapid deformation of material fluid elements into highly ramified and filamented structures. This promotes efficient transport reminiscent of the rapid dispersion by stochastic fluctuations in turbulent flows and thus renders chaotic advection the laminar counterpart to turbulent mixing. Chaotic advection has first been demonstrated in the seminal study of Hassan Aref in the early 1980s [41] and can occur for very general (and often deceptively simple) flows [42, 43].

Consider as an illustration of the versatility of Lagrangian transport phenomena a few examples in completely different settings. Fig. 1(a) gives 3D trajectories (visualised by fluorescent tracer particles) in the steady flow inside a cylindrical container stirred by an impeller [44]. The system serves as laboratory model for industrial batch mixers and the Lagrangian transport – in particular the accomplishment of global 3D chaotic advection – evidently is crucial to the functionality and performance of such devices. The disordered nature of the trajectories suggests chaos yet dedicated Lagrangian analysis is necessary to conclusively establish this. The web of trajectories, by virtue of continuity and mass conservation, namely contains hidden “pathways” and coherent structures that geometrically guide the transport. Relevant here are in particular toroidal (i.e. donut-shaped) material surfaces that may emerge around the impeller axis, which, if indeed occurring, act as barriers to chaotic trajectories and thus compromise the mixing performance. Such structures cannot be inferred from the velocity field nor are directly visible, meaning they elude conventional analyses and engineering. Hence many mixer designs and operating conditions likely are sub-optimal.

A non-technological example is found in physiology. Fig. 1(b) gives the 3D Lagrangian trajectories inside a human aortic aneurysm (balloon-like malformations of blood vessels) visualised by *in vivo* measurements using phase-contrast cardio-vascular magnetic-resonance imaging [45]. This reveals vortical structures (indicated by open arrows) akin to the batch mixer in Fig. 1(a) driven by the main bloodstream (closed arrows) and thus suggests comparable (chaotic) dynamics due to a similar “hidden organisation”

of the fluid trajectories into chaotic tangles and toroidal barriers. However, unlike mixers, chaotic advection has a potentially adverse impact by tending to entrap blood-borne platelets and substances implicated in thrombosis and atherosclerosis [29]. Hence Lagrangian transport is a key factor in these vascular diseases and investigation of the pathways and coherent structures embedded in the fluid trajectories may shed more light on their origin and causes.

A biological counterpart exists in the cilia-driven flow at polyps in coral reefs visualised (for polyp explants) by fluorescent particles in Fig. 1(c) [46,47,48]. The “stirring” by the cilia aims, similar to the batch mixers, at creating favourable transport conditions near the coral surface for the benefit of photosynthesis and suppression of adverse effects as carbon fixation and pathogen invasion. However, *what* conditions are in fact “favourable” (this must not necessarily be chaos; transport barriers as mentioned before may very well benefit these processes) and *how* Nature accomplishes this remains unclear. Lagrangian transport analyses may again contribute to the understanding of these phenomena.

The examples in Fig. 1 give a first flavour of the richness and universality of Lagrangian transport and demonstrate that seemingly different systems have much more in common than meets the eye. The fluid trajectories are namely organised into elementary “building blocks” that form the network of transport pathways and barriers according to general “rules” depending only secondarily on the particulars of the flow (forcing). This implies unifying structures that transcend specific flow configurations (as well as scientific and engineering disciplines) and thus enable a universal strategy for analysis of Lagrangian transport by the geometry, topology and coherence of fluid trajectories.

The relevance and usefulness of a (cross-disciplinary) unified Lagrangian approach towards laminar transport is evident from the above. Moreover, efficient laminar transport being synonymous to chaotic advection is in itself recognised in the fluid-dynamics community [43]. However, the gap between scientific research and insights into (chaotic) Lagrangian transport and technological applications is still formidable primarily for two reasons. *First*, scientific studies on Lagrangian transport to date mainly concern two-dimensional (2D) flows. The real world is three dimensional (3D), on the other hand, yet 3D Lagrangian transport remains elusive. The additional spatial degree of freedom greatly increases the dynamical richness and geometric complexity and a comprehensive theoretical and conceptual framework, in contrast with the basically complete picture of 2D Lagrangian transport, is therefore still non-existent in 3D [49, 43]. *Second*, Lagrangian transport is typically investigated via theoretical and computational studies and often concerns idealised flow situations that are difficult (or even impossible) to create in laboratory experiments. Dedicated experimental studies on Lagrangian transport, crucial for (conclusively) establishing physical meaningfulness and practical relevance of results, remain scarce, though. The only systematic technological application to date exists in a subclass of industrial and micro-fluidic mixers that admit reconciliation with 2D flows and the associated theory

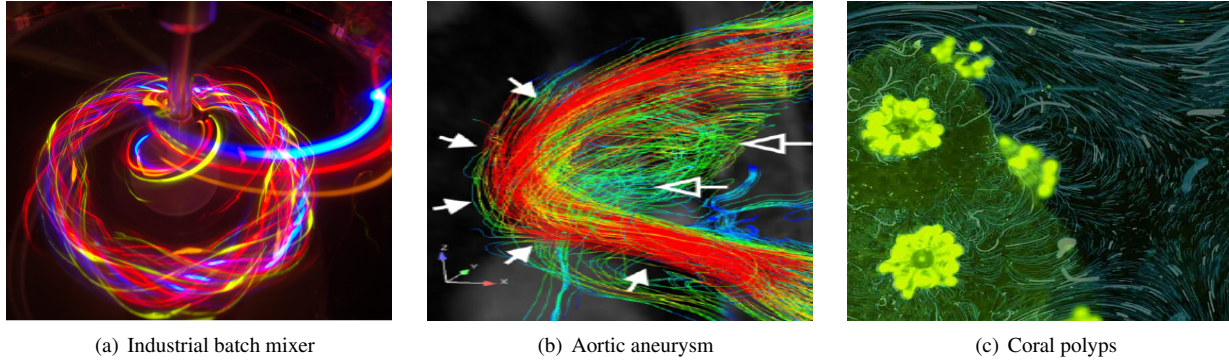


Fig. 1. Instances of Lagrangian (chaotic) transport in 3D flows: (a) impeller-driven (chaotic) trajectories in laboratory model for industrial batch mixers visualised by fluorescent tracers (reproduced from [44]); (b) vortical (chaotic) trajectories in human aortic aneurysm (open arrows) driven by main aortic flow (closed arrows) visualised by *in vivo* phase-contrast magnetic-resonance imaging (reproduced from [45]); (c) vortical (chaotic) trajectories in cilia-driven flow around (explants of) coral polyps visualised by fluorescent tracers (reproduced from [46]).

[50]. However, dissemination even of the proven principle of chaotic advection for such devices to the practicing engineering community remains a challenge.

The growing importance and urgency to close the gap between fundamentals and applications motivates this review. Its principal aim is to stimulate further utilisation and development of know-how on 3D Lagrangian transport for technological applications and its dissemination to practitioners in industry and beyond. To this end 3D practical flows to which (non-)chaotic Lagrangian transport is essential are categorised into canonical problems so as to (i) identify analogies and similarities, (ii) establish connections with configurations in fundamental 3D Lagrangian studies, (iii) outline a unified Lagrangian framework for 3D transport studies and (iv) isolate challenges specifically regarding applications. The focus will be primarily on flows and applications in industry and technology with excursions into life sciences and on occasion beyond. Furthermore, the canonical flow problems will be exemplified and represented by experimental(ly-realisable) cases to ensure practical relevance and robustness of phenomena.

The Lagrangian framework and the concept of chaotic advection have, expanding on Aref’s pioneering work [41], been developed in the 1980s and 1990s mainly for 2D time-periodic flows (as approximations for inline industrial mixers) using dynamical-systems methods as Hamiltonian mechanics and vector-field topology [51, 52, 53, 54, 55, 56, 57]. Two important extensions of the Lagrangian framework in the early 2000s include granular-media flows that admit a continuum description [26,27] and deterministic descriptions of large-scale oceanographic flows [36, 37]. Recent and ongoing efforts focus on generalisations of the Lagrangian approach to aperiodic and finite-time flows [58, 59] and the interaction between (chaotic) advection and other transport physics (e.g. diffusion, reaction, propulsion, particle inertia) [60, 43, 61].

The present review expands on the above body of work by explicitly positioning this in the context of 3D practical flows and is organised as follows. Sec. 2 introduces the general concepts and methods of Lagrangian transport studies.

Sec. 3 categorises 3D practical flows into canonical problems in order to, first, identify analogies and similarities and, second, establish connections with fundamental 3D Lagrangian studies. Sec. 4 outlines a unified Lagrangian framework for 3D transport studies by reconciling the flow categories and canonical problems with theory and fundamentals on Lagrangian transport. Sec. 5 investigates the degree of dissemination and technological utilisation of the concept of chaotic advection via a survey on relevant patents and commercial applications. Concluding remarks including an overview of challenges exposed by this review are in Sec. 6.

2 Lagrangian approach to transport and mixing

In the absence of chemical reactions, transport of a scalar quantity C in fluid flows occurs by an interplay of two physical mechanisms: advection by the fluid motion and molecular diffusion along concentration gradients (Fig. 2).² The corresponding Eulerian evolution is governed by the advection-diffusion equation

$$\frac{dC}{dt} = \frac{\partial C}{\partial t} + \vec{u} \cdot \vec{\nabla} = \frac{1}{Pe} \vec{\nabla}^2 C, \quad C(\vec{x}, 0) = C_0(\vec{x}), \quad (1)$$

with \vec{u} the velocity field and $Pe = UL/\alpha$ the well-known Péclet number. Here U and L are characteristic velocity and length scales, respectively, and α is the scalar diffusivity. The present review concerns systems with $Pe \gg 1$, which holds for many practical systems, meaning that scalar transport is dominated by advection and (1) effectively reduces to $dC/dt = 0$. Thus scalar C is passively advected by fluid parcels, i.e. $C(\vec{x}(t)) = C(\vec{x}_0)$, with $\vec{x}(t)$ the current parcel position governed by the kinematic equation

$$\frac{d\vec{x}}{dt} = \vec{u}(\vec{x}(t), t) \quad \Rightarrow \quad \vec{x}(t) = \vec{\Phi}_t(\vec{x}_0), \quad (2)$$

²Advection and diffusion of heat is usually denoted “convection” and “conduction”, respectively.

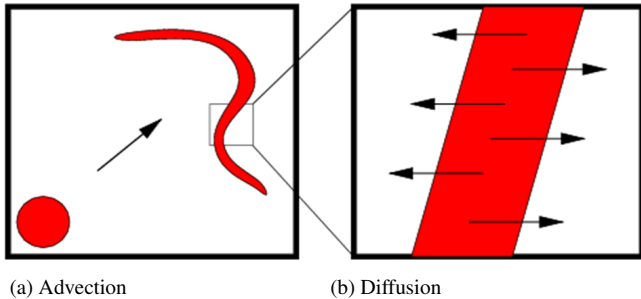


Fig. 2. Transport of scalar quantity C (red) in fluid flows by interplay of advection of material region (left) and diffusion across its interface (right). Arrows indicate transport by respective mechanisms.

and flow $\tilde{\Phi}_t$ its formal solution describing the Lagrangian motion of a parcel released at $\bar{x}(0) = \bar{x}_0$. Hence, $dC/dt = 0$ and $d\bar{x}/dt = \bar{u}$ are the equivalent Eulerian and Lagrangian representations of scalar advection. The fluid is assumed incompressible, implying solenoidal flow ($\nabla \cdot \bar{u} = 0$), which has fundamental ramifications for Lagrangian transport.

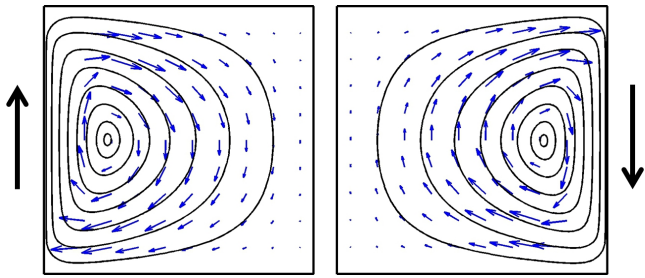
The exposition hereafter adopts the Lagrangian perspective on scalar transport with kinematic equation (2) as its cornerstone. The latter defines a generically nonlinear dynamical system and enables investigation of advective transport by the geometry and topology of the Lagrangian fluid trajectories, i.e. the ‘‘Lagrangian flow topology’’, which is composed of elementary structures denoted ‘‘Lagrangian coherent structures’’ (LCSs) [52, 59, 43].³ The nature of LCSs is described and illustrated by the time-periodic flow

$$\bar{u}(\bar{x}, t + pT) = \bar{u}(\bar{x}, t), \quad (3)$$

with T the period time and p the period, in a 2D cavity driven by the alternate steady motion of the left and right walls. Fig. 3 gives the translation direction of each wall and the corresponding velocity vectors and streamline patterns obtained by numerical solution of the non-dimensional Navier-Stokes equations. Note that the steady flow during the second half of each period is a reorientation of that of the first half. This composition of time-periodic flows from reorientations of a steady base flow is common practice both in scientific studies on mixing and industrial applications.

The scalar advection illustrated in Fig. 2(a) may take place in two fundamentally different ways: non-chaotic advection versus chaotic advection. This is demonstrated in Fig. 4 for the advection of blue and red material elements in the 2D lid-driven cavity, revealing a dramatic difference in behaviour. The blue element undergoes a moderate shear-like deformation that yields (at most) linear stretching of the interface. This signifies *non-chaotic* advection. The red element, on the other hand, exhibits strong deformation due to repeated stretching and folding, resulting in exponential elongation of the interface. This is the hallmark of *chaotic* advection [52].

³Term ‘‘LCS’’ originally denotes specific classes of coherent structures in aperiodic flows [59]. Here it denotes coherent structures in general.



(a) First half of each period p . (b) Second half of each period p .

Fig. 3. Time-periodic 2D lid-driven cavity flow $\bar{u}(\bar{x}, t + pT) = \bar{u}(\bar{x}, t)$ due to alternate steady translation of left and right wall during first ($0 \leq t' \leq T/2$) and second ($T/2 \leq t' \leq T$) half, respectively, of each period p with time interval $0 \leq t' \leq T$. Heavy black arrows indicate translation direction; blue arrows and closed curves indicate velocity vectors and streamlines, respectively.

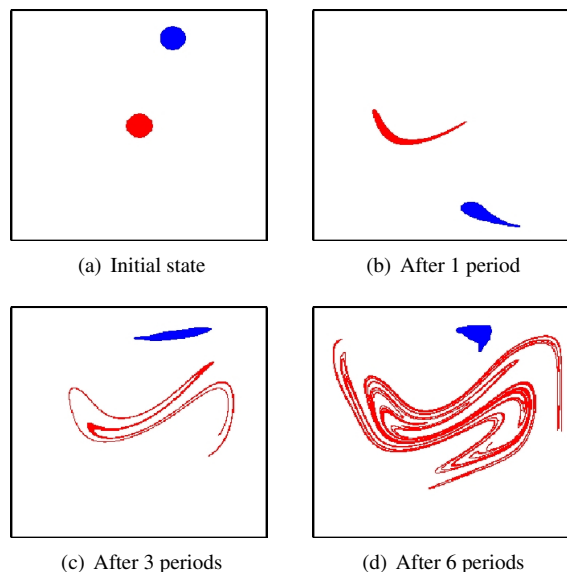


Fig. 4. Non-chaotic versus chaotic advection illustrated by evolution of blue and red material elements, respectively, in 2D time-periodic lid-driven cavity.

Chaotic advection promotes efficient mixing in laminar flows by (i) rapid global scalar distribution (Fig. 4) and (ii) creation of large ‘‘working areas’’ and steep gradients for diffusion (Fig. 2(b)) by exponential interface stretching. Hence, it is the laminar counterpart to efficient mixing by turbulent diffusion in turbulent flows. However, unlike turbulence, chaotic advection is not a natural mixing mechanism of the flow and in fact can be challenging to accomplish. This is a direct consequence of the fundamental disconnect between the Eulerian velocity field and the Lagrangian transport in laminar flows, allowing complex fluid trajectories to coexist with simple flow fields. Compare to this end the simple step-wise flows in Fig. 3 with the intricate Lagrangian advection in Fig. 4. Thus the Lagrangian approach is essential to describe and understand scalar transport in laminar flows.

The Lagrangian flow topology underlying scalar advec-

tion in time-periodic flows (as the lid-driven cavity) admits visualisation by so-called “stroboscopic maps” of tracer particles. Such maps visualise the motion of a tracer released at \vec{x}_0 via the sequence of positions at the end of each period, i.e.

$$\mathcal{S}(\vec{x}_0) = \{\vec{x}_0, \vec{\Phi}_T(\vec{x}_0), \vec{\Phi}_T^2(\vec{x}_0), \dots\}, \quad (4)$$

with

$$\vec{x}_p = \vec{\Phi}_T(\vec{x}_{p-1}) = \vec{\Phi}_T^p(\vec{x}_0), \quad (5)$$

the period-wise mapping, as if illuminated by a stroboscope. This is a common technique also often referred to as “Poincaré sectioning” [43].

Fig. 5(a) gives the Lagrangian flow topology visualised by the combined stroboscopic maps (black dots) of a number of tracer particles released on the vertical line $x = 0.5$. This exposes a first kind of LCSs, viz. islands (white circular patches), embedded in “chaotic seas” (densely filled regions). Such islands systematically return to their initial position after a given number of periods and act as transport barriers by entrapping material regions during their excursion through the flow domain. The blue element in Fig. 4 is trapped in the island near the top wall that cyclically returns to its initial position after 3 periods through intermediate positions at the island near the bottom and left walls after the first and second periods, respectively. The centres of the islands are periodic points, i.e. material points cyclically returning to the initial position after $p \geq 1$ periods following

$$\vec{x}_0 = \vec{\Phi}_T^p(\vec{x}_0), \quad (6)$$

commonly denoted *elliptic points* (Sec. 4.1) [52]. Periodic points for $p > 1$ always emerge as sets of p material points

$$\mathcal{X}_p(\vec{x}_0) = \{\vec{x}_0, \vec{\Phi}_T(\vec{x}_0), \dots, \vec{\Phi}_T^{p-1}(\vec{x}_0)\}, \quad (7)$$

through which each element of \mathcal{X}_p cyclically progresses in the course of time.

A second kind of LCSs in Fig. 5(a) concerns structures termed “manifolds”, which are associated with another type of periodic points known as *hyperbolic points* (Sec. 4.1) [52]. At each hyperbolic point (marked with a cross in Fig. 5(a)), a stable (blue) and unstable (red) manifold exists that wind their way through the chaotic sea. (The type of a periodic point is determined by the local deformation characteristics; Sec. 4.1.) These manifolds are “special” material curves that delineate the principal transport directions in this sea and thus dictate the chaotic advection [43]. The red element in Fig. 4 coincides with the chaotic sea and its chaotic transport – characterised by the repeated stretching and folding – is determined by the unstable manifold. Figs. 5(b-d) demonstrate this by the rapid convergence of the red element on the unstable manifold (coloured in grey); essentially the same

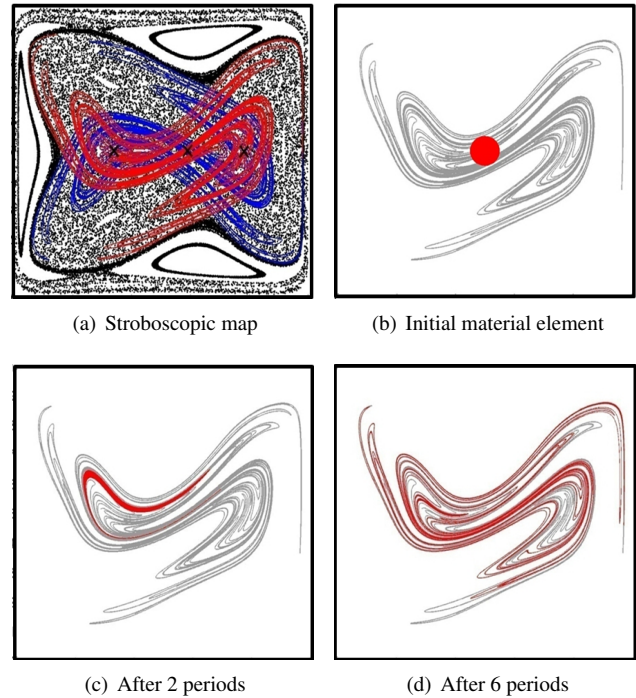


Fig. 5. Typical Lagrangian flow topology and transport in 2D time-periodic flows demonstrated by lid-driven cavity: (a) stroboscopic map including stable (blue) and unstable (red) manifolds of chaotic sea; (b-c) convergence of material element (red) on asymptotic mixing pattern demarcated by unstable manifold (grey).

convergence occurs for *any* material element released in the chaotic sea, exposing the unstable manifold as its fundamental mixing pattern (or “mixing template” [43]).⁴

Solenoidal 2D velocity fields ($\vec{\nabla} \cdot \vec{u} = 0$) exclusively admit elliptic/hyperbolic points and associated islands/manifolds [52]. Hence these LCS are the fundamental “building blocks” of Lagrangian flow topologies of 2D incompressible flows. Moreover, solenoidality in 2D imposes a *Hamiltonian structure* on kinematic equation (2) that makes unsteadiness a necessary (yet not sufficient) condition for chaotic advection in 2D flows. This Hamiltonian structure and its ramifications for the dynamics are detailed in Sec. 4.2. Time-periodic 2D flows – here represented by the lid-driven cavity – meet this requirement and their Lagrangian flow topologies therefore typically consist of arrangements of islands and chaotic seas as in Fig. 5(a) [43].

The Lagrangian flow topology of 3D flows (both steady and unsteady) admits an essentially similar decomposition into distinct LCSs yet encompasses a larger set of such “building blocks” and corresponding interaction scenarios. Furthermore, the beforementioned Hamiltonian structure of kinematic equation (2) is retained only for certain conditions (refer to Sec. 4.3, Sec. 4.4 and Sec. 4.6). Thus 3D flows in general exhibit much greater topological complexity and, in consequence, far richer dynamics than their 2D counter-

⁴Refer to www.youtube.com/watch?v=B3dwryNgPXY for an experimental demonstration of chaotic advection and the emergence of a mixing pattern due to the unstable manifold.

parts. LCSs enable systematic and rigorous exposure of this topology and associated dynamics and therefore are indispensable for in-depth transport studies and characterisations. Furthermore, LCSs, given their robustness, can (in principle) be instrumentalised for specific purposes. Efficient mixing requires systematic “destruction” of transport barriers as the islands in 2D; containment of polluted groundwater, on the other hand, requires establishment of such barriers in the subsurface flow. This can (basically) be realised by appropriate flow conditions. [Sec. 3](#) below reconciles the Lagrangian framework and the utilisation of LCSs as “tools” for analysis, characterisation and engineering 3D practical flows to which Lagrangian transport is essential.

3 Lagrangian transport in 3D practical flows

3.1 Introduction

The examples in [Fig. 1](#) clearly demonstrate the diversity and relevance of 3D Lagrangian transport yet applications of concepts and insights remain limited due to the still formidable gap between theory and practice for reasons mentioned in [Sec. 1](#). The only systematic technological application is found in the subclass of industrial and micro-fluidic mixers that, for “proper” conditions, admit reconciliation with 2D flows and the associated theory ([Sec. 3.2](#)). Julio Ottino and co-workers laid the groundwork for mixing technology based on Lagrangian chaos in such 2D analogons in the late 1980s (resulting in his classical textbook [52]) and the framework thus developed has since found frequent application in engineering sciences [62, 63, 50, 64, 6, 65, 7, 66, 67, 9, 13, 68, 16, 69, 70, 71, 72, 73]. The Ottino group extended this framework to granular flows that behave as a continuum [26, 27, 28].

Employment of the Lagrangian framework for transport studies beyond industry and technology occurs primarily in the geophysical sciences. Large-scale oceanographic and atmospheric flows, due to their quasi-2D nature, namely also connect well with existing 2D theory [36, 37, 38, 39]. Development of Lagrangian methods specifically for aperiodic flows is in fact strongly motivated by such systems [74, 59, 75].

Dissemination of the above chaos-based mixing technology to the practicing engineering community poses a major challenge in its own right. Many recent handbooks on fluids processing, despite overwhelming evidence of its crucial role in (at least) inline mixers, mention chaotic advection only perfunctorily and continue to rely on properties of the Eulerian velocity field⁵ or standard metrics as the “coefficient of variation” (CoV) [76, 77, 5, 78].⁶ Two leading manufacturers

of static mixers, viz. Sulzer AG (Winterthur, Switzerland) and Chemineer (Dayton, USA), still heavily lean on the CoV to design and optimise their Sulzer SMX and Kenics KMX-V mixers, respectively.⁷ Similarly, the dedicated Sulzer CFD tool for laminar mixing adopts the CoV as mixing measure and functionalities for mixing diagnostics (other than visual inspection of particle paths) are absent altogether in the popular commercial CFD package ANSYS-FLUENT [81, 82].

Development and design by Lagrangian concepts enables technological leaps, though. Consider as a case in point the Rotated Arc Mixer (RAM) to be introduced in [Sec. 3.2](#). The RAM is to date the only commercially-available industrial mixer that from its inception is designed entirely on the basis of scientific insights into Lagrangian transport and the notion of chaotic advection ([Sec. 5.2.3](#)). This sound scientific basis allows it to substantially outperform conventional inline mixers both in energy consumption and mixing quality ([Sec. 5.2.3](#)). A survey of such “commercialisation” of chaos-based mixing technology is given in [Sec. 5](#). This includes the above Kenics mixer, which has been developed well before the advent of the concept of chaotic advection and thus is an indirect “commercialisation” of chaos ([Sec. 5.2.1](#)).

Application of Lagrangian concepts has similar potential for technological development in other (industrial) fields as well as in non-technological disciplines as life sciences. The physiological and biological examples in [Fig. 1](#) clearly highlight the central role of Lagrangian transport in such processes and the inherent need for LCS-based analyses to expose the underlying mechanisms. Said fields and disciplines may thus greatly benefit from a Lagrangian ansatz.

One of the key aims of this review is to lay the groundwork for describing and analysing transport and mixing in 3D practical flows by the Lagrangian ansatz. To this end, the following (heuristic) categorisation of such flows into canonical problems is adopted:

- flows in ducts ([Sec. 3.2](#));
- flows in containers ([Sec. 3.3](#));
- flows in drops ([Sec. 3.4](#));
- flows in webs ([Sec. 3.5](#)).

This hinges on the fact that analogies and similarities exist between seemingly different problems and thus provides a framework that enables (i) connection with configurations in fundamental studies on 3D Lagrangian transport, (ii) development of generic strategies and methods utilising Lagrangian concepts and (iii) isolation of challenges specifically regarding applications. Moreover, reduction to canonical problems promotes cross-fertilisation and multidisciplinary. The batch mixer and aneurysm in [Fig. 1](#) e.g. both concern transport in containers ([Sec. 3.3](#)) and transport within blood vessels is similar to that in inline micro-mixers ([Sec. 3.2](#)). Such analogies may enable application of mixing technology to cardio-vascular research and treatment.

⁵This may lead to erroneous results. A common misconception is e.g. that vortices imply efficient mixing. Reconsider to this end the lid-driven cavity. The flow consists of two alternating vortices ([Fig. 3](#)) yet mixing is inefficient ([Fig. 4](#)) due to islands in the Lagrangian flow topology ([Fig. 5\(a\)](#)).

⁶The CoV is in essence the “intensity of segregation” introduced by Danckwerts in the early 1950s [79]. An important shortcoming is arbitrariness of the cell size to determine the scalar concentration, which may cause non-physical effects as artificial diffusion and thus yield misleading results [80]. More sophisticated measures seek to overcome this yet their practical utilisation is scarce to non-existent [43].

⁷Refer to brochures “Mixing and Reaction Technology” (sulzer.com) and “Kenics KMX-V Static Mixer” (chemineer.com).

3.2 Flow in ducts

3.2.1 General configuration

Flows in ducts are assumed *periodic* in space unless stated otherwise. This assumption makes these problems tractable by allowing representation of the complete system by a periodic subsection and is a valid approximation in important industrial devices as the beforementioned inline mixers. Using this approximation, such periodic duct flows consist of a duct of infinite length and (in principle) arbitrary cross-section composed of repeated duct segments of length L . Each duct segment p accommodates a 3D steady flow that is a periodic repetition of that in the first segment $p = 1$, i.e.

$$\vec{u}(x, y, z + pL) = \vec{u}(x, y, z), \quad (8)$$

rendering the duct flow the spatially-periodic counterpart to the time-periodic flow (3). The duct segments are, in turn, partitioned into N axial “cells” of length $\Delta = L/N$. Each cell k accommodates a 3D steady flow that is a reorientation of flow \vec{v} in the first cell $k = 1$, i.e.

$$\vec{u}(r, \theta, z + k\Delta) = \vec{v}(r, \theta - \Theta_R(z), z), \quad (9)$$

with axial reorientation following

$$\Theta_R(z) = \Theta \sum_{k=1}^{N-1} \mathcal{H}(z - kL), \quad (10)$$

Θ the cell-wise reorientation angle such that $N\Theta$ is commensurate with 2π and \mathcal{H} the Heaviside function [83].

3.2.2 Industrial and technological relevance

Periodic duct flows constitute the generic configuration for industrial devices involving *continuous* processing or treatment of laminar fluid streams.⁸ Applications are numerous and include [1, 2, 3, 6, 7, 10, 9, 4, 12, 5, 8, 11, 13, 16, 14, 15, 17, 18, 19]:

- inline mixers for food processing;
- extruders for polymer processing;
- compact inline mixers for process intensification;
- inline micro-mixers and throughflow compartments in micro-fluidic (lab-on-a-chip) devices.

The purpose is mixing of a continuous axial throughflow at velocity u_z (typically pressure-driven) by systematic reorientation of the transverse flow (u_x, u_y) via e.g. static internal mixing elements [1, 3, 4]. Fig. 6 demonstrates this principle for the RAM introduced above [66]. Here the transverse flow is driven by viscous drag exerted by a rotating outer cylinder via apertures in the stationary inner cylinder (Fig. 6(a)); the cell-wise reorientation angle Θ following (10) is the angular offset of consecutive apertures accomplishes systematic

⁸Flow in such devices normally settles on a repeated pattern and thus effectively becomes periodic after a short transient following the inlet [84].

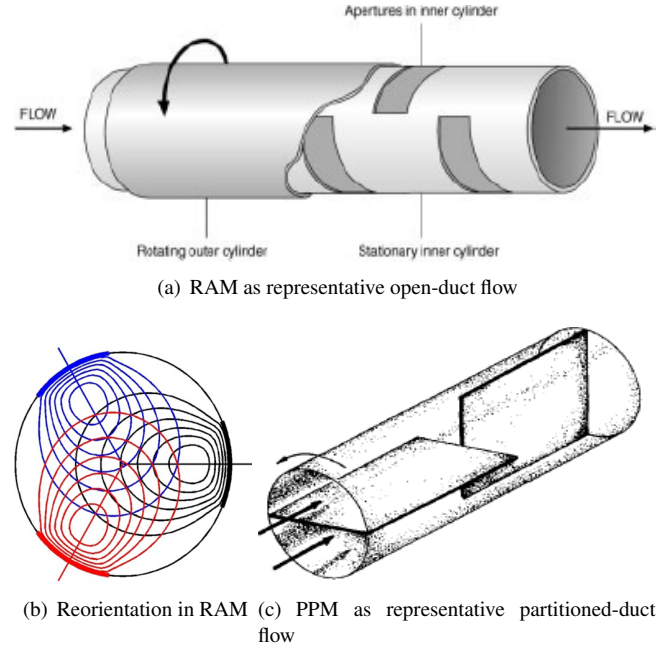


Fig. 6. Rotated Arc Mixer (RAM) and Partitioned-Pipe Mixer (PPM) as representative *open-duct* and *partitioned-duct* inline mixing flows, respectively: (a) reorientation in RAM by angular offset of apertures in inner cylinder (reproduced from [66]); (b) reoriented transverse streamline portraits in RAM (colour distinguishes aperture); (c) reorientation in PPM by splitting and recombination of axial flow via alternating horizontal/vertical internal plates (reproduced from [85]).

downstream reorientation of the transverse flow following Fig. 6(b). Each tube section containing an aperture defining one cell and shown black/blue/red transverse streamline patterns correspond with flow (9) in cells $k = 1, 2, 3$, respectively, for $\Theta = 2\pi/3$ of duct segments of $N = 3$ cells.

The RAM is inspired by the Partitioned-Pipe Mixer (PPM) shown in Fig. 6(c) [85]. The PPM achieves reorientation by the combined effect of a rotating cylinder and alternating horizontal/vertical static internal elements that repeatedly split and recombine the axial throughflow. The PPM served as model problem for the pioneering work on industrial mixers by the Ottino group (Sec. 3.1). The RAM and PPM capture the essentials of two kinds of periodic duct flows relevant in the present context:

- *Open duct flows*: consist of a duct devoid of internal walls and rely on reorientation by the transverse boundary forcing as primary mixing mechanism.
- *Partitioned duct flows*: consist of a duct partitioned by internal walls and rely on reorientation by splitting and recombination of the axial flow as primary mechanism.

Moreover, the RAM and PPM have both been the subject of in-depth (experimental) Lagrangian transport analyses and thus are well-suited to bridge the theory–practice gap. Hence, the RAM and PPM are adopted hereafter as the two representative periodic duct flows.

Generic flow topology The generic 3D flow topology of periodic duct flows is demonstrated in Fig. 7(a) for the RAM.

It typically consists of families of concentric stream tubes running from inlet to outlet of the duct segment (3 specimens highlighted in colour) embedded in chaotic streamlines (black). Fig. 7(b) gives the corresponding axial cross-section at the inlet and reveals a transverse topology reminiscent of the stroboscopic map of the lid-driven cavity in Fig. 5(a): islands in a chaotic sea. This reflects the fundamental property that 3D steady duct flows (in principle) are dynamically equivalent to 2D time-periodic flows and kinematic equation (2) admits a (formal) transformation \mathcal{F} following

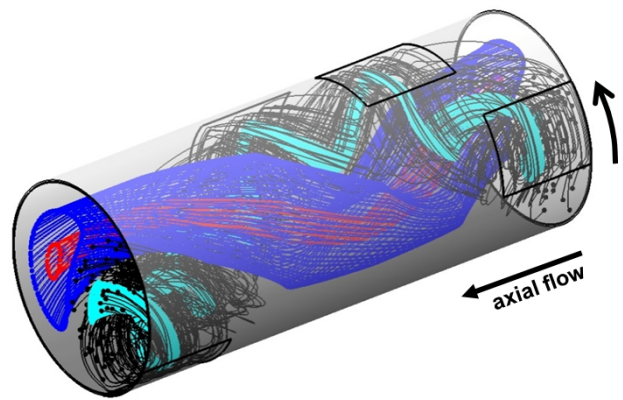
$$\frac{d}{dt} \begin{bmatrix} x \\ y \\ z \end{bmatrix} = \begin{bmatrix} u_x \\ u_y \\ u_z \end{bmatrix} \xrightarrow{\mathcal{F}} \frac{d}{d\tau} \begin{bmatrix} \zeta_1 \\ \zeta_2 \end{bmatrix} = \begin{bmatrix} v_1 \\ v_2 \end{bmatrix}, \quad (11)$$

such that the transverse and axial Lagrangian motion corresponds with transport in the 2D domain (ζ_1, ζ_2) and periodic evolution in “time” τ , respectively. The LCSs relate as follows: periodic points, islands and 1D manifolds (i.e. curves) in 2D materialise as axially reconnecting streamlines, tubes and 2D manifolds (i.e. surfaces), respectively, in 3D (Sec. 4.1.4).

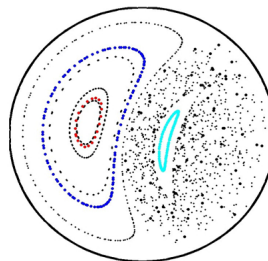
The Lagrangian framework developed by the Ottino group (Sec. 3.1) implicitly relies on transformation (11) following Sec. 4.3.2 and studies on the RAM explicitly demonstrate its existence (at least) for generic open-duct flows [83, 86]. Localised phenomena such as reversed axial flow or internal recirculations may restrict this transformation – and the equivalence with 2D dynamics – to a “net through-flow region” yet this is inconsequential for the functionality of open-duct mixers [86].

The equivalence (of at least said net throughflow region) with 2D unsteady flows means that 3D steady duct flows can basically always be designed to achieve global chaotic advection. Parametric studies enable systematic isolation of the appropriate operating conditions and thus are a common approach for optimisation and design of actual devices [62, 63, 50, 64, 6, 65, 7, 66, 67, 9, 13, 68, 16, 69, 71, 72, 73]. Fig. 7(c) gives the stroboscopic map for the RAM optimised by this approach, yielding a chaotic state devoid of stream tubes and, inherently, efficient mixing.

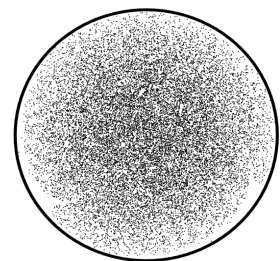
The generic composition of 3D Lagrangian flow topologies according to Fig. 7(a) and the impact upon the transport is demonstrated experimentally via dye visualisation for the RAM in Fig. 8(a) and the PPM in Fig. 8(b) [85, 66]. Two situations are considered for each system, viz. a poor-mixing case (top) with cross-sectional stroboscopic map containing islands similar to Fig. 7(b) and a good-mixing case (bottom) exhibiting global chaos as in Fig. 7(c). (Stroboscopic maps of the PPM are essentially similar as in Fig. 7 [85, 87].) The dye visualisations in both RAM and PPM indirectly expose the coexisting tubes and chaotic regions of the poor-mixing case via the entrapment of the red dye and transverse spreading of the green dye, respectively. The global chaotic advection of the good-mixing case is clearly demonstrated by the transverse spreading of both the red and green dye and the resulting formation of a homogeneous (yellowish) mixture.



(a) 3D flow topology

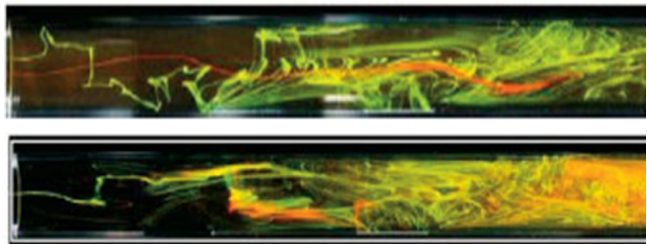


(b) Cross-section at inlet

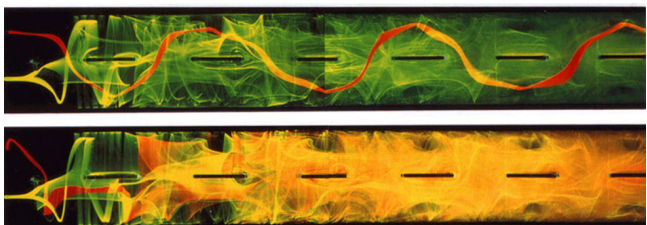


(c) Globally-chaotic topology

Fig. 7. Generic composition of 3D flow topology of periodic duct flows demonstrated for RAM: (a) stream tubes (colour) embedded in chaotic environment (black) for sub-optimal RAM; (b) corresponding cross-section at inlet; (c) globally-chaotic topology for optimised RAM. Created using analytical 2.5D RAM flow from [83].



(a) RAM: poor (top) versus good (bottom) mixing.



(b) PPM: poor (top) versus good (bottom) mixing.

Fig. 8. Mixing performance versus flow topology demonstrated experimentally by dye visualisation: (a) RAM (adapted from [66]); (b) PPM (adapted from [85]). Poor (good) mixing concerns topologies with(out) streamtubes; side view with axial flow from left to right.

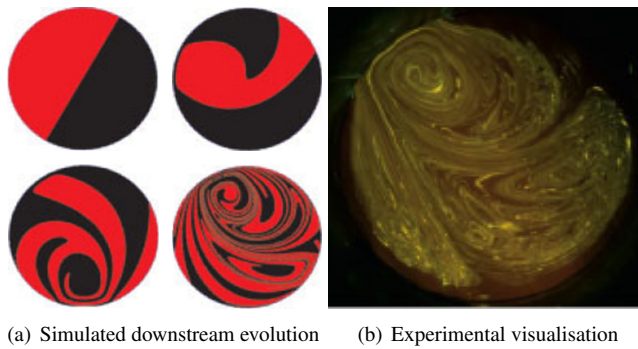


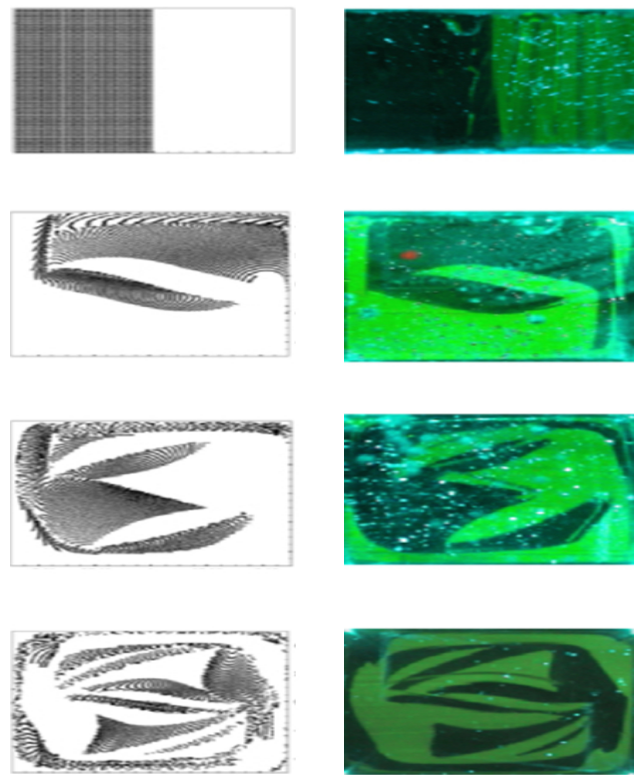
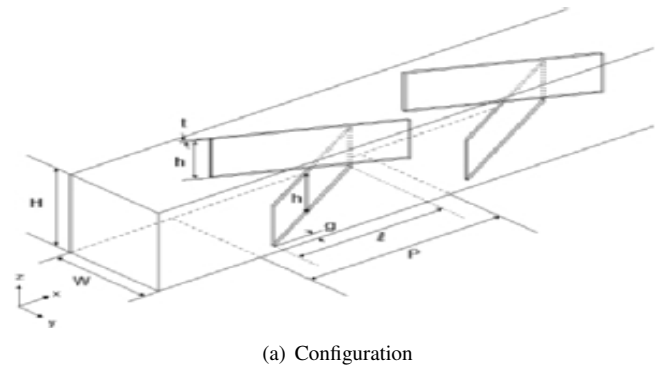
Fig. 9. Typical cross-sectional mixing patterns in RAM: (a) simulated downstream evolution of binary (red/black) concentration distribution (reproduced from [88]); (b) corresponding experimental visualisation by fluorescent dye (reproduced from [66]).

Chaotic advection implies cross-sectional mixing patterns with downstream progression similar to Fig. 4. This is demonstrated in Fig. 9(a) by the simulated evolution of a binary concentration distribution in the RAM, revealing the characteristic stretching and folding imparted by the unstable manifold (not shown) following Fig. 5 [88]. Experimental visualisation using fluorescent dye illuminated by a transverse light sheet near the outlet of the RAM set-up of Fig. 8(a) exposes (for comparable operating conditions) an essentially similar cross-sectional mixing pattern (Fig. 9(b)) [66]. This experimentally validates the key mechanism underlying chaotic advection in inline mixers and indirectly visualises the governing LCS(s), viz. the unstable manifold(s).

Open-duct flows: micro-mixers using patterned walls
 Inline mixers of the open-duct type are, apart from the RAM, found mainly in micro-fluidics and usually accomplish transverse flow and reorientation by patterned duct walls.⁹ Consider as an example the square micro-channel with cross-baffles extending from top and bottom channel walls shown in Fig. 10(a) [89]. The cross-baffles merely “deform” the duct boundary without partitioning the domain and thus the system indeed constitutes an open-duct flow. This holds, irrespective of the geometric complexity, for any wall pattern and duct shape.

Fig. 10(b) gives a typical cross-sectional mixing pattern in the above micro-mixer according to the simulated evolution of a patch of black tracer particles (left) versus experimental visualisation by fluorescent dye via transverse light sheets (right). This reveals the same progressive stretching and folding as in the RAM (Fig. 9) and thus demonstrates (i) the universality of Lagrangian (chaotic) transport phenomena of open-duct flows and (ii) the intrinsic similarity in mixing characteristics of (practical) flows belonging to this class. Moreover, the close agreement between computational and experimental results further substantiates the physical validity and meaningfulness of the Lagrangian concept.

⁹Reorientation by static wall structures instead of wall motion (as e.g. in the RAM) is inconsequential for classification as an open-duct flow.



(b) Simulated (left) vs. experimental (right) cross-sectional mixing pattern.

Fig. 10. Open-duct micro-mixer using patterned wall for reorientation: (a) rectangular channel with wall-mounted cross-baffles; (b) cross-sectional mixing pattern according to simulated downstream cross-sections of streamlines of black tracers (left) versus experimental visualisation by fluorescent dye (right). Adapted from [89].

Other inline micro-mixers adopting patterned walls for reorientation – thus defining open-duct flows with basically the same transport characteristics as above – include the “staggered-herringbone mixer” (using grooved walls) and the “C-shaped serpentine micromixer” (using C-shaped duct segments) and numerous variations on these designs [90, 13]. State-of-the-art micro-manufacturing technologies make commercial fabrication of such devices increasingly feasible and may thus become a key enabler for the practical application of chaos-based micro-mixing technology [91].

Partitioned-duct flows: static mixers using baffles Inline mixers of the partitioned-duct type have a long history as

static mixers in the traditional processing industry. These devices rely on partitioning of the flow domain by internal static mixing elements (“baffles”) for reorientation and the Kenics mixer is perhaps the best known incarnation of this principle. Its original design dates back to the 1960s [92] and to this day finds widespread utilisation in fluids engineering (Sec. 5.2.1) [1, 2]. Modified Kenics designs have even been implemented in micro-mixers [93]. Hence, the Kenics mixer, arguably, is the archetypical static mixer and on that grounds served as model for the PPM [52].

The Quatro mixer (Primix BV, Mijdrecht, The Netherlands) is a static mixer reminiscent of the Kenics mixer [94]. Its mixing elements consist of chevron-shaped central plates with perpendicular elliptical segments extending to the cylinder wall and are alternately reversed and rotated about the cylinder axis (grey elements 1 and 2 in Fig. 11). This yields a periodic repetition of pairs of mixing elements analogous to the consecutive pairs of reordered plates in the PPM.

Fig. 11 demonstrates the transverse mixing within each duct segment by horizontal and vertical splitting (and subsequent recombination) of the axial throughflow by the central plates of elements 1 and 2, respectively, via the 3D streamline pattern measured with 3D Particle Tracking Velocimetry (3DPTV) [94, 84]. Mixing element 1 splits the incoming fluid into two separate streams (indicated in red and green) that, in turn, undergo further splitting by element 2, resulting in a “mixture” of red and green streamlines at the segment exit. Repetition of this process by consecutive duct segments yields ever finer striations as visualised in Fig. 12(a) by transverse cuts of the 3D distribution of a fluorescent dye (bright) injected at the inlet and measured by 3D Laser-Induced Fluorescence (3DLIF) [84]. Here mixing elements 1,3,5 are the upstream elements (i.e. element 1 in Fig. 11) in the consecutive duct segments 1,2,3, respectively, and shown cuts are halfway the central horizontal plate (white bar).

The cross-sectional mixing pattern in Fig. 12(a) exhibits stretching and folding (signifying chaotic advection) akin to the RAM (Fig. 9) and the micro-mixer (Fig. 10) and thus the Quatro mixer, notwithstanding the entirely different designs of the devices, accomplishes efficient mixing by essentially the same Lagrangian mechanism. However, the underlying 3D fluid motion is markedly different. Said open-duct mixers effectively coil up streamlines reminiscent of twirling spaghetti around a fork, illustrated in particular by the black chaotic streamlines in Fig. 7(a), giving rise to cross-sectional swirling (Fig. 9). The (partitioned-duct) Quatro mixer, on the other hand, progressively “slices” the downstream fluid stream not unlike a meat grinder, as visualised in Fig. 12(b) by longitudinal cuts of the 3D dye distribution in the indicated mixing elements (top view of central horizontal plate). This manifests itself in the cross-sectional filamentation shown in Fig. 12(a).

Inline static mixers, regardless of baffle shape and fluid rheology, exhibit basically the same Lagrangian transport characteristics as the Quatro mixer. Consider to this end e.g. the qualitative resemblance of the cross-sectional mixing patterns in Fig. 12(a) with the dye visualisations of those for shear-thinning fluids in Kenics static mixers [80]. The

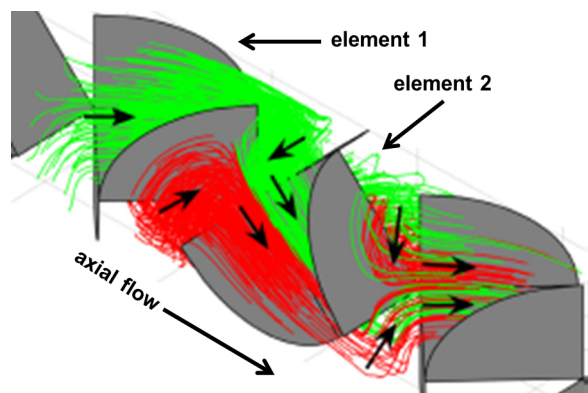
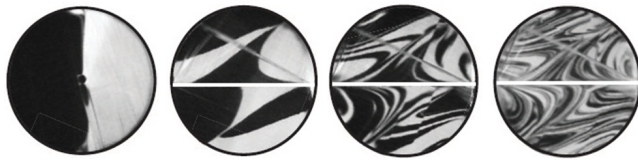


Fig. 11. Partitioned-duct mixer using internal mixing elements for reorientation demonstrated for Quatro mixer by 3D internal streamlines measured by 3DPTV. Red/green streamlines represent axial flow separated by element 1; arrows within streamlines indicate local flow direction. Adapted from [84].

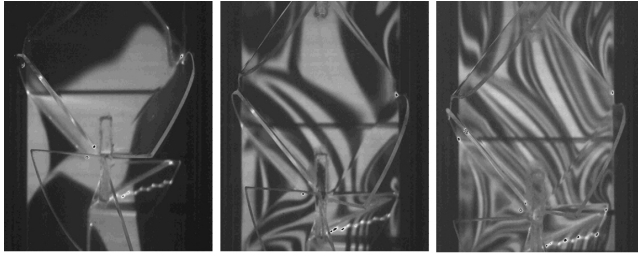
wide variety of baffles employed in industry is nonetheless designed primarily by empirical studies and case-specific numerical simulations using standard mixing measures such as the CoV (Sec. 3.1). Design and optimisation of static mixers using Lagrangian concepts, on the other hand, is rare and mainly restricted to studies in engineering sciences on the beforementioned Kenics and Sulzer mixers [62, 63, 95, 70]. This strongly suggests that many mixer designs are in fact sub-optimal and industry may greatly benefit from dedicated engineering tools as e.g. post-processing modules in a (commercial) CFD package for determination of cross-sectional stroboscopic maps. The latter namely enables systematic and conclusive isolation of the operating conditions that yield global chaotic advection as in Fig. 7(c).

An open fundamental issue concerns the impact of the internal walls on the Lagrangian framework. The existing approach implicitly relies on transformation (11) and studies to date basically confirm its validity. However, internal walls may, besides the beforementioned reversed axial flow and recirculation, introduce singularities that (locally) break the link with 2D unsteady systems and thus pave the way to essentially 3D phenomena (Sec. 4.3.2). In particular LCSs emerging from critical points on the internal boundaries (instead of periodic points (6) and corresponding reconnecting streamlines in the flow interior) are likely to play a (decisive) role in the transport characteristics on grounds of the analogy with transport in porous media. The latter namely involves similar splitting and recombination of throughflows by internal walls and is in fact dominated by such LCSs (Sec. 3.5.1). Hence investigation of transformation (11) for partitioned flow domains and wall-induced LCSs according to Sec. 3.5.1 may strengthen the theoretical foundation and yield important insights with possible new applications.

Partitioned-duct flows: branching micro-channels The partitioned-duct principle finds application also in microfluidic inline mixers yet, owing to the difficult fabrication of microscopic baffles, typically in the form of branching and



(a) Transverse cross-sections from inlet (left) via mixing elements 1,3,5.



mixing element 1 mixing element 3 mixing element 5

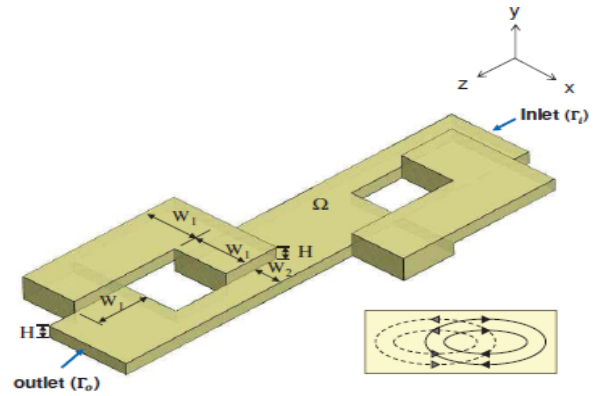
(b) Longitudinal cross-sections in mixing elements 1,3,5.

Fig. 12. Evolution of 3D mixing pattern in Quatro mixer visualised by 3DLIF: (a) transverse cross-sections at indicated elements (adapted from [84]); (b) corresponding longitudinal cross-sections.

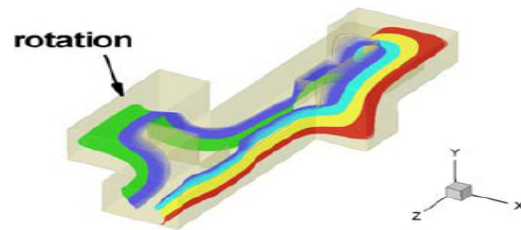
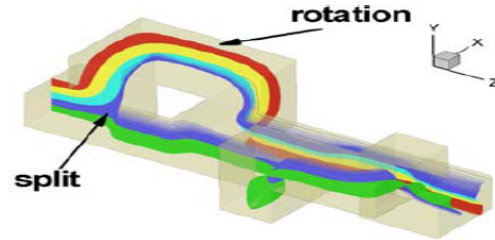
reconnecting channels. Consider for illustration the chaotic serpentine micro-mixer (CSM) [96, 97]. Fig. 13(a) shows one duct segment comprising of two branching-reconnecting cells that each are composed of a pair of reversed L-shaped channels. Thus each cell in the CSM, despite distributing the fluid streams over two physically separate channels, gives rise to basically the same splitting and recombination of the axial throughflow as imparted by each mixing element in the Quatro mixer. Fig. 13(b) demonstrates this by the simulated foliation of the internal 3D material interface separating the incoming fluid streams, revealing a “slicing” as in Fig. 11 and Fig. 12(b). The corresponding cross-sectional mixing pattern is shown in Fig. 13(c) and exhibits similar filamentation as in Fig. 12(a). Hence, transport in the CSM, despite completely different designs and length scales, indeed emanates from essentially the same Lagrangian mechanisms as the Quatro mixer and, inherently, any partitioned-duct mixer.

Aperiodic duct flows A class of inline mixers intimately related to the above devices exists in *aperiodic* duct flows, that is, axial throughflows without the periodic structure following (8) and (9). Consider for illustration the T-shaped micro-mixer in Fig. 14(a): two fluid streams are brought together via separate inlets and undergo transverse mixing by a vortical flow in one common outlet duct (reminiscent of open-duct flows) induced at the junction in case of sufficiently strong fluid inertia (Fig. 14(b)) [98, 9].

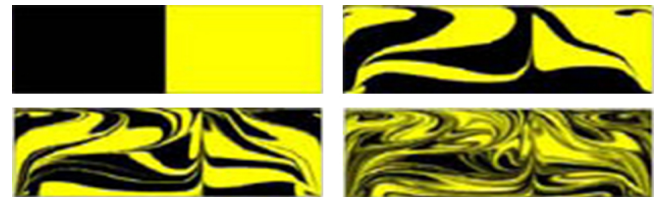
Said vortical flow (termed “engulfment flow” in [98, 9] and occurring if the Reynolds number Re exceeds a certain threshold) is characterised by two adjacent counter-rotating longitudinal swirling flows that intensify in downstream direction and each cross the vertical axial midplane of the duct (Fig. 14(b)). This yields a 3D mixing pattern consisting of two longitudinal “mixing rolls” visualised in Fig. 15(a) by iso-contours of a 3D dye distribution – and cor-



(a) Single duct segment



(b) 3D interface between species



(c) Typical cross-sectional mixing pattern (inlet to outlet)

Fig. 13. Partitioned-duct micro-mixer using branching channels for reorientation demonstrated by chaotic serpentine micro-mixer: (a) single duct segment (reproduced from [97]); (b) simulated splitting and recombination of 3D material interface (colour distinguishes vertical position at inlet); (c) simulated evolution of segment-wise cross-sectional mixing pattern. Panels (b,c) adapted from [96].

responding cross-sectional evolution (Fig. 15(b)) – using μ -LIF [98]. Numerical simulations for similar flow conditions (Fig. 15(c)) reveals a roll-wise “stretching and folding” pattern reminiscent of the RAM (Fig. 9). This implies similar transport characteristics as the periodic counterparts and thus strongly suggests that the nature of the axial evolution, i.e. periodic versus aperiodic, is of secondary importance to this process.

The (spatial) aperiodicity has in fact primarily theoretical/conceptual ramifications by considerably limiting the

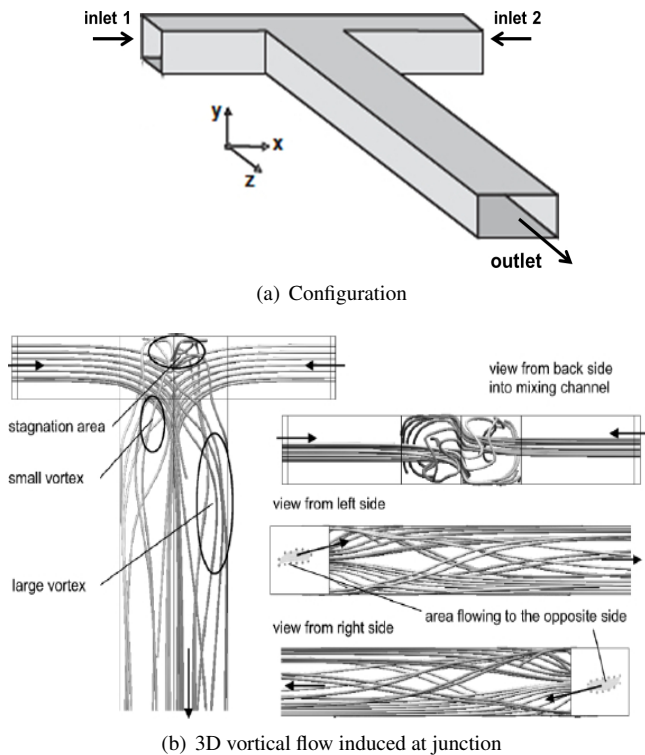
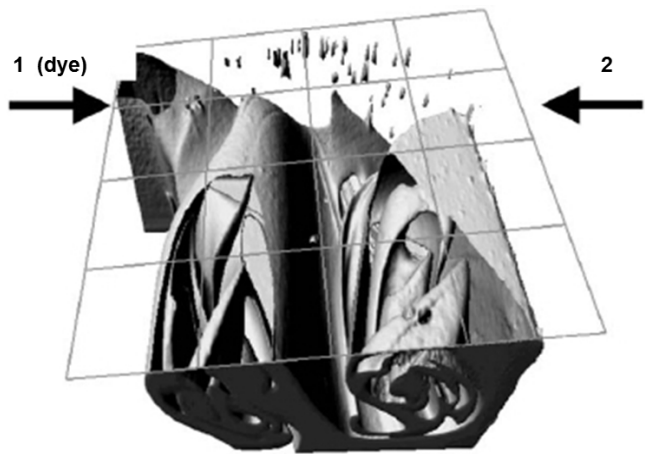


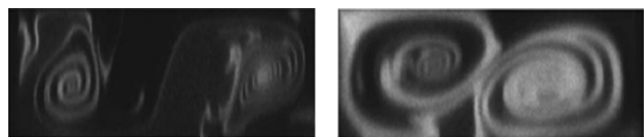
Fig. 14. T-shaped micro-mixer as representative aperiodic duct flow: (a) configuration of double inlet and single outlet (reproduced from [98]); (b) transverse mixing by 3D vortical flow (illustrated by typical 3D streamline pattern) induced at junction (reproduced from [9]).

usefulness of the existing Lagrangian machinery for transport analysis due to its strong reliance on stroboscopic maps and LCSs associated with periodic points (6) (Sec. 2). This limitation is of even greater significance for geophysical flows and in particular the latter spurred scientific efforts, with George Haller and co-workers at the vanguard, to generalise the notion of coherence imparted by “special” Lagrangian entities (i.e. LCSs) to aperiodic flows [59].¹⁰ Relevant here are particularly so-called *attracting LCSs*, i.e. the aperiodic counterparts to the *unstable* manifolds in Fig. 5(a), which in a similar manner as the latter govern stretching and folding – and thus chaotic advection – in aperiodic flows [59] (Sec. 4.1). Isolation of attracting LCSs in the T-shaped micro-mixer is (to the best of our knowledge) outstanding yet their identification in an analogous flow in life sciences, i.e. an artery bifurcation (Fig. 16 in Sec. 3.2.3), provides compelling evidence of their existence. This, in turn, underpins the above conjecture that the transport characteristics of (a)periodic duct flows are in essence the same. However, generalisation of the Lagrangian framework to a universal and unambiguous approach for *aperiodic* and, intimately related, *finite-time* (transient) flows is still in progress (Sec. 6).

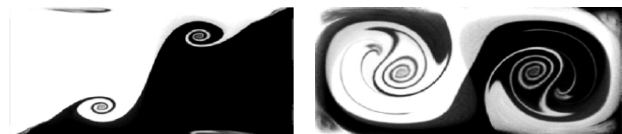
¹⁰Term “Lagrangian coherent structures” (LCSs) in fact stems from these efforts and here denotes such entities in both periodic and aperiodic flows.



(a) Experimental 3D mixing pattern near junction



(b) Dye pattern directly (left) & further (right) downstream of junction



(c) Simulated pattern directly (left) & further (right) downstream of junction

Fig. 15. Typical 3D mixing pattern in T-shaped micro-mixer: (a) experimental visualisation by fluorescent dye near junction using μ -LIF; (b) corresponding cross-sectional patterns downstream of junction (adapted from [98]); (c) simulated cross-sectional mixing patterns downstream of junction (adapted from [9]).

3.2.3 Relevance beyond industry

Lagrangian transport and 3D chaotic advection in (a)periodic duct flows is also at the heart of several non-industrial configurations and thus implies fundamental similarities with the above industrial systems. This is illustrated below by way of examples.

Cardio-vascular flows An important physiological occurrence of *aperiodic* duct flows is found in human carotid artery bifurcations (Fig. 16(a)). Carotid arteries supply oxygenated blood to the head and neck and their bifurcations are known as a site of chronic atherosclerotic plaque formation by the deposition of fat dissolved in the blood stream on the artery walls. The corresponding Lagrangian transport closely resembles that in the T-shaped micro-mixer yet reversed in time in that the blood flow *approaches* a bifurcation via a single duct and *exits* via two ducts (implying 3D vortical flow akin to Fig. 14 yet in opposite direction). Experimental 3D steady velocity fields constructed in [99] from 2D cross-sectional measurements with stereo Particle Image Velocimetry (PIV) in a laboratory model indeed reveal vortical motion at the bifurcation similar to the T-shaped micro-mixer (Fig. 14(b)). The *attracting* LCSs, computed

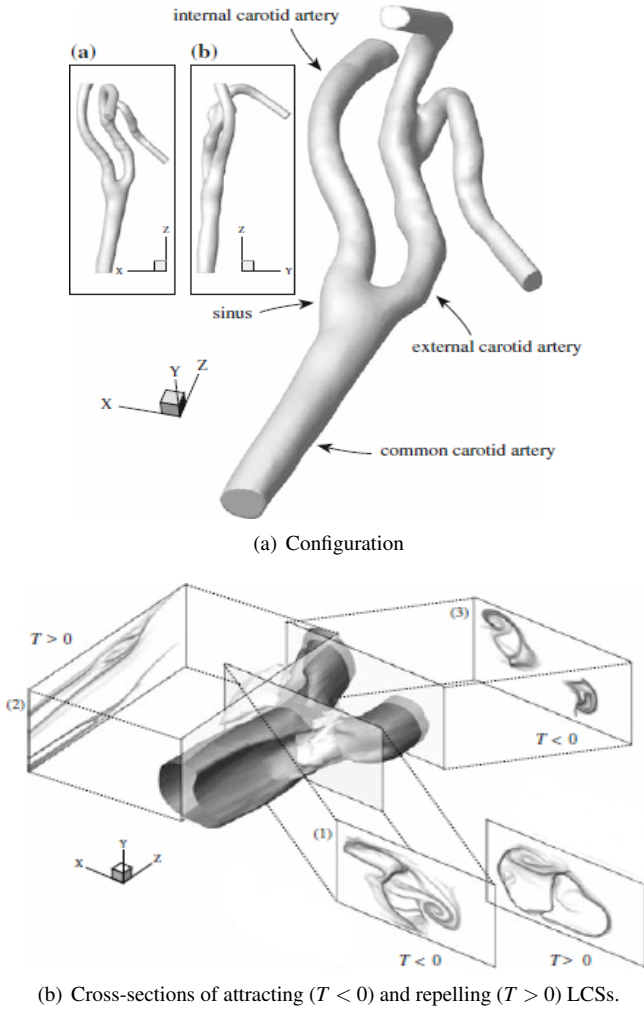


Fig. 16. Human carotid artery bifurcations as physiological analogy to aperiodic T-shaped micro-mixers: (a) configuration; (b) flow topology consisting of attracting and repelling LCSs. Adapted from [99].

using the experimental flow, are given in Fig. 16(b) in the transverse cross-sections 1 and 3 (indicated by $T < 0$) and exhibit similar stretching and folding as their periodic counterparts, i.e. the *unstable* manifolds, in Fig. 5(a). Shown also are the corresponding *repelling* LCSs (indicated by $T < 0$) in cross-section 1 and stream-wise cross-section 2, which are the aperiodic counterparts to the *stable* manifolds in Fig. 5(a.) Existence of these entities – and their similarity to manifolds in chaotic seas – strongly suggests chaotic advection in the artery bifurcation and, by analogy, also in the T-shaped micro-mixer. Moreover, the implication of chaotic advection with atherosclerosis in carotid arteries is consistent with its purported role in blood-clot and plaque formation in aneurysms (Sec. 3.1 and Sec. 3.3.3). Hence, chaotic advection could be, by tending to augment the residence time of blood-borne substances [29], a central player in the development of vascular diseases. Further exploitation of the resemblance with industrial inline mixers and application of the corresponding (scientific) knowledge on (chaotic) Lagrangian transport may contribute to the understanding of these processes.

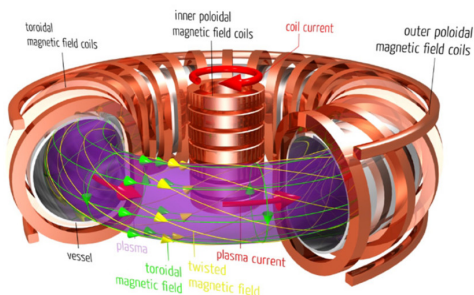
Tokamak fusion reactors A remarkable analogy exists between *periodic* duct flows \vec{u} and the magnetic fields \vec{B} of magneto-hydrodynamic (MHD) descriptions of plasmas in tokamak fusion reactors (Fig. 17(a)). First, a periodic duct is topologically a torus and thus equivalent to the interior of said reactors. Second, flow and magnetic fields are both solenoidal, i.e. $\vec{\nabla} \cdot \vec{u} = 0$ and $\vec{\nabla} \cdot \vec{B} = 0$. Third, the toroidal-poloidal magnetic forcing imposes similar net flux and reorientation as the axial-transverse forcing in periodic ducts. Thus the tokamak admits a transformation \mathcal{F} following (11) of magnetic field \vec{B} and toroidal reference frame (σ, η, φ) such that poloidal (σ, η) and toroidal (φ) dynamics correspond with canonical space (ζ_1, ζ_2) and time τ , respectively.¹¹ These commonalities render periodic duct flows and magnetic fields in MHD tokamak models topologically and kinematically equivalent [54, 101, 100].

The objective in tokamak fusion plasmas is accomplishment of so-called “magnetic confinement”, that is, a magnetic topology consisting entirely of one global family of concentric tubes (denoted “magnetic flux surfaces” and indicated schematically by the purple torus in Fig. 17(a)) similar to the stream tubes in the RAM (Fig. 7(a)). However, this remains a major challenge and is in fact the principal hindrance to the envisaged application of fusion plasmas as heat source for power plants (and safe alternative to nuclear *fission*) [100].

Magnetic confinement may be broken by the disintegration of certain flux surfaces through the nonlinear process of reconnection, yielding metastable states denoted “neo-classical tearing modes” (NTMs) that precede global instability of the magnetic field [101, 100]. Such NTMs are often investigated in an oversimplified manner, though. First, their (poloidal) magnetic topology is typically assumed to entirely consist of one central island with multiple satellite islands arranged by “o-points” and “x-points” following Fig. 17(b) [100]. (Former and latter are the magnetic equivalents to elliptic and hyperbolic points, respectively, in flow topologies.) The analogy with periodic duct flows strongly suggests far more complex NTM topologies similar to Fig. 7. Both numerical studies and experimental evidence support this [102, 103, 104, 105]. Fig. 17(c) gives a typical simulated poloidal NTM topology that indeed exhibits the expected characteristics; the red curve is a shearless transport barrier and is (considered) key to the survival of the remaining flux surfaces [105]. Second, transport by chaotic magnetic field lines is commonly regarded a stochastic turbulent-diffusion-like mechanism (“magnetic turbulence”) devoid of spatial organisation [100, 106]. However, chaotic advection in mixing flows implies a (though highly complex) well-defined spatial structure imparted by manifolds (Fig. 5) and thus fundamentally contradicts this key assumption. Dedicated studies on chaotic magnetic field lines are indicative of such a spatial structure in NTM topologies [107, 106].

The above strongly suggests that incorporation of the true (3D) topological structure of the magnetic field and in-

¹¹This holds equally for the so-called “flux coordinates” often employed in tokamaks; these are namely intimately related to the toroidal frame [100].



(a) Tokamak reactor with magnetic field lines and flux surfaces.

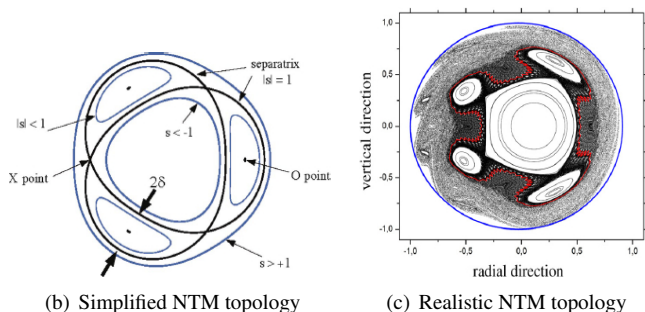


Fig. 17. Tokamak fusion reactors as MHD analogy to periodic open-duct flows: (a) configuration including magnetic field lines (green/yellow) and flux surfaces (purple) (reproduced from Max-Planck Institut für Plasmaphysik); (b) simplified cross-sectional NTM topology of magnetic islands only (reproduced from [100]); (c) realistic topology with islands and chaotic regions (reproduced from [105]).

sights into (chaotic) Lagrangian transport is imperative for in-depth MHD-based analyses of tokamak fusion plasmas and magnetic confinement. The established link with periodic duct flows offers a way to achieve this.

3.3 Flow in containers

3.3.1 General configuration

Containers are defined as 3D flow domains confined by a closed surface (i.e. flux across the boundaries is absent) that are topologically equivalent to spheres. This includes, besides the latter, common geometries as cylinders and cubes. The key difference with periodic ducts exists in the nature of the domain. Periodic ducts and containers namely are topologically a *torus* and a *sphere*, respectively, which can have fundamental consequences for the Lagrangian flow topology and associated transport properties

Flow and transport in periodic ducts and containers constitute the two principal canonical problems in the present categorisation. The surface classification theorem namely states that orientable¹² closed surfaces are topologically equivalent to the surface of either a connected sum of tori or a single sphere [108]. Hence, tori and spheres are the fundamental building blocks of 3D (realistic) flow domains and Lagrangian transport in any such configuration thus intimately relates to that in periodic ducts and/or containers.

¹²I.e. with a uniquely defined normal. Examples of non-orientable surfaces are the Möbius strip and the Klein Bottle.

3.3.2 Industrial and technological relevance

Flows in containers are the generic configuration for industrial devices involving *batch* processing or treatment of fluid bodies under laminar conditions. Practical applications include [1, 2, 109, 5, 11, 110, 111, 112]:

- bio-reactors;
- food processing;
- electro-magnetic materials processing;
- batch micro-mixers and processing chambers in micro-fluidic (lab-on-a-chip) devices.

The confinement by the closed boundary imparts a flow (topology) that generically involves a global circulation and consists of (multiple) vortical structures. Consider as a first illustration the impeller-driven flow in Fig. 1(a); here the toroidal tracer paths reveal a primary circulation about the impeller and a secondary circulation transverse to this. However, unlike periodic duct flows, the flow (topology) in containers may vary significantly with driving mechanism (i.e. surface versus body forcing) and time signature (i.e. steady versus unsteady). Hence, this flow class is discussed below in terms of the following basic practical configurations:

- steady flow driven by *body* forcing;
- steady flow driven by *surface* forcing;
- unsteady flow.

This classification is somewhat pragmatic by leaning on relevant *practical* characteristics of container flows and is adopted here for reasons of accessibility. A more rigorous (yet at this point inscrutable) differentiation can be made on the basis of *dynamic* characteristics and emerges naturally in the course of the following discussion.

Steady flow driven by body forcing The abovementioned impeller-driven flow is archetypal of a steady container flow driven by body forcing; the immersed stirring device namely effectively acts as a (local) body force. This is the most common configuration in industrial batch mixers and thus of great practical relevance.

The study by [113, 114] adopts the flow inside a cylindrical container driven by a tilted rotating disk following Fig. 18(a) as physical model for industrial batch mixers. (The specific domain and stirrer geometry are of secondary importance.) Fig. 18(b) visualises the Lagrangian transport using fluorescent dye and reveals, consistent with the toroidal paths in Fig. 1(a), a 3D flow topology comprising of nested closed stream tubes (one specimen highlighted by red dye) encircling the rotation axis of the impeller. The corresponding vertical cross-section, visualised in Fig. 18(c) by red and green dye, and intersections of 3D computational streamlines (Fig. 18(d)) imply an internal structure resembling the transverse topology of duct flows (Fig. 7(b)): islands in a chaotic sea. This has the fundamental implication that, despite topologically different flow domains, the 3D Lagrangian motion and flow topology of the impeller-driven flow are dynamically similar to periodic duct flows. The similarity is particularly apparent upon comparison with the tokamak fusion reactor in Fig. 17. The cross-sectional and azimuthal

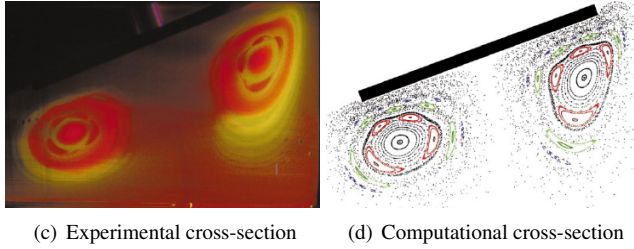
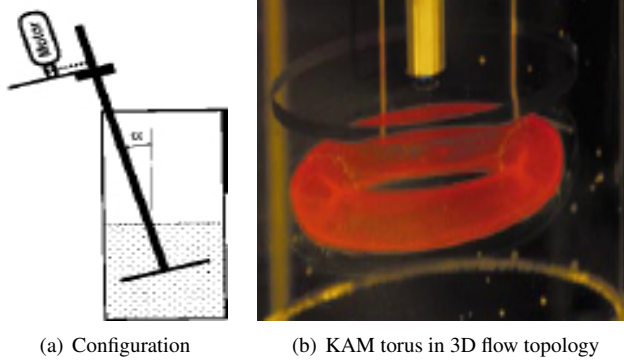


Fig. 18. Impeller-driven steady flow in a cylindrical container as physical model for industrial batch mixers: (a) configuration with tilted disk as impeller; (b) typical KAM torus in 3D flow topology visualised by red fluorescent dye; (c) vertical cross-section of 3D flow topology visualised by red/green dye; (d) corresponding simulated topology visualised by cross-sections of 3D streamlines. Adapted from [114].

dynamics in the impeller-driven flow are equivalent to the poloidal/toroidal dynamics of the tokamak and, in turn, to the transverse/axial dynamics of periodic duct flows. This implies for the impeller-driven flow a transformation (11) of the cylindrical reference frame (r, θ, z) such that canonical space (ζ_1, ζ_2) and time τ correspond with r_z -plane and azimuthal component θ , respectively. (Refer to Sec. 4.3.3 and Sec. 4.6.2 for the conditions permitting this transformation.) The (closed) stream tubes as shown in Fig. 7(a) and Fig. 18(b) and the magnetic flux surfaces in Fig. 17(a) thus constitute equivalent LCSs and are denoted “Kolmogorov-Arnold-Moser (KAM) tori” in dynamical-systems terminology [52, 100]. This nomenclature is adopted hereafter to indicate such entities.

Lagrangian flow topologies consisting of KAM tori embedded in chaos is generic for steady flows driven by body forcing. The particular forcing and/or domain geometry may (significantly) affect the emergence and arrangement of KAM tori and other LCSs, though. Consider to this end the impact of the impeller shape and positioning on the flow topology of the stirred container in Fig. 18(a). A single impeller consisting of blades and rotating about the cylinder axis (i.e. a so-called “Rushton impeller” widely used in industry) results in two “stacked” families of KAM tori as visualised in Fig. 19(a) (left) by the transverse cross-section of a 3D distribution of tracer particles [115]. Detailed dye visualisation under comparable operating conditions reveals the upper tori family and its chaotic environment (Fig. 19(a); right) [44]. The latter corresponds with the “ripples” ex-

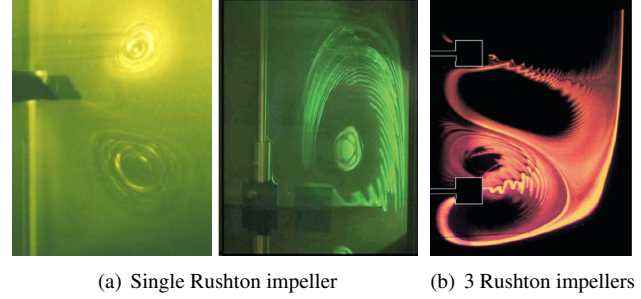


Fig. 19. Impact of impeller geometry on transport properties of impeller-driven flow in cylindrical container: (a) cross-sectional mixing pattern (left) and close-up (right) for single-impeller case visualised experimentally by fluorescent dye (adapted from [115]); (b) dye visualisation for 3-impeller case (reproduced from [116]).

tending from the impeller, which exhibit the characteristic stretching-and-folding pattern created by manifolds akin to Fig. 5. A configuration of 3 Rushton impellers yields a sizeable chaotic region, visualised by the dye concentration at the upper/middle impellers in Fig. 19(b), enveloping multiple tori families of variable extent (black islands) [116]. The impellers induce similar “rippling” (signifying chaotic advection) as the single-impeller case.

The above experimental analyses reveals a dramatic impact of the impeller geometry on the mixing properties. Stirring by disks rotating about the cylinder axis yields only KAM tori; tilting of the rotation axis is essential to induce chaos yet this remains highly localised (Fig. 18) [114]. The Rushton impellers, on the other hand, yield significant chaotic regions (Fig. 19) and, potentially, global chaos. The generic composition of the flow topology (i.e. KAM tori and chaos) nonetheless is essentially the same in all cases.

The generality of KAM tori as key LCSs in 3D steady container flows – and the dynamic analogy with periodic duct flows – admits further substantiation by an entirely different (industrial) example involving (global) body forcing: electro-magnetic stirring of glass melts [110].¹³ This relies on buoyancy (induced by Joule heating via an electric current) in conjunction with a Lorentz force (induced via interaction of said current with an external magnetic field). Fig. 20 gives the particular configuration for a cylindrical container: a central (gray rod) and outer (cylinder wall) electrode set up a radial electric current \vec{J} ; external magnets (not shown) create a vertical magnetic field \vec{B} that (together with \vec{J}) yield a (volumetric) Lorentz force

$$\vec{F} = \vec{J} \times \vec{B}, \quad (12)$$

with a dominant azimuthal component. Joule heating only ($\vec{B} = \vec{0}$) results for sufficiently strong \vec{J} in a steady buoyancy-driven circulatory flow with a topology that consists entirely of two families of tori symmetric about the vertical midplane

¹³Electro-magnetic stirring is in fact a common technique for processing of liquid metals. However, this occurs (unlike glass melts) under *turbulent* flow conditions and thus is beyond the present scope [117].

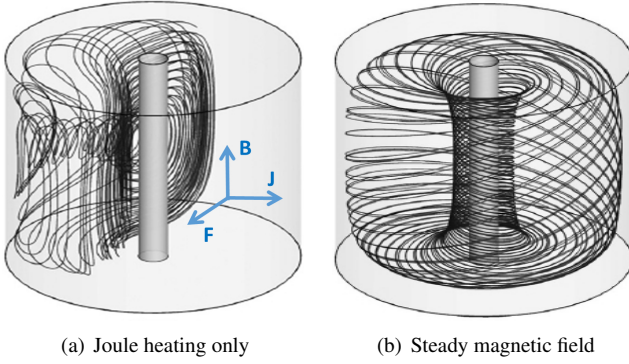


Fig. 20. Electro-magnetic steady stirring of glass melt in cylindrical container by Lorentz force \vec{F} due to radial current \vec{J} between central rod and cylinder wall and vertical magnetic field \vec{B} : (a) one torus of two tori families symmetric about vertical midplane for Joule heating only ($\vec{B} = \vec{0}$); (b) one torus of single tori family centered on cylinder axis for electro-magnetic case ($\vec{B} \neq \vec{0}$). Adapted from [110].

following Fig. 20(a) (shown is one torus of one family described by a single streamline). Activation of the magnetic field ($\vec{B} \neq \vec{0}$) changes this completely into a steady swirling flow and corresponding topology of one global family of tori centered on the central electrode (Fig. 20(b)) [110]. KAM tori nonetheless persist as the topological building blocks and their arrangement is similar to that of the individual families in the above impeller-driven flows (Fig. 18 and Fig. 19). However, an essential difference with the latter is (at least in the considered parameter ranges) the absence of (local) chaotic advection; this requires unsteady electro-magnetic stirring and is addressed below.¹⁴

The above concerns practical utilisations of Lagrangian transport seeking to accomplish chaotic advection for the purpose of efficient mixing and dispersion. KAM tori, in their capacity as barriers to fluid transport, are detrimental to this process. However, industrial batch processing often aims at solid-liquid separation in suspensions of finite-size particles for e.g. waste-water treatment or biorefinery. KAM tori offer a way to realise such “unmixing” for (at least) small particles slightly lighter than the bulk fluid by exploiting the fact that they closely (yet not exactly) follow the fluid parcels. The weak deviation in Lagrangian motion namely has a remarkable effect by causing such particles to migrate towards KAM tori and thus cluster there. This “unmixing” is demonstrated experimentally in Fig. 21 for the above steady flow driven by a single Rushton impeller via the clustering of polystyrene particles suspended in glycerin in the KAM tori at the impeller (Fig. 19(a)) [44]. Fig. 1(a) shows individual particle trajectories in this process.

The particle behaviour in Fig. 21 stems from the fact that the Lagrangian dynamics, though also described by a kinematic equation as (2), is determined by a particle velocity \vec{v} instead of the fluid velocity \vec{u} . The fundamental difference between both fields is that the former is non-solenoidal,

¹⁴This is largely inherent in the particular configuration, though. Buoyancy alone may (in 3D steady container flows) namely already yield intricate flow topologies with multiple tori families and chaotic regions [118].

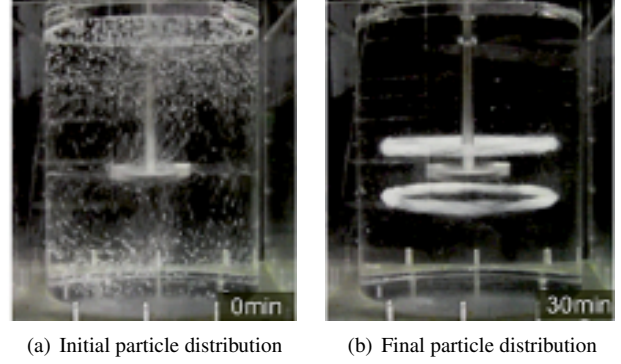


Fig. 21. Impeller-driven “unmixing” of inertial particles in fluid flow in cylindrical container by clustering in KAM tori of flow topology. Experimental visualisation using polystyrene particles suspended in glycerine. Reproduced from [44].

i.e. $\vec{\nabla} \cdot \vec{v} \neq 0$, and its (asymptotic) dynamics, in consequence, is governed by so-called “attractors”, that is, LCSs associated with \vec{v} onto which the particles converge in the course of time. Such entities are absent in solenoidal flows and thus non-existent for the Lagrangian flow topology underlying the fluid motion. However, an intriguing connection occurs in that the attractors for the particular kind of particles considered here are in fact the KAM tori [119]. This gives rise to the “unmixing” of particles shown in Fig. 21. General criteria for particle clustering in LCSs are developed in [120].

Steady flow driven by surface forcing Flows in a cylindrical cavity due to rotating or translating lids are representative examples of surface-driven flows and are 3D counterparts of the 2D lid-driven cavity flow introduced in Sec. 2. The flow and transport characteristics depend essentially on the specific lid motion (i.e. rotating versus translating) and time signature (i.e. steady versus unsteady).

Steady *rotation* of the bottom lid gives rise to a swirling flow and associated flow topology comparable to the steady impeller-driven and electro-magnetically-driven flows in Fig. 18 and Fig. 20(b), respectively: a family of KAM tori centered on the cylinder axis and surrounded by chaos. This is demonstrated experimentally in Fig. 22 by the time-averaged light intensity emitted by a fluorescent dye in a vertical cross-section; its level sets (differentiated by colour) expose the characteristic island structure including localised LCSs as the indicated period-2/3/4 island chains [121]. Moreover, this reveals a progressive breakdown of tori into chaos with increasing Reynolds number Re .

Steady *translation* of the bottom lid yields a circulatory flow consisting of two symmetric vortices similar to the buoyancy-driven flow in Fig. 20(a) [122, 123]). Fig. 23 demonstrates the emergence of the corresponding flow topology by a typical streamline in case of translation in $+x$ -direction. The non-inertial limit $Re = 0$ yields a closed streamline (Fig. 23(a)) that, upon introduction of fluid inertia, becomes non-closed and describes a torus as shown for $Re = 10$ in Fig. 23(b). Thus two global families of tori separated by the symmetry plane $y = 0$ are created for

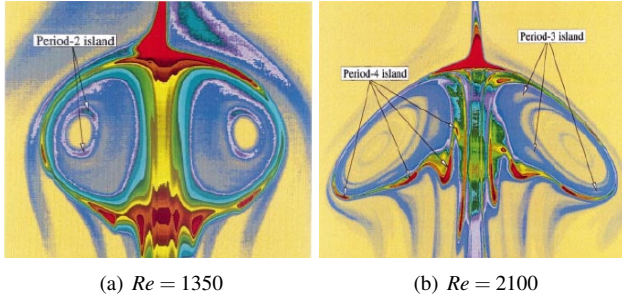


Fig. 22. Lagrangian flow topology in steady swirling flow in cylinder driven by *rotation* of bottom wall. Shown are vertical cross-sections of KAM tori and higher-order tori (indicated by period-2/3/4 islands) for given Re as visualised experimentally by level sets of fluorescence intensity. Reproduced from [121].

“sufficiently small” Re . The streamline becomes chaotic upon further increasing Re , as demonstrated for $Re = 100$ in Fig. 23(c), signifying breakdown of certain tori and resulting in KAM tori embedded in chaos (outlined by the corresponding cross-section with the plane $x = 0$ in Fig. 23(d)) similar as the above rotating-lid case (Fig. 22). The flow field and streamline pattern are validated experimentally by 3D PTV in [124, 125]. Single-wall forcing of *cubical* cavities yields essentially the same flow topology as in Fig. 23, implying, similar as the previous impeller-driven flows, an only secondary importance of the specific geometry [123]. Moreover, forcing by multiple walls or wall segments typically induces bifurcations into more complex topologies yet nonetheless with a generic composition of (multiple) families of tori embedded in chaos [126, 127].

The transition of the flow topology from a global family of closed streamlines in the non-inertial limit $Re = 0$ to two global families of tori, as demonstrated for a generic streamline in Fig. 23, happens for any $Re = 0^+$. Moreover, other minute perturbations of the non-inertial limit as e.g. asymmetric forcing have the same effect [126, 128]. Thus the response of the steady cylinder flow to fluid inertia in fact reflects universal behaviour. Flow topologies in *any* system consisting entirely of closed streamlines namely constitute a singular limit in that the slightest perturbation induces transition into (multiple families of) tori that robustly survive a finite perturbation strength (here $Re \lesssim 10$) [129, 130]. The impeller-driven flow in Fig. 18 exhibits this behaviour e.g. as a function of the tilt angle α : aligned impellers ($\alpha = 0$) yield closed circular streamlines about the cylinder axis; tilting ($\alpha \neq 0$) results in tori formation as in Fig. 23. Hence, given realistic systems are inherently imperfect, tori are the LCSs that make-up the “true” non-chaotic baseline topology of both the cylinder flow and the other cases considered so far as well as most of the configurations discussed hereafter. Flows in micro-droplets are, for instance, a further manifestation of this scenario (Sec. 3.4.2).

A practical instance of 3D steady container flows driven by translational surface forcing, though not immediately apparent, exists in micro/nano-particle separation in micro-fluidic channel flows driven by AC electro-osmosis (ACEO)

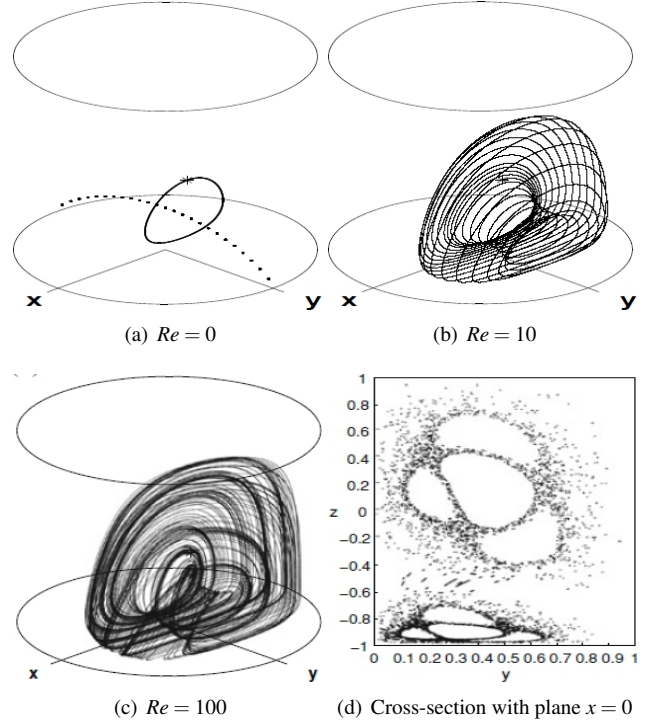
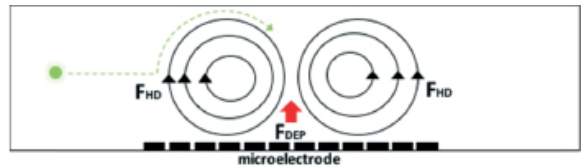


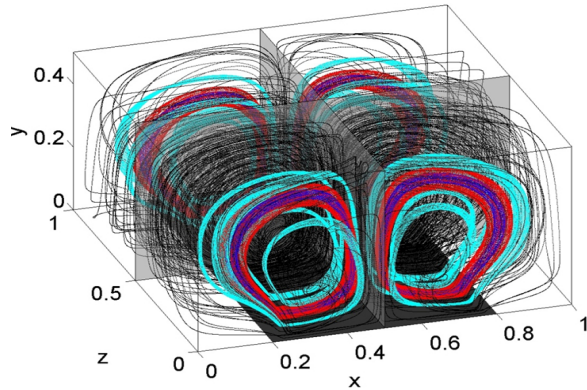
Fig. 23. Lagrangian flow topology in steady cylinder flow driven by *translation* of bottom wall in $+x$ -direction: (a-c) emergence and progressive disintegration of two families of tori symmetric about mid-plane $y = 0$ with increasing Re as visualised by simulated single streamline; (d) vertical cross-section with plane $x = 0$ exposing KAM tori embedded in chaos. Reproduced from [131].

[132]. Fig. 24(a) illustrates the working principle: micro-electrodes at the channel bottom induce a slip velocity in the electric double layer (EDL), setting up vortices that trap and concentrate particles by the resulting centrifugal forces (\vec{F}_{HD}). The local dielectrophoretic force (\vec{F}_{DEP}) at the electrode centre supports this process by pushing particles into the bulk flow. The ACEO-driven flow is dynamically equivalent to said container flows: (i) separatrices between adjacent vortices effectively compartmentalise the channel into confined domains; (ii) the EDL has a negligible thickness and the slip velocity thus effectively acts as an elastic translating wall. Fig. 24(b) gives the 3D flow topology associated with each electrode (dark patch) [128]. This exposes a composition of KAM tori (3 specimens highlighted in colour) and chaotic streamlines (black) within each of the compartments bounded by the separatrices (transparent planes) that is indeed similar to the lid-driven container flow in Fig. 23.¹⁵ Measurements of the 3D streamline pattern by astigmatism μ -PTV (Fig. 24(c)) provides the first experimental validation of this structure [133]. Here dark/light blue streamlines remain within the subdomains divided by the separatrix at $x = 35 \mu\text{m}$ (transparent plane). Red streamlines cross this separatrix due to experimental imperfections

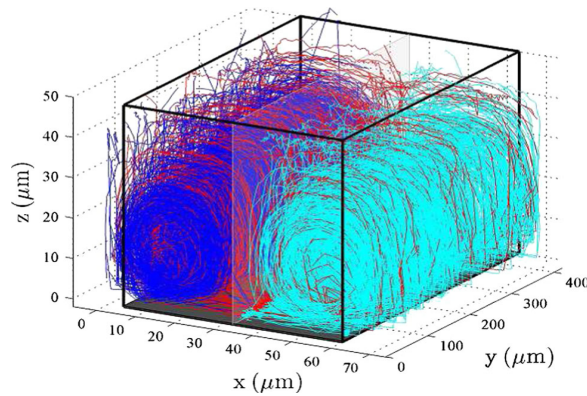
¹⁵The ACEO-driven flow is non-inertial ($Re = 0$); here asymmetric slip velocity induces the universal tori formation from closed streamlines and their (local) breakdown into chaos demonstrated in Fig. 23 [128].



(a) Working principle



(b) Simulated 3D flow topology



(c) Experimental 3D streamline portrait

Fig. 24. Trapping of nano-particles in ACEO-driven vortical microfluidic flow as practical instance of steady lid-driven container flow: (a) particle trapping by interplay of centrifugal (\vec{F}_{HD}) and dielectrophoretic (\vec{F}_{DEP}) forces (adapted from [132]); (b) simulated 3D flow topology comprising of KAM tori (coloured) embedded in chaos (black) (adapted from [128]); (c) 3D streamline pattern measured by astigmatism μ -PTV (reproduced from [133]).

that, akin to tori formation from closed streamlines, act as natural perturbations of an idealised state. Essentially the same perturbation-induced separatrix crossing may occur in droplet flows (Sec. 3.4.2) and convection cells (Sec. 3.5.2); its underlying mechanisms are elaborated in Sec. 3.4.2.

The ACEO-driven flow is situated in a duct and thus admits transport characteristics of both duct and container flows. Imposition of an axial (x -wise) pressure gradient of “appropriate” strength sets up a throughflow that passes over the vortical structures shown in Fig. 24(b) and thus yields a flow topology comprising of (diminished) tori at the electrode and stream-wise tubes as in Fig. 7(a) surrounded by a chaotic region [128]. Tracers in this chaotic region exhibit both container-flow and duct-flow dynamics by prolonged

entrapment in the vortical structure during their excursion from inlet to outlet. Similar hybrid behaviour occurs also in the flow inside an aneurysm shown in Fig. 1(b) and is examined further in Sec. 3.3.3.

Unsteady flows Dependence of the flow \vec{u} on time t expands the phase space of kinematic equation (2) from the 3D physical domain to the 4D space-time domain. This affords greater dynamic freedom and generically tends to promote chaotic advection. Reconsider for illustration the flow inside a cylindrical container driven by a rotating disk (Fig. 18). Stirring of a Newtonian fluid yields a steady flow and corresponding flow topology consisting of KAM tori embedded in chaos (Fig. 18). Tilting of the disk is imperative to attain this state; alignment with the cylinder axis yields a topology devoid of chaos and comprising entirely of tori [114]. (Recall that this constitutes the “true” baseline topology emanating from a singular state consisting of closed streamlines.) Non-Newtonian fluid rheology may fundamentally change the latter by (for *steady* stirring) inducing *time-periodic* oscillations and, in consequence, richer dynamics. Fig. 25(a) demonstrates this for a fluid exhibiting both visco-elastic and shear-thinning behaviour stirred by a rotating disk aligned with the cylinder axis [134]. Shown is a typical instantaneous dye distribution in the vertical cross-section that visualises the mixing pattern and thus outlines the LCSs in the corresponding stroboscopic map as in Fig. 5. The emergence of “rippled” structures (green) enveloping islands (blue/yellow) implies a 3D flow topology of KAM tori and chaos basically similar to that emanating from the tilted disk (Fig. 18(c)) and the single Rushton impeller (Fig. 19(a)) for Newtonian fluids. Thus unsteadiness promotes chaos in a comparable way as a non-trivial geometry in said steady flows. Here in particular the high-shear region around the impeller (indicated by red in Fig. 25(a)) is the physical cause of the rheology-induced time-periodicity.

Introduction of time-periodicity in the electro-magnetic stirring of glass melts by an oscillating magnetic field in Fig. 20 has essentially the same effect: breakdown of the global family of tori in Fig. 20(b) into chaos. Fig. 25(b) demonstrates this by the resulting global dispersion of 25,600 tracers released on a small line segment of length $l/R = 0.02$ in the axial midplane (top view) [110]. First experimental evidence of 3D chaos in unsteady flows such as those in Fig. 20(b) has been obtained by direct measurement of 3D stroboscopic maps of a single tracer via combined 2DPTV in two projections in a time-periodic swirling flow driven by alternate eccentric rotation of upper and lower endwalls [135].

The above container flows, notwithstanding substantial differences in configuration and forcing, in essence all concern cases in which the Lagrangian dynamics are inextricably linked to the emergence and breakdown of KAM tori. This renders these flows dynamically analogous both to one another and to periodic duct flows with behaviour that, in general, is similar to that of 2D unsteady systems. The link with 2D systems is broken only near possible singularities in transformation (11) and/or upon development of 3D defects

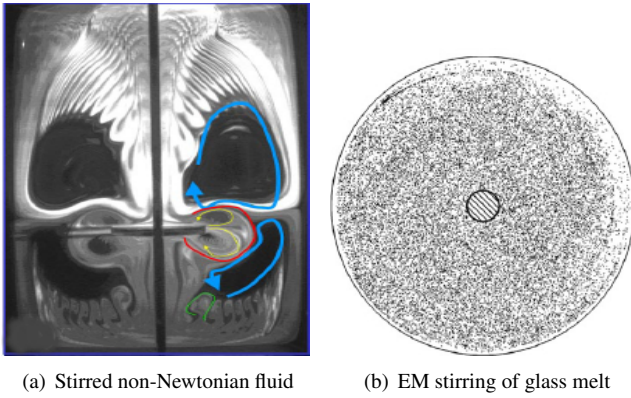


Fig. 25. Impact of unsteady flow on Lagrangian dynamics: (a) emergence of “rippled” structures (green) around tori (blue/yellow) signifying chaos in rheology-induced time-periodic cylinder flow driven by rotating disk (red indicates high-shear region) visualised experimentally by dye (adapted from [134]); (b) onset of global chaos due to time-periodic electro-magnetic (EM) stirring of glass melt visualised by computational stroboscopic map (reproduced from [110]).

in KAM tori (Sec. 4.6.2).

However, 3D unsteady flows admit far greater richness beyond that shown above and its exploration is still incomplete [49, 43]. Fig. 26(a) demonstrates this by 3D time-periodic flows constructed from reorientations of the steady lid-driven cylinder flow in Fig. 23 (for Stokes limit $Re = 0$) by piece-wise steady translation of endwalls according to certain protocols. (Numbered arrows indicate the sequence of periodic wall translations.) Shown stroboscopic maps correspond with a *single* tracer released in a given flow and expose intensifying “levels” of (chaotic) dynamics: 2D chaos restricted to spheroidal surfaces (left); quasi-2D chaos in layers (centre); global 3D chaos (right) [136]. (Dye visualisations experimentally validate these basic “dynamic levels” of 3D Lagrangian transport [124, 137].) The second case concerns a topology of KAM tori (outlined by the “holes” in the stroboscopic map) embedded in chaos and thus belongs to the beforementioned class. The first and third cases, on the other hand, reflect essentially different situations.

Lagrangian motion is in Fig. 26(a) (left) restricted to spheroids (shown is one specimen of a continuous family) and in consequence qualitatively deviates from that on KAM tori. (Refer to Sec. 4.4 for the mechanisms behind the spheroids and the intrinsically 2D dynamics.) Tori generically accommodate spiralling trajectories (as e.g. the magnetic field lines in Fig. 17(a)) due to an interplay of poloidal and toroidal circulation. The fundamentally different topology of spheroids precludes such double circulation and dictates dynamics equivalent to that of 2D confined unsteady flows (Sec. 4.4.2). Hence spheroids generically contain islands and chaos as e.g. the lid-driven cavity in Fig. 5.¹⁶

¹⁶This is a consequence of the domain topology. Brouwer’s well-known fixed-point theorem states that time-periodic flows in *convex* domains have (at least one) periodic point(s) following (6) [138]. Spheroids and 2D confined domains (as the lid-driven cavity) are convex domains and, by virtue of said theorem, both have flow topologies consisting of periodic points and

Global chaos as in Fig. 26(a) (right) sets in after total breakdown of transport-obstructing LCSs as e.g. KAM tori or spheroids in response to some perturbation. The topology of such states generically consists of (multiple) isolated periodic points (6) and associated manifolds that, due to the 3D nature of the flow, materialise as surface–curve pairs. This is exemplified in Fig. 26(b) by the 2D stable (convoluted surface) and 1D unstable (convoluted curve) manifolds of an isolated periodic point (not shown) in the globally-chaotic state that ensues from disintegration of said spheroids due to significant fluid inertia ($Re = 100$) [139].

Intermezzo: toroidal versus spheroidal “route to chaos”

The particular “route to chaos” depends on the kind of LCSs constituting the baseline topology. The above findings imply that – from a *dynamical* perspective – two canonical cases can be distinguished: baseline topologies consisting of (i) tori and (ii) spheroids.¹⁷ Disintegration of KAM tori in both steady and unsteady 3D flows often (including the previous examples) follows the quasi-2D route dictated by their equivalence with 2D unsteady systems: progressive breakdown of tori into chaos with increasing perturbation according to well-defined scenarios (Sec. 4.2). However, 3D systems may furthermore follow two essentially 3D “routes to chaos” associated with tori and spheroids. This is elaborated below.

Tori may under certain conditions develop local defects that enable “jumping” of tracers between tori and, in consequence global dispersion. Such defects (locally) break the link with 2D unsteady systems and thus cause essentially 3D behaviour (Sec. 4.6.2). The study in [129] investigates this for the time-periodic flow inside the 3D annular region between two concentric spheres driven by their co-axial rotation about axis $\vec{r} = \cos(\alpha)\vec{e}_z + \sin(\alpha)\vec{e}_x$, with α alternating between $\alpha = 0$ and $\alpha = 1^\circ$. The base flow ($\alpha = 0$) consists (for sufficiently small $Re > 0$) of a primary (θ -wise) circulation about the z -axis ($\vec{r} = \vec{e}_z$) and a weak secondary circulation in the rz -plane [143]. The corresponding streamlines describe two families of tori (with a dense poloidal winding) centred on the z -axis and symmetric about plane $z = 0$ following Fig. 27(a) (left), implying a flow topology qualitatively the same as the steady cylinder flow in Fig. 23(b). The time-periodic flow, due to the only minute reorientation of the base flow during rotation about the tilted axis ($\alpha = 1^\circ$), yields a stroboscopic map consisting of basically the same tori as the base flow (Fig. 27(a); left). The principal difference is the emergence of defects in the tori that enable said “jumping” as demonstrated in Fig. 27(a) (left) by the cross-sectional stroboscopic map of a *single* tracer. This results in a gradual global dispersion due to intermittent dynamics comprising of circulation *along* and jumping *between* tori at

associated LCSs. Moreover, periodic points preclude double circulation.

¹⁷Shown examples suggest that baseline topologies in realistic flows generically consist of either tori or spheres yet in principle more complex situations are possible. Studies on kinematic models emulating 3D time-periodic flows demonstrate that a range of closed invariant surfaces of intricate shape accommodate essentially the same (chaotic) dynamics as encountered on spheroids [140]. Similar studies demonstrate that tori in 3D systems with non-trivial coexistence and nesting of multiple tori families behave the same as in simpler (canonical) configurations [141, 142].

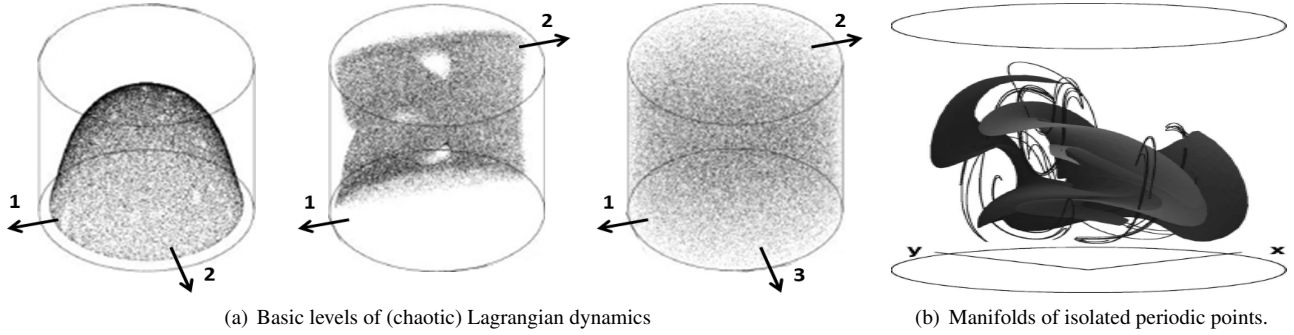


Fig. 26. Richness of Lagrangian dynamics in realistic 3D unsteady (container) flows demonstrated for time-periodic cylinder flow driven by step-wise steady translations of endwalls: (a) basic dynamic levels exposed by time-periodic Stokes flow ($Re = 0$) due to given forcing protocols (numbered arrows indicate period-wise sequence of wall translations) visualised by computational stroboscopic map of single tracer (adapted from [136]); (b) 1D (curve) and 2D (surface) manifold of isolated periodic point in global chaotic sea ensuing from breakdown of invariant spheroids in panel (a) (left) by fluid inertia ($Re = 100$) (reproduced from [139]).

local defects (indicated by dashed semi-circles).

The mechanism causing the defects is the local synchronisation of the dynamics with the time-periodic forcing: the poloidal (ϕ) and toroidal (φ) angles of certain tracers (in the local toroidal reference frame) evolve with rotations $\omega = \omega(\vec{x}_0)$ and $\gamma = \gamma(\vec{x}_0)$ relating via rational fractions, i.e.

$$\phi_p = \phi_0 + p\omega, \quad \varphi_p = \varphi_0 + p\gamma, \quad \omega/\gamma = m/n, \quad (13)$$

where m and n are integers. They describe trajectories that reconnect after n toroidal windings. Tracers exhibiting such “resonance” prevent neighbouring trajectories from densely filling the entire torus and thus cause local defects (refer to Sec. 4.6.2 for the basic mechanisms). Here this occurs in surfaces termed “resonance sheets”; these sheets are unstable and under arbitrarily small perturbation disintegrate into localised chaotic zones that interrupt the poloidal circulation within tori and thus enable random jumps between them. This results in global transport following Fig. 27(a) (right) and is aptly termed “Resonance-Induced Dispersion” (RID) [129]. The actual jumps in RID are facilitated by localised versions of global manifolds similar to Fig. 26(b) corresponding with isolated periodic points (6) that remain from the disintegrated resonance sheets [130].

Circumstantial experimental evidence of RID is obtained by the dispersion properties of fluorescent tracer particles in convection cells (Sec. 3.5.2) [144]. Moreover, RID has a direct counterpart in 3D steady flows in global dispersion following Fig. 27(a) (right) enabled by local defects in tori induced by poloidal/toroidal evolutions

$$\phi(t) = \phi_0 + \omega t, \quad \varphi(t) = \varphi_0 + \gamma t, \quad (14)$$

with ω and γ forming rational fractions following (13) [145]. The notion of resonance furthermore generalises to defects in tori caused by significant slow-down of Lagrangian motion.¹⁸ This e.g. underlies the separatrix crossing in the

ACEO-driven flows, droplets flows (Sec. 3.4.2) and convection cells (Sec. 3.5.2).

Spheroids may also develop local defects due to resonances yet fundamental disparities exist with tori on grounds of the different topology and dynamics. Key is the formation of periodic lines through coalescence of isolated periodic points (6) in the case of spheroids. These lines intersect the spheroids as illustrated in Fig. 27(b) (left) for the two-step forcing by the bottom wall in Fig. 26(a) (left). (Such points – and thus the resulting periodic lines – always exist on account of Brouwer’s fixed-point theorem. Tori, on the other hand, are generically devoid of periodic points, which sets them fundamentally apart from spheroids [139].) The impact of periodic lines on the response to weak perturbation depends fundamentally on the nature of the associated LCSs: chaotic seas (demarcated by manifolds of the individual points on hyperbolic line segments) survive as thin shells; islands (centered on individual points of elliptic line segments) coalesce into tubes. Resonance here ensues from the isolated degenerate periodic points (termed “parabolic points”) that partition the periodic line into elliptic and hyperbolic segments and (instead of causing local defects in otherwise complete tori as in RID) results in *truncation* of the *entire* tube. Shells and truncated tubes thus formed merge into intricate LCSs and this process is therefore termed “Resonance-Induced Merger” (RIM). RIM is also an essentially 3D phenomenon by, similar to RID, breaking the link with 2D unsteady systems (again refer to Sec. 4.6.2 for the basic mechanisms).

Fig. 27(b) (right) demonstrates RIM due to perturbation of the flow topology in Fig. 27(b) (left) by weak fluid inertia ($Re = 0.1$), with heavy and normal curves indicating ellip-

called “averaging principle”, which assumes motion along trajectories that (i) causes tracer positions to densely fill them over time and (ii) is significantly larger than the drift induced by the perturbation [146]. These assumptions break down near resonances as well as in slow-motion regions and yield local motion in all coordinate directions in the order of the perturbation strength. This results in essentially 3D dynamics that is no longer restricted to tori. Thus slow motion is a generalisation of “true” resonances by (though not strictly precluding) strongly impeding the filling of entire trajectories and, inherently, tori formation. This is further explained in Sec. 4.6.2.

¹⁸ The survival of tori subject to weak perturbation relies on the so-

tic and hyperbolic line segments, respectively, separated by the isolated parabolic points (stars) that underlie resonance here [139, 147]. Shown is the 3D stroboscopic map of a *single* tracer outlining an inner and outer shell connected by two tubes centred on the elliptic line segments. The LCS thus visualised (and formed by merger of shells and truncated tubes) is one member of a family of such LCSs that are arranged concentrically according to the truncated tubes. Hence RIM “creates” new LCSs from existing ones; RID, on the other hand, (partially) destroys LCSs. Moreover, RIM, unlike the random jumps in RID, is a predictable and systematic phenomenon in that families of truncated tubes form on elliptic line segments and merge with shells at tube ends at the well-defined positions of parabolic points. (Segmentation of periodic lines therefore is key to RIM; it cannot occur for single-type lines.) The observation of RIM in other flow configurations as well as direct isolation of periodic lines and tube segments by experimental stroboscopic maps using 3DPTV strongly suggests that RIM is a universal and robust phenomenon in flows with spheroidal LCSs and segmented periodic lines [148, 149, 125, 150].

Important to note is that RIM, though creating rather than destroying LCSs, nonetheless is on a “route to chaos”. Said entities namely, instead of being strictly invariant, effectively constitute regions of prolonged (yet not indefinite) entrapment for (tens of) thousands of periods that in the long run admit global dispersion by accumulated transverse drifting. Moreover, incomplete shells may form that exhibit “leakage” of tracers into 3D chaotic zones [148, 139, 147].

The route to 3D chaos from spheroids, in stark contrast with tori, is (to the best of our knowledge) hardly explored in the literature. However, the above findings as well as the considerations below suggest that this scenario may be relevant specifically for unsteady container flows consisting of reoriented base flows.

Unsteady flows revisited Mixing of granular media in spherical tumblers is an industrial application that (under the premise of continuum-like flow) exhibits spheroidal LCSs and (signatures of) RIM [151]. The configuration is given schematically in Fig. 28(a) and consists of a time-periodic flow in a half-full sphere driven by alternate rotation about x and z -axes. Equal rotation rates yield a flow topology comprising of spheroids and periodic lines and, in consequence, 2D dynamics similar to that in the lid-driven cylinder flow in Fig. 26(a) (left). Fig. 28(b) demonstrates this by the computational stroboscopic map of multiple tracers (distinguished by colour) released within a given spheroid; green/blue curves are periodic lines consisting entirely of hyperbolic/elliptic points and intersect the spheroid at the chaotic sea and centre of the two opposite islands (outlined by circular orbits). Slight deviation in rotation rates triggers a similar response as weak fluid inertia in the cylinder flow: the chaotic sea forms a thin shell; islands of adjacent spheroids coalesce into tubes. Fig. 28(c) demonstrates former and latter by weak drifting transverse to the spheroid and incipient spiralling about the elliptic line (blue), respectively, resulting in a “fuzzier” stroboscopic map. These dynamics are

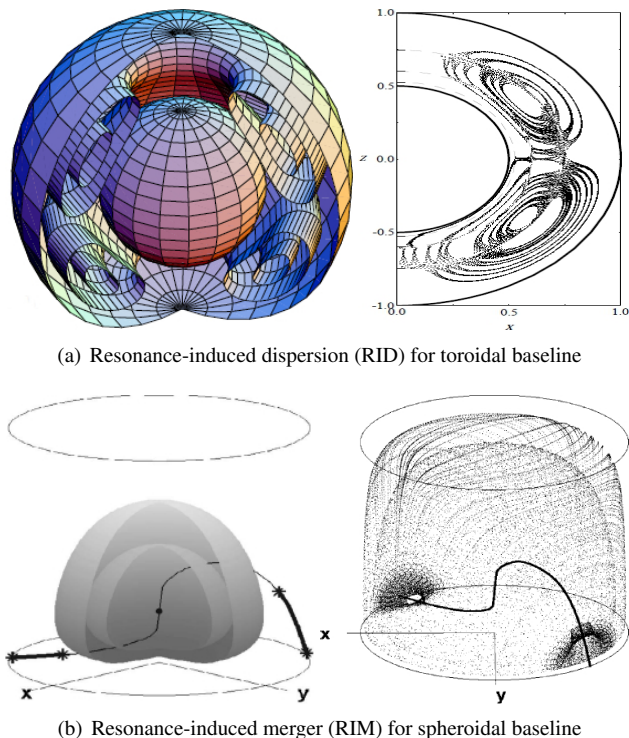


Fig. 27. 3D “routes to chaos” for baseline topologies of tori versus spheroids: (a) global dispersion in time-periodic flow between two concentric spheres due to defects in tori (left) visualised by cross-sectional stroboscopic map of single tracer (right) (reproduced from [129]); (b) formation of intricate LCSs in time-periodic lid-driven cylinder flow by merger of truncated tubes forming on elliptic (heavy) segments of periodic lines and shells forming on chaotic spheroid sectors (left) due to weak fluid inertia ($Re = 0.1$) visualised by 3D stroboscopic map of single tracer (right) (reproduced from [139]).

clear signs of RIM and, though actual tube-shell merger as in Fig. 27(b) is not investigated in [151], thus strongly suggest that the spherical tumbler follows this route to 3D chaos upon perturbation by varying rotation rates. An important outstanding question is whether the periodic lines (in appropriate parameter regimes) admit the segmentation into elliptic and hyperbolic segments that is essential to RIM.

Unsteady transport phenomena as exemplified above are yet to find their way into analysis, design and technological development of other industrial applications. However, accomplishment of 3D global chaos as in Fig. 26(a) (right) by time-periodic agitation of industrial batch mixers may significantly boost performance compared to conventional steady stirring that (implicitly) relies on effectively 2D chaos due to breakdown of tori (Fig. 18 and Fig. 19). Novel concepts such as glass processing by time-periodic electro-magnetic stirring (Fig. 25(b)) take important first steps in this direction.

Micro-fluidic devices and emerging technologies that involve batch processing may particularly benefit from (insights into) unsteady Lagrangian transport and chaos due to the high degree of flexibility and control offered by micro-fluidic forcing techniques and domain shapes. Proper elec-

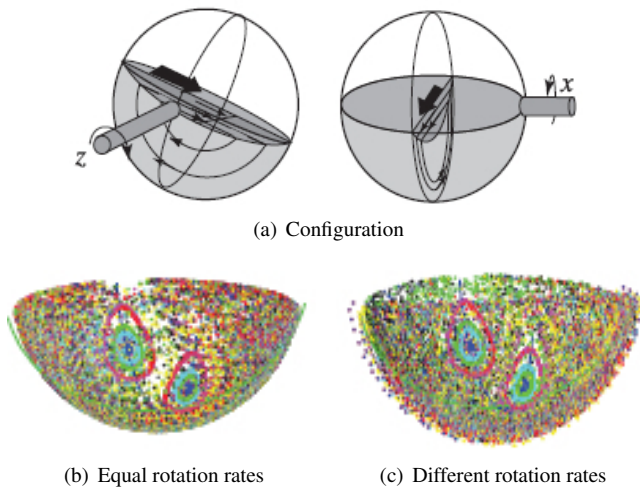


Fig. 28. Signatures of RIM in mixing of granular media by time-periodic flow in half-full spherical tumbler driven by alternating rotation axes: (a) configuration; (b) 2D (chaotic) dynamics within spheroids for equal rotation rates; (c) tube and shell formation due to slight deviation in rotation rates. Adapted from [151].

trode layouts and (time-periodic) activation in ACEO-driven flows e.g. enable systematic reorientations of the steady “base flow” in Fig. 24(b) so as to create various flow and transport conditions in micro-channels similar to the cylinder flow (Fig. 26) including (in principle) delicate processes such as RIM (Fig. 27(b)). Suspended magnetic nano-particles facilitate well-controlled body forcing reminiscent of the above electro-magnetic glass processing for basically any liquid and find first applications for batch mixing in microfluidic platforms for biomedical and diagnostic purposes [109, 112]. The latter employ time-periodic magnetic forcing to accomplish chaotic advection and incorporation of essentially 3D insights may enable further (technological) development of such devices. Moreover, this may enable new (diagnostic) functionalities by systematically creating and utilising LCSs for e.g. particle trapping and/or separation similar to Fig. 21.

3.3.3 Relevance beyond industry

Lagrangian (chaotic) transport in 3D container flows also play a central role in many (seemingly disconnected) non-industrial flow situations and thus have fundamental similarities with the systems considered above. This is, as for duct flows (Sec. 3.2.3), again illustrated via examples.

Aneurysms Aneurysms are balloon-like malformations of blood vessels that, upon rupturing, lead to internal bleeding with potentially lethal consequences. Transport of blood-borne substances is a key player in this process and in particular chaotic advection (induced by the anomalous shape of aneurysms) has been implicated in the promotion of cardiac diseases (Sec. 3.1 and 3.2.3). The typical flow in aortic aneurysms is visualised experimentally in Fig. 1(b) by 3D Lagrangian trajectories and consists of a vortical structure within the aneurysm (open arrows) driven by the passing aortic flow (closed arrows) [45]. Fig. 29(a) substanti-

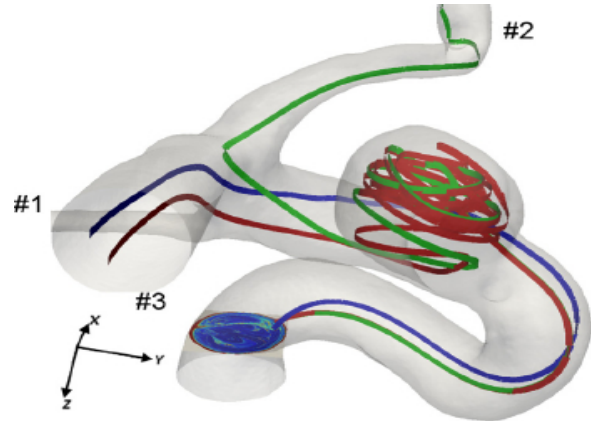
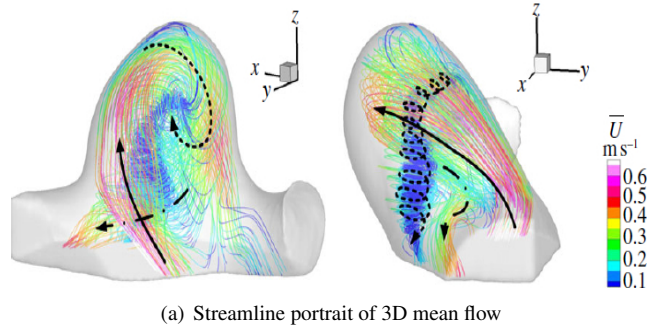


Fig. 29. Flow in cerebral aneurysm as physiological instance of time-periodic lid-driven container flow: (a) streamline portrait of 3D mean flow over cardiac cycle exposing inflow jet (solid arrow), vortical internal flow (dotted arrow) and outflow (dashed arrow) (reproduced from [152]); (b) hybrid duct/container-flow character of Lagrangian dynamics demonstrated by 3 tracer paths (distinguished by colour) released at inlet cross-section (reproduced from [153]).

ates this generic structure by the 3D streamline portrait of the cyclic mean velocity field in a laboratory replica of a cerebral aneurysm constructed from 2D stereo-PIV measurements [152]. This exposes a similar vortical interior flow (dotted arrow) as well as the local in/outflow (solid/dashed arrow) at the attachment to the cerebral artery that drives the former. Thus the flow in the aneurysm resembles the above time-periodic lid-driven cylinder flow by consisting of a re-orientation of a circulatory base flow akin to Fig. 23 forced at its boundary; a non-essential difference is that the flood flow varies continuously (instead of step-wise) during each cardiac cycle. This resemblance implies unsteady 3D (chaotic) transport and its exploitation offers a way to investigate and unravel this process in aneurysms so as to deepen insights into their origins and implicated vascular diseases as thrombosis and atherosclerosis (Sec. 3.1).

A further analogy exists in the larger configuration of aneurysm and blood vessel combined. This situation is comparable to the previous ACEO-driven flow in conjunction with a main throughflow, implying similar interactions between subregions of the vortical flow in the aneurysm and the main blood stream and, in consequence, similar hybrid behaviour including both duct-flow and container-flow char-

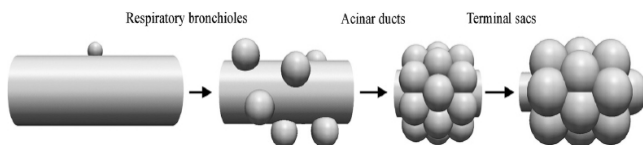
acteristics. The computational study by [153] investigates such 3D Lagrangian transport in the 3D time-periodic flow in a cerebral aneurysm induced by the cardiac cycle using a realistic geometry based on CT angiography. Fig. 29(b) shows typical Lagrangian trajectories (distinguished by colour) of three initially close fluid parcels released at the inlet of the single ingoing blood vessel. (The cross-sectional distribution at the inlet gives the residence time of a dense set of parcels released here.) The parcel dynamics nicely demonstrates (i) said hybrid behaviour of prolonged entrapment in the vortical structure inside the aneurysm during excursion from inlet to outlet and (ii) its essentially chaotic nature by the rapid separation of the trajectories. Chaotic trajectories in the above ACEO-driven flow exhibit exactly the same behaviour [128].

Fig. 29(b) exposes a further ramification of chaotic advection specific for the aneurysm flow: deflection of trajectories into different outgoing blood vessels (labelled 1–3). Such random distribution over multiple branches is in fact an important mechanism for both local and global dispersion in (random) porous media (Sec. 3.5.2) including cardiovascular networks (Sec. 3.5.3).

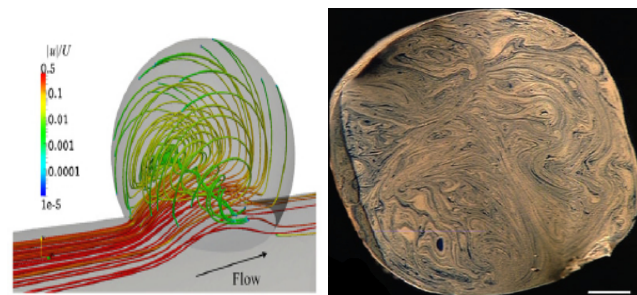
Lung alveoli Flow and transport within the lungs, though physiologically entirely different, intimately relates to the above aneurysms. Air enters the lungs via the respiratory bronchioles, passes through the acinar ducts and ends in the terminal sacs (Fig. 30(a)). These airways become increasingly populated with hemispheroidal protrusions denoted “alveoli” that release air into the bloodstream. The internal flow is primarily driven by the passing ductal flow and the configuration thus resembles that in aneurysms and, in turn, the time-periodic lid-driven cylinder flow. Compare to this end the simulated instantaneous 3D streamline pattern inside an alveolus in Fig. 30(b) with Fig. 23 and Fig. 29(a). The similarity in flow configuration furthermore implies interaction between alveolic and throughflow akin to that in aneurysms and, inherently, hybrid dynamics in the chaotic regions as demonstrated in Fig. 29(b).

Aerosol mixing and deposition in the alveoli is essential to the overall functioning of the lungs and motivated a range of studies on Lagrangian transport in the pulmonary acinus [154, 155, 156, 30, 157]. This gave the key insight that chaotic advection, in stark contrast with its adverse effect in aneurysms, is vital for the kinematic irreversibility necessary to achieve net aerosol transport during each breathing cycle. Fig. 30(c) experimentally validates stretching and folding – signifying chaotic advection – in the airways by visualisation the cross-sectional mixing pattern using two polymerised liquids of different colour driven through the bronchial tree of rat lungs by mechanical ventilation [156]. The majority of these studies considers 3D steady flow in an axi-symmetric alveolus wrapped around a bronchiolus, implying a toroidal geometry and, inherently, essentially 2D unsteady dynamics equivalent to that of periodic duct flows (Sec. 3.2). Moreover, the explicit links with Lagrangian concepts established in [30] also adopt this configuration.

The true system, notwithstanding the evident impor-



(a) Schematic structure of airways in lungs



(b) Instantaneous 3D streamlines (c) Cross-sectional mixing pattern

Fig. 30. Aerosol mixing and deposition in lungs as physiological instance of transport in time-periodic container flow: (a) structure of airways; (b) simulated instantaneous 3D streamline portrait in lung alveolus (adapted from [157]); (c) cross-sectional mixing pattern in alveolus visualised experimentally by polymerised liquids of different colour (bar = $500\mu\text{m}$) (reproduced from [156]).

tance of said studies, concerns 3D unsteady dynamics in a container flow driven by translational boundary forcing according to the analogy with aneurysms made before, however. Thus flow and Lagrangian dynamics in alveoli must (on topological grounds) in fact also resemble that of the time-periodic lid-driven cylinder flow. This is supported by computational studies on (instantaneous) 3D streamlines and Lagrangian transport of (finite-size) aerosols in spheroidal configurations [158, 159, 160, 31, 157]. The coherent structures in the instantaneous streamline patterns denoted “Russian nesting dolls” in [31] in particular are directly equivalent to the toroidal streamlines in Fig. 23(c), implying a cross-sectional stroboscopic map of the corresponding time-periodic flow akin to Fig. 23(d). Hence, as for aneurysms, in-depth investigations of the 3D alveolic transport based on the analogy with 3D lid-driven container flows may significantly deepen insights.

Gastric digestion A further physiological example of transport in 3D time-periodic container flows exists in the digestive process inside the stomach. The objective is efficient extraction of nutrients by the mixing and “kneading” of the gastric contents via peristaltic movement of the stomach wall through so-called “antral contraction waves”. These waves periodically compress and expand the stomach and its contents and thus set up a 3D time-periodic flow driven by movement at/of the boundary reminiscent of aneurysms and lung alveoli and, by the beforementioned analogy, 3D lid-driven cavity flows. The main differences with said examples are (i) that the stomach, though topologically again spheroidal, has a more complex shape (Fig. 31(a)) and (ii) involves elaborate forcing by the *entire* boundary. This results in the formation of multiple families of vortical structures

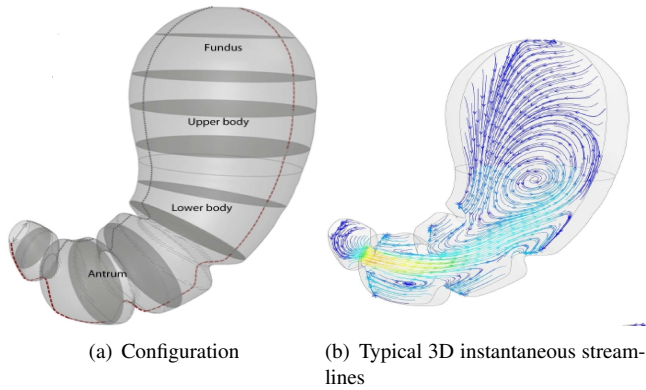


Fig. 31. Gastric digestion as physiological instance of transport in time-periodic container flow: (a) configuration; (b) simulated instantaneous 3D streamline portrait (adapted from [33]);

of varying extent and intensity as exemplified in Fig. 31(b) by typical instantaneous 3D streamlines [33]. The individual structures – particularly in the central part of the stomach – clearly resemble those in Fig. 23(c).

The highly non-trivial interplay of the vortical structures in the course of a period are likely to produce (at least local) chaotic advection and first exploratory studies on simplified systems indeed suggest this [161]. However, the contribution of advective transport to actual gastric mixing remains unclear yet is considered important for better understanding of this process [162]. Hence, this is a further problem that may benefit considerably from insights in 3D Lagrangian transport and analogies with the above systems.

Champagne tasting A perhaps surprising (though appealing) instance of 3D transport in container flows emerges in champagne tasting. Transport and mixing due to the internal flow driven by bubble formation upon pouring into the glass is namely believed key to the exhalation of flavours and aromas and thus the taste of the champagne [163].

Champagne glasses typically have engravings at the bottom as nucleation site for a central column of rising CO_2 bubbles as driver of a cross-sectional circulation in the rz -plane following Fig. 32 (top, left). This is visualised in Fig. 32 by vertical cross-sections of fluorescent dye in a coupe glass (bottom, left) and polymer particles in a flute (bottom, right). The vortical structures thus created are qualitatively similar yet their extent depends on the type of glass [163].

The 3D flow constitutes a vortex ring with a corresponding 3D flow topology reminiscent of that below the disk impeller in Fig. 18 yet with one fundamental difference. The impeller actively imposes uni-directional azimuthal flow and, by virtue of the resulting analogy with periodic duct flows, gives rise to KAM tori and associated chaotic regions (Sec. 3.3.2). The champagne flow, on the other hand, stems from passive internal forcing by the (approximately) axisymmetric bubble column. Its small asymmetric fluctuations induce weak azimuthal flow without one preferential direction and, in consequence, continuous reversal in the course of time. Such dominant cross-sectional circulation in com-

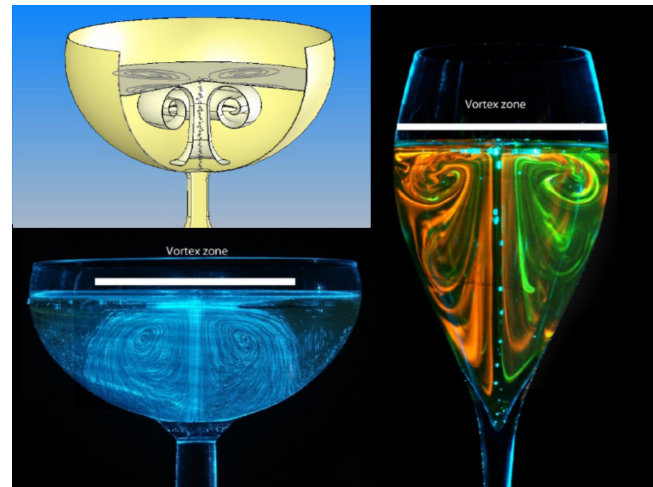


Fig. 32. Flow and mixing in champagne glass as culinary instance of (transport) in 3D container flows: (top, left) cross-sectional circulation driven by central bubble column; (bottom, left) experimental visualisation in coupe glass by fluorescent dye; (bottom, right) experimental visualisation in flute by polymer particles (adapted from [163]).

ination with weak azimuthal fluctuations are in fact key ingredients for resonance-induced defects in tori and, in consequence, RID as in Fig. 27(a) (right). RID namely ensues from weak perturbation of an idealised flow topology consisting of closed streamlines (Sec. 4.6.2). These considerations suggest that transport and mixing in the champagne glass may be highly non-trivial and of unexpected richness. In-depth Lagrangian analysis – with a particular focus on resonance phenomena – enables rigorous exploration of this.

Cilia-driven flows at coral reefs Transport in the cilia-driven flow at polyps in coral reefs shown Fig. 1(c), while, as for the ACEO-driven flow (Sec. 3.3.2), not immediately apparent, intimately relates to flows in containers. The cilia, though strictly in an open domain, namely create a boundary-driven flow in a confined region adjacent to the coral surface consisting of vortical structures comparable to that of the boundary-driven container flows shown in Fig. 23 and Fig. 24(b). This is demonstrated in Fig. 33 for typical flow patterns above coral explants obtained by 2DPTV using powdered coral food as tracer particles [47]. The 2DPTV measurements reveal arrays of vortices with alternating circulation (indicated by white arrows) involving flow speeds ranging from stagnant fluid (blue) to a maximum velocity of $O(1 \text{ mm/s})$ (red). Note in particular the striking resemblance of the pair of counter-rotating vortices in Fig. 33 (right) with the ACEO-driven flow in Fig. 24(b). These analogies imply similar Lagrangian transport as in said container flows.

3.4 Flow in drops

3.4.1 General configuration

Neglecting two-phase effects as drop coalescence and breakup, the flow inside a drop is in a dynamical sense a subclass of flow in containers considered above. They namely both concern confined flows in (topologically) spheroidal do-

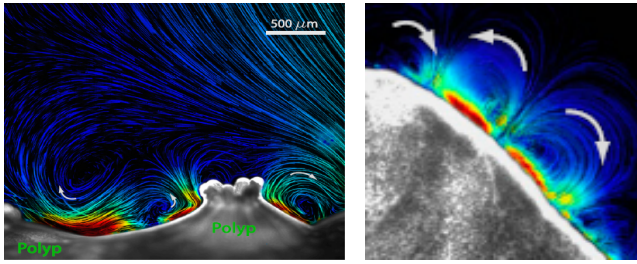


Fig. 33. Cilia-driven vortical flow at coral polyps as biological instance of (transport) in 3D lid-driven container flows demonstrated by typical flow patterns above coral explants visualised experimentally by 2DPTV. Colour represents flow speed (blue: stagnant; red: $O(1 \text{ mm/s})$); white arrows indicate circulation (adapted from [47]).

mains and the corresponding Lagrangian transport thus is subject to the same kinematic and topological constraints. The primary difference with container flows is that drops are bounded by a fluid-fluid interface instead of an (elastic) solid wall and thus offer functionalities (particularly in micro-fluidic systems) such as immersion in a bulk flow and external forcing by techniques unavailable to the former. Hence (potential) technological applications involving drops are entirely different from the above container flow and this motivates its distinction as a separate flow class.

3.4.2 Industrial and technological relevance

Lagrangian transport and mixing in drops is relevant to a range of micro-fluidic applications and emerging technologies. Two basic configurations can be distinguished:

- *Microfluidic networks* Here droplets propagate in an ambient flow through (interconnected) micro-channels and chambers and serve both as processing and transportation vessels. This principle finds application in micro-fluidic devices for batch processing of samples in e.g. pharmaceutical manufacturing or bio-engineering using droplets as chemical reactors or cell incubators so as to boost reaction rates, shield against contamination and/or provide protected environments [164, 165, 166, 167, 168, 169].
- *Digital microfluidic platforms* Here discrete droplets are trapped (and displaced) on solid substrates. Applications of this approach include processing and analysis of microscopic fluid quantities as e.g. chemical synthesis of drugs or immunoassays for clinical diagnostics of minute blood samples [170, 171, 172].

A great diversity of techniques is available for actuation and manipulation of the internal flow within microscopic drops. The intimate connection with container flows nonetheless means that droplet-based micro-fluidic systems, irrespective of the specific configuration, share fundamental properties with the former as well as among each other. This is elaborated below for several flow-forcing techniques.

Internal flow induced by ambient flow Droplets immersed in a micro-channel flow driven by e.g. a pressure gra-

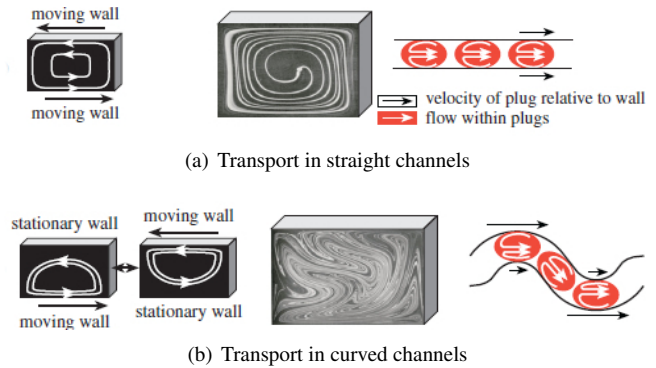


Fig. 34. Transport in propagating droplets (“plugs”) in micro-channel flow versus channel geometry: (a) straight channels yield non-chaotic transport due to equivalence with steady cavity flow; (b) curved channels admit chaotic transport due to equivalence with time-periodic cavity flow (adapted from [52]).

dient are subject to shear stresses at the fluid-fluid interface (and generically travel slightly faster than the bulk) [6]. This yields a non-zero surfacial velocity in said interface and thus induces an internal flow within the drop akin to lid-driven cavities (Fig. 34). Straight channels, by virtue of constant droplet shape and propagation speed, compare to steady wall forcing and thus yield a steady global circulation with typically non-chaotic dynamics (Fig. 34(a)). Curved channels with a spatially periodic geometry, on the other hand, give rise to oscillating droplet shape and speed and, analogous to time-periodic wall forcing, result in a time-periodic internal flow that admits chaotic dynamics (Fig. 34(b)) [164].

Practical implementation of the above working principle is found in a droplet travelling through a serpentine micro-channel according to Fig. 35(a) [164, 173]. Fig. 35(b) visualises the internal mixing pattern by the evolution of a binary concentration distribution in the droplet midplane using fluorescent lifetime imaging microscopy and reveals the characteristic stretching and folding of chaotic advection. The corresponding simulated evolution is shown in Fig. 35(c) and closely agrees with the experiments.

In-depth experimental analysis of 3D flow and transport within immersed (propagating) microscopic drops is highly challenging and largely beyond current experimental methods. Hence its exploration to date primarily involves theoretical and computational studies. Two standard cases underlying such studies are: (i) buoyant drops driven by gravity; (ii) non-buoyant drops driven by viscous stresses at the fluid-fluid interface. The non-dimensional 3D Stokes flow inside droplets of unit radius is in the co-moving reference frame, with z the direction of travel, described analytically by

$$u_x = zx, \quad u_y = zy, \quad u_z = 1 - 2z_*^2 + z^2, \quad (15)$$

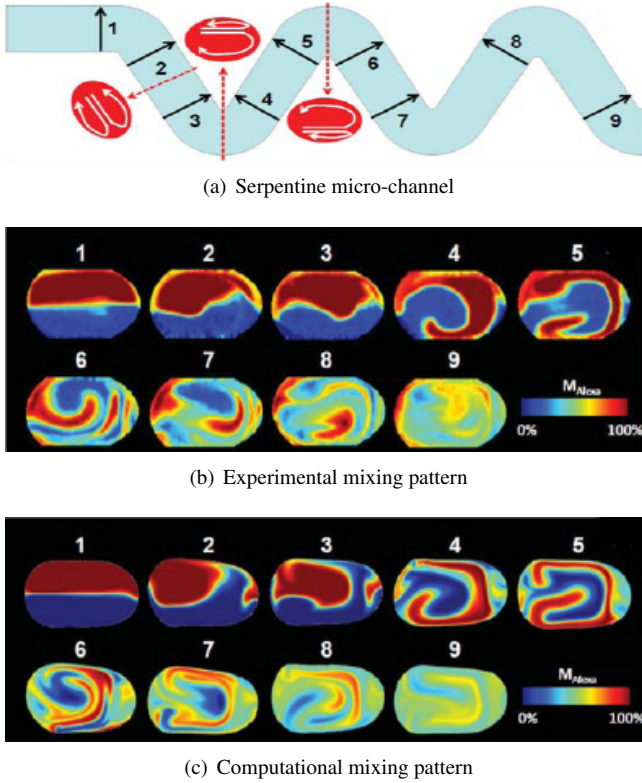


Fig. 35. Mixing inside propagation droplet immersed in serpentine micro-channel: (a) configuration; (b) experimental visualisation of mixing pattern by fluorescent imaging microscopy; (c) computational visualisation of mixing pattern (adapted from [173]).

and

$$\begin{aligned} u_x &= x(r_*^2 + 2z^2 - 1), \\ u_y &= y(r_*^2 + 2z^2 - 1), \\ u_z &= 2z(1 - 2r_*^2 + z^2), \end{aligned} \quad (16)$$

for former and latter case, respectively, with $r_*^2 = x^2 + y^2 + z^2$ [174].¹⁹ Fig. 36(a) gives the flow topologies for (15) (left) and (16) (right) comprising, by virtue of axis-symmetric flow ($u_\theta = 0$), of two and four “islands” of closed streamlines in planes of constant θ , respectively. (The black line indicates the z -axis and direction of travel.) However, these flow topologies – analogous to the cylinder flow in Fig. 23 – are singular limits in that *any* perturbation induces transition into (multiple families of) tori (Sec. 3.2.2). Disturbance of (15) and (16) by e.g. a weak swirl $\vec{u}' = \vec{\omega} \times \vec{x}$ (mimicking arbitrary imperfections), with $\vec{\omega} = (\omega_x, 0, \omega_z)$ following [174] and $\omega_x = \omega_z = 10^{-2}$, leads to the formation of one and two families of tori, respectively, centred on the axis of motion (Fig. 36(b)). Thus the perturbation exposes the “true” non-chaotic baseline of the flow topology in droplets,

¹⁹Flow (15) corresponds with Hill’s spherical vortex and is an analytical solution to both the Euler equations governing inviscid flow and the Stokes equations governing the flow inside a buoyant spherical droplet rising in a viscous fluid [175]. The latter, in turn, corresponds with the Hadamard-Rybczynski problem in the non-inertial limit $Re = 0$ [165].

which, by consisting of tori, is (dynamically) indeed equivalent to the above container flows. This overall implies similar Lagrangian dynamics and “routes to chaos”; the tori in Fig. 36(b) generically give way to a 3D steady topology of KAM tori and chaos as in e.g. Fig. 22 and Fig. 23 upon intensifying the perturbation of (15) and (16) [176, 174]. The specific behaviour may depend significantly on the relative strength of poloidal versus toroidal flow, though.

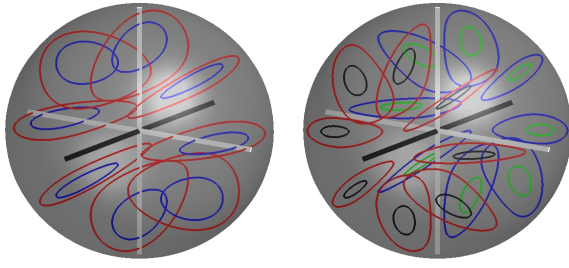
The study in [165] adopts base flows (15) and (16) to model 3D flow and Lagrangian transport within the travelling drop in the serpentine channel (Fig. 35). Flow (15) represents the straight channel (Fig. 34(a)) and, taking inevitable imperfections into account, yields a non-chaotic steady topology comprising of a single family of tori following Fig. 36(b) (left). The time-periodic flow in the curved channel (Fig. 34(b)) admits (in the presumed Stokes limit) construction from linear combinations of (15) and (16) and, by effectively switching continuously between the instantaneous base-flow topologies in Fig. 36(b), induces breakdown of tori and thus yields chaotic advection. Fig. 36(c) demonstrates this by the characteristic stretching-and-folding pattern emerging (for 3 typical situations) in the cross-section $x = 0$ of the 3D distribution of a tracer (white) initially occupying the lower droplet hemisphere [165].

Internal flow induced by electro-hydrodynamic forcing

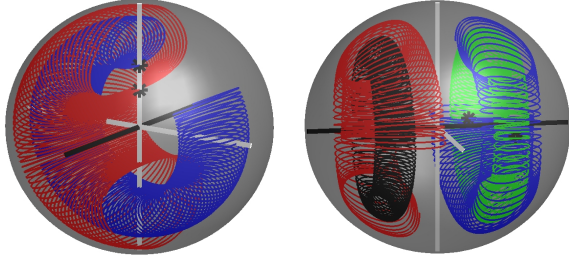
A configuration intimately related to the above serpentine channel exists in a translating droplet in a straight channel subject to an axial electric field $\vec{E} = E\vec{e}_z$. The latter, given the dielectric properties of droplet and bulk fluids are sufficiently apart, induces forces in the fluid-fluid interface that set up a so-called “Taylor circulation” [177]. Its topology corresponds (for a stationary droplet) with Fig. 36(b) (right), where the black axis coincides with the direction of travel, meaning that electro-hydrodynamic forcing has a comparable effect as shear due to curvature in the serpentine channel. Droplets travelling in the z -direction retain this topology yet develop a z -wise asymmetry: the leading/trailing family of tori expands/diminishes and, inherently, the separatrix – spanned by the grey axes in Fig. 36(b) (right) – shifts towards the trailing side of the droplet [177].

Chaotic advection by destruction of the tori arrangement following Fig. 36(b) (right) can be achieved basically in two ways: (i) unsteady field strength $E(t)$ so as to change the position of said separatrix in time; (ii) misalignment between electric field \vec{E} and translation direction so as to break the symmetries of the topology. The former is investigated for a falling droplet in a tank subject to a time-periodic electric field $\vec{E}(t) = E \sin(\omega t)\vec{e}_z$ in [178]. Fig. 37(a) visualises typical Lagrangian transport conditions by 2D temporal stroboscopic maps in the xz -plane of tracer particles according to simulations (top) and experiments (bottom). This reveals erratic wandering of tracers around surviving KAM tori (white patches in top panel) and thus signifies chaotic advection. The underlying mechanism intimately relates to RID (Sec. 3.3.2) and is elaborated below in the context of thermo-capillary forcing,

Chaos by misalignment is investigated in the



(a) Ideal topology buoyant (left) and non-buoyant (right) droplet.



(b) Real topology buoyant (left) and non-buoyant (right) droplet.



(c) Mixing pattern in serpentine-channel flow

Fig. 36. Buoyant gravity-driven and non-buoyant stress-driven drops as basic flow configurations: (a) 3D topologies for ideal conditions (black indicates z -axis and direction of travel; gray indicates (x, y) -axes); (b) 3D topologies for realistic conditions; (c) simulated mixing pattern in serpentine channel due to switching between buoyant and non-buoyant droplet flow. Panel (c) adapted from [165].

same configuration by imposing an electric field $\vec{E} = E(\cos\alpha\vec{e}_x + \sin\alpha\vec{e}_z)$ under an angle α with the translation direction [179]. This results in similar erratic wandering around KAM tori, as demonstrated by a typical 3D streamline in Fig. 37(b), again implying chaotic dynamics. Primary difference with the above is the fixed position of the separatrix, i.e. the imaginary plane in Fig. 37(b) between the vortical structures at the trailing (top) and leading (bottom) droplet side. The slight tilt emanates from the misaligned electric field ($\alpha \neq 0$).

Reorientation of the electric field enables similar accomplishment of chaos for a *stationary* droplet. This is demonstrated in [180] by a time-periodic reorientation of the above field via alternating angles $\alpha = 0$ and $\alpha = \alpha_w$.

Internal flow induced by thermo-capillary forcing

Thermo-capillary effects in droplets immersed in a bulk fluid and exposed to an axial temperature gradient

$$\vec{\nabla}T = (\kappa_0 + \kappa_1 z)\vec{e}_z, \quad (17)$$

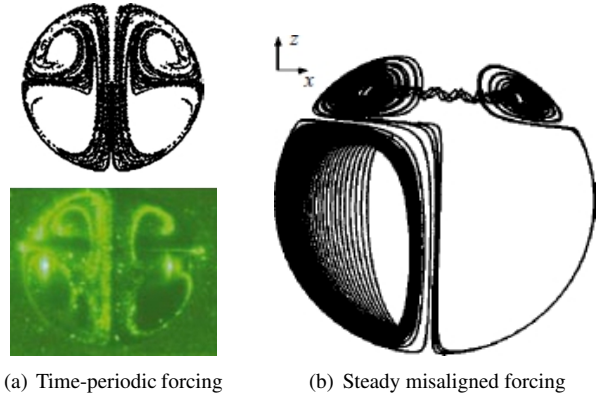


Fig. 37. Lagrangian transport in z -wise falling droplet subject to electro-hydrodynamic forcing: (a) stroboscopic map in xz -plane for time-periodic electric field along z -axis as simulated (top) and visualised by tracers (bottom) (adapted from [178]); (b) 3D streamline for steady electric field misaligned with z -axis (adapted from [179]).

with coefficients κ_0 and κ_1 parameterising its uniform and z -wise linear contributions, respectively, may induce forces in the fluid-fluid interface akin to the above electro-hydrodynamic phenomena and thus drive an internal circulation [181]. A uniform axial temperature gradient ($\kappa_0 > 0, \kappa_1 = 0$) causes droplet motion in $+z$ -direction and yields an internal circulation and corresponding topology following (15) and Fig. 36(b) (left), respectively. Chaotic advection again requires destruction of tori and can here be achieved by imposition of a non-uniform temperature gradient ($\kappa_0 > 0, \kappa_1 \neq 0$) and a perpendicular vortical motion due to shearing by the ambient flow. The non-uniform gradient yields an entirely intact topology following Fig. 36(b) (right) yet with the same z -wise asymmetry (and shift of the separatrix) as the above electro-hydrodynamic case; superposition of the shear initiates tori breakdown and results in chaotic streamlines wandering around surviving KAM tori in the same as shown in Fig. 37(b) [181, 182].²⁰

The onset of 3D chaotic advection in the present steady flow stems from defects that develop in both tori families near the separatrix for weak perturbation of the non-chaotic baseline [182]. This results in drifting and gradual chaotic dispersion reminiscent of RID in unsteady container flows (Fig. 27(a)) for all streamlines that encounter these defects. Essential difference with RID – and its steady counterpart [145] – is that defects here emanate from significant slowdown of Lagrangian motion near the separatrix instead of “true” resonance following (14). (Slow motion is a generalisation of resonance in that this affects the dynamics in a similar way; see Sec. 3.3.2 and Sec. 4.6.2.) The impact is therefore restricted to the “outer” tori close to the separatrix; the “inner” tori survive unscathed. Hence the dispersion thus induced is restricted to a chaotic region surrounding the latter tori. Stronger perturbation overrides these phenomena and results in the “conventional” breakdown of tori and (further) proliferation of the chaotic region (Sec. 4.6).

²⁰These flow conditions can be generated experimentally by e.g. differential heating via a traversing laser beam [181].

Dispersion due to local defects in LCSs of 3D steady flows has first been examined in [175] and denoted “trans-adiabatic drift”. Here significant slow-down of Lagrangian motion near certain isolated stagnation points caused this phenomenon. Analogous flow structures strongly suggest that basically the same mechanisms are at play in the above electro-hydrodynamically forced flow [179, 183]. Hence the chaotic dynamics in Fig. 37 are representative of the weakly-perturbed state for both electro-hydrodynamic and thermo-capillary forcing. Moreover, comparable baseline topologies implicate this mechanism also in the separatrix crossing in convection cells (Sec. 3.5.2).

Internal flow induced by electro-wetting In contrast to forcing in microfluidic networks, electro-wetting is a promising forcing technique for droplets in digital microfluidic platforms and relies on the dependence of the contact angle between droplet surface and substrate on the electric potential between former and latter. This enables actuation of an internal time-periodic flow through controlled oscillation of the droplet shape by variation of the contact angle via an AC voltage applied between an electrode at the droplet pole and the substrate [184, 185].

Fig. 38(a) visualises the 3D Lagrangian transport in a droplet flow driven by electro-wetting by temporal stroboscopic maps of tracer particles in a vertical cross-section through the axis (left) and a horizontal cross-section near the substrate (right) [185]. This reveals a global toroidal circulation about the vertical droplet axis, directed downwards in the centre and radially outward at the bottom, and implies a flow topology that is a perturbed state of a non-chaotic baseline following Fig. 36(b) (left). (The horizontal black axis in the latter coincides with the vertical droplet axis.) The corresponding transport is visualised in Fig. 38(b) by the evolution (from left to right) of fluorescent dye (green) and the symmetric counter-rotating “swirls” in the middle snapshot strongly suggest a topology that, similar to Fig. 18, contains sizeable KAM tori. Hence, contrary to the findings in [185], chaotic advection seems to occur only locally, namely in the surroundings of said tori. Moreover, dominant poloidal flow in conjunction with weak (fluctuating) toroidal flow closely resembles the situation in the champagne glass in Fig. 32 and thus suggests dynamics that, by considerations given before, may likely involve resonance phenomena.

Internal flow induced by acoustic streaming A relatively novel forcing technique for droplet flow in digital platforms employs 3D streaming induced by Rayleigh surface acoustic waves (SAWs) impinging on the surface [186]. Fig. 39 shows a typical internal streamline pattern driven by a SAW (red arrow), obtained by simulations (panel a) and experimental visualisation (panel b), and reveals two adjacent toroidal circulations about a common centre of rotation (red dashed curve). This implies (on grounds of symmetry) a baseline topology similar to Fig. 36(b) (right) consisting of two families of tori, where the horizontal black axis coincides with the red dashed curve in Fig. 39(a), suggesting behaviour comparable to the above flows driven by electro-hydrodynamic

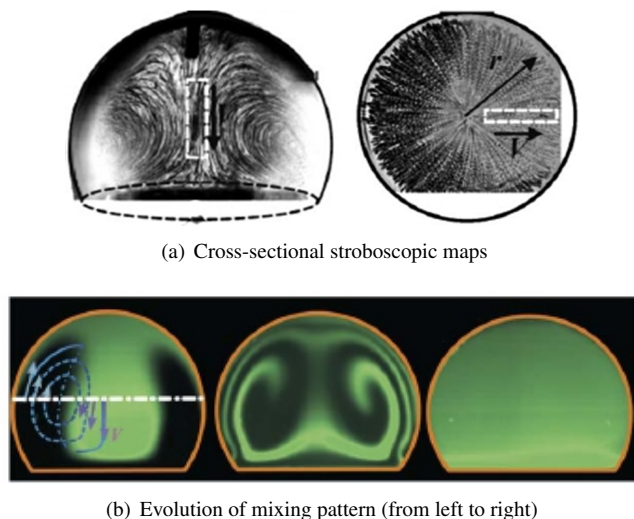


Fig. 38. Lagrangian transport in time-periodic droplet flow on substrate induced by electro-wetting: (a) stroboscopic map in vertical (left) and horizontal (right) cross-section visualised experimentally by tracers (arrows indicate flow direction); (b) evolving mixing pattern visualised by fluorescent dye. Adapted from [185].

and thermo-capillary forcing (Fig. 37). However, in contrast with the latter, the acoustic streaming exhibits a significant toroidal circulation (i.e. about the red dashed curve in Fig. 39), implying a 3D flow topology comparable to the steady inertial cylinder flow in Fig. 23: two symmetric families of KAM tori surrounded by chaos. Thus here chaos likely results from the conventional breakdown of tori associated with a predominantly toroidal motion instead of the resonance-induced scenario for the (mainly poloidal) flow driven by electro-hydrodynamic or thermo-capillary forcing.

Integrity of immersed drops Droplet-based microfluidic networks assume intact droplets and absence of transport between interior and ambient flow. However, droplets may exhibit leakage or even break-up due to e.g. excessive shear stresses and thus compromise the functionality of microfluidic devices [187, 188]. The fluid-fluid interface that bounds immersed droplets is a material surface and thus constitutes an LCS in its own right. Hence the Lagrangian dynamics of the interface is crucial to the integrity and stability of droplets. Consider to this end the response of a buoyant droplet following Fig. 36(b) to perturbation of the ambient flow by an unsteady strain investigated computationally in [189]. Fig. 40 shows the proliferation and interaction of the stable (red) and unstable (green) manifold of two so-called “distinguished hyperbolic trajectories” (DHTs) emerging from the disintegration of the (initially) spherical interface. DHTs and their manifolds are in essence the counterparts in aperiodic flows to hyperbolic periodic points and manifolds in time-periodic flows and thus dictate (chaotic) transport in basically the same way as illustrated in Fig. 5 (Sec. 4.6.1) [190]. Here these LCSs determine the intricate 3D detrainment and entrainment of droplet and ambient fluid, respectively, that ensues from the droplet instability.

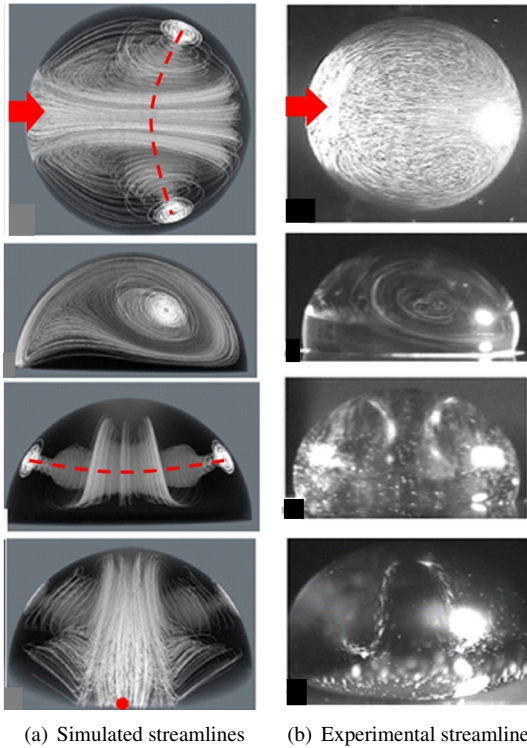


Fig. 39. Lagrangian transport in steady droplet flow on substrate induced by acoustic streaming: (a) simulated 3D streamline portrait (arrow indicates impingement of SAW; dashed curve indicates axis of primary circulation); (b) experimental visualisation of 3D streamline portrait by tracer particles. Adapted from [186].

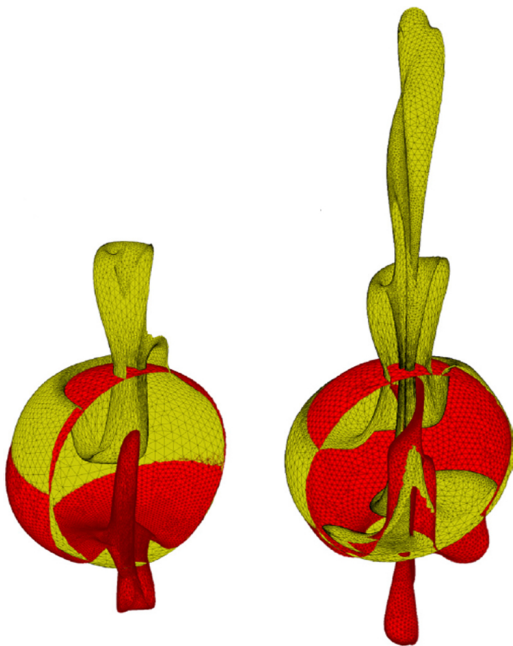


Fig. 40. Instability of immersed buoyant droplet due to perturbation of ambient flow by unsteady strain demonstrated by simulated proliferation (from left to right) and interaction of stable (red) and unstable (green) manifold of two DHTs (not shown) emerging from disintegration of (initially) spherical interface. Reproduced from [189].

3.4.3 Relevance beyond industry

Discussed below are instances of 3D Lagrangian (chaotic) transport in non-industrial flows that closely relate to flows in drops. The aim, as for duct (Sec. 3.2.3) and container (Sec. 3.3.3) flows, is again to expose similarities and analogies between (seemingly) different problems.

Cytoplasmic flow and transport Cytoplasmic flow and transport inside cells of living organisms is (regarding domain topology) the physiological analogy to the above drops. An important forcing mechanism is so-called “cytoplasmic streaming”, that is, internal circulation within cells by flow actuation at the cell boundary via “molecular motors” in a manner akin to shear-driven flow in droplets. Fig. 41(a) illustrates this for the cytoplasmic circulation inside a drosophila oocyte for the purpose of mixing of yolk granules as nourishment during cell development [191]. The corresponding cross-sectional circulatory velocity field in the (approximate) midplane obtained by 2DPIV is given in Fig. 41(b). Mixing is visualised in Fig. 41(c) by the motion and dispersion of yolk granules in the oocyte (indicated by dashed outline) tagged via a tracer injected at the yellow arrow (numbers indicate time instance in minutes). The tagged yolk initially migrates as a compact patch, subsequently moves away from the midplane and reappears in a well-mixed state. These observations in conjunction with the domain shape strongly suggest a baseline topology following Fig. 36(b) (right), where the grey axes span the separating midplane. The appreciable circulation in Fig. 41(b), in turn, suggests a flow resembling the droplet flow driven by acoustic streaming (Fig. 39). This, by analogy, implies a 3D flow topology comparable to the steady inertial cylinder flow in Fig. 23 and, inherently, chaos due to conventional tori breakdown.

A forcing mechanism employed specifically by motile cells is flow induced via deformation during migration in an ambient flow [34]. This suggests cytoplasmic flow and transport comparable to droplets propagating a serpentine channel (Fig. 35).

Delivery and mixing of drugs A further physiological counterpart of Lagrangian transport in drops is found in the delivery and mixing of drugs in the vitreous chamber of the eye (Fig. 42(a)). Intravitreal drug delivery namely is a common treatment for retinal diseases and advective transport by the internal flow induced through so-called “saccades” (rapid eye rotations during redirection of the visual axis) are considered key to this process. The study by [192] investigates the advection characteristics via reconstruction of the 3D time-periodic flow field in an *in vitro* physical model of the vitreous chamber from cross-sectional 2DPIV measurements. Lagrangian transport analyses by numerical particle tracking using the experimental velocity field reveal two toroidal circulations about the vertical axis and approximately symmetric about the midplane between upper and lower hemisphere. Fig. 42(b) gives typical trajectories in the upper hemisphere $z \geq 0$ (distinguished by colour) and demonstrates that said circulations consist of a predominantly poloidal circulation and a weak toroidal drift. This implies a baseline topology

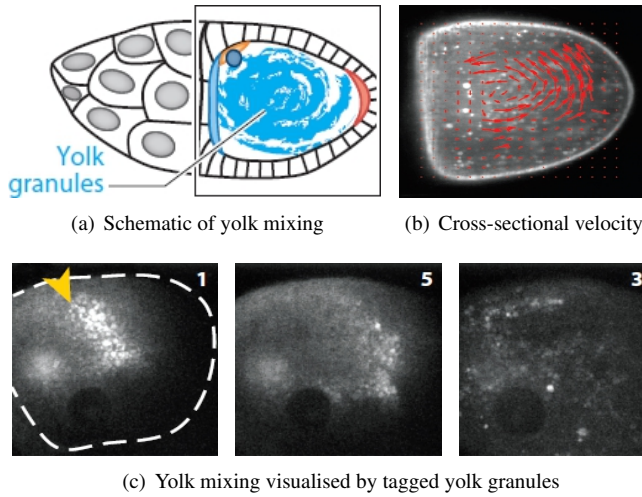


Fig. 41. Cytoplasmic flow and mixing in *Drosophila* oocyte driven by cytoplasmic streaming as physiological analogy to droplet flow: (a) yolk mixing by cytoplasmic streaming; (b) cross-sectional velocity (red vectors) visualised experimentally by 2DPIV; (c) yolk mixing visualised experimentally by motion and dispersion of yolk granules in oocyte (dashed outline) tagged by tracer injected at yellow arrow (numbers indicate time instance in minutes). Adapted from [191].

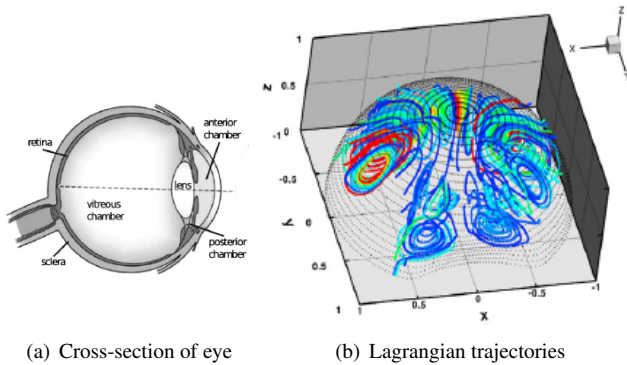


Fig. 42. Drug delivery in vitreous chamber of eye as physiological analogy to droplet flow: (a) cross-section of eye; (b) simulated Lagrangian trajectories in upper hemisphere (distinguished by colour) using experimental 3D time-periodic velocity field constructed from cross-sectional *in vitro* 2DPIV. Adapted from [192].

following Fig. 36(b) (right), where the grey axes span the xy -plane in Fig. 42(b). The prevailing poloidal motion suggests non-trivial Lagrangian dynamics due to separatrix crossing similar to the electro-hydrodynamic (and thermo-capillary) droplet flow in Fig. 37 and, given time-periodicity, likely also RID as in Fig. 27(a) (right).

3.5 Flow in webs

3.5.1 General configuration

A final class of systems relevant in the present scope concerns flows in a domain with an internal partitioning into interconnected elementary cells that admit exchange of fluid and scalars. This may involve a “soft” partitioning by a mesh

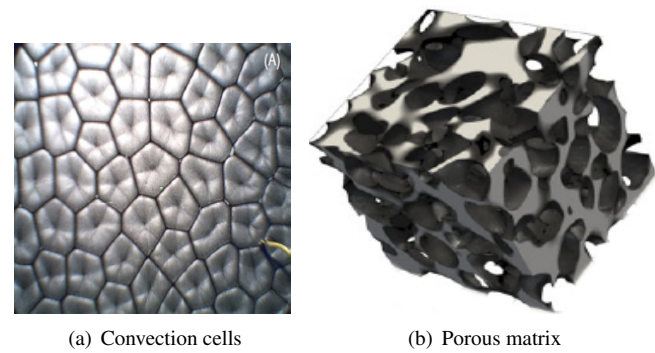


Fig. 43. Partitioning of flow domains into interconnected elementary cells: (a) “soft” partitioning in e.g. convection cells (reproduced from [193]); (b) “hard” partitioning by e.g. interconnected cavities in porous matrix (adapted from [194]).

of stream surfaces or material interfaces as e.g. in convection cells of buoyancy-driven flows (Fig. 43(a)) or a “hard” partitioning by a solid matrix enclosing interconnected cavities as e.g. in porous media (Fig. 43(b)). The Lagrangian transport by flows in such “webs” of interconnected cells exhibits, on grounds of the domain structure, characteristics of both periodic duct flows (transport *along* cells) and container flows (transport *within* cells). Hence flows in webs define in essence a hybrid class incorporating features of the systems considered in Sec. 3.2–Sec. 3.4.

3.5.2 Industrial and technological relevance

The examples of flows in webs shown in Fig. 43 in fact constitute two important configurations in the context of technological applications:

- *Convection cells* Lagrangian transport by laminar flow in convection cells is relevant to materials processing and fabrication involving coatings and films [195, 196, 197, 198, 199, 200, 201, 202] as well as for emerging technologies as liquid metal batteries [203, 204, 205].
- *Porous media* Lagrangian transport in porous media is key to both natural and engineered environments. The former primarily concerns subsurface flows involved in e.g. hydrology, enhanced oil and heat recovery and aquifer heat-storage systems [20, 21, 22, 23, 24, 25]. Transport in engineered porous media is at the heart of e.g. thermo-chemical heat-storage systems, microfluidic devices consisting of micro-vascular networks and compact heat exchangers based on metal foams [206, 207, 208, 209, 210].

The general flow and transport characteristics of both configurations are discussed and illustrated below using similarities and analogies with the above flow classes. Their manifestation and role in practical applications are subsequently exemplified by way of representative cases.

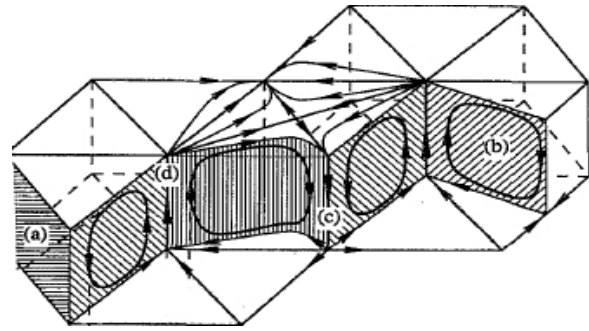
Convection cells: generic characteristics Fluid confined by a hot bottom wall and cold top wall tends to rise and descend near former and latter, respectively, due to buoyancy

and (upon overcoming viscous friction) thus sets up a pattern of circulations. This phenomenon is known as Rayleigh-Bénard convection and the vortical structures thus created, commonly denoted convection (or Bénard) cells, form regular patterns in the present regime of laminar flows [211]. Thin fluid films on a hot horizontal wall and with a free top surface behave essentially the same; here circulations emerge from an interplay of buoyancy and surface tension and result in Bénard-Marangoni convection. Both Rayleigh-Bénard and Bénard-Marangoni convection yield (under 3D laminar conditions) hexagonal patterns of convection cells as exposed in Fig. 43(a) by flow visualisation in the free surface of a silicon oil layer using aluminium tracer particles [193].

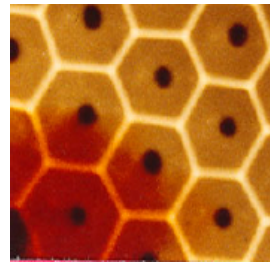
Fig. 44(a) schematically gives the 3D streamline pattern in two neighbouring hexagons consisting (within each cell) of closed streamlines within vertical cross-sections (surface “b” in right cell) centered around the hexagon axis (line “d” in left cell) [212]. Thus the flow topology is equivalent to that in the droplet in Fig. 36(a) (left), where the *horizontal* black axis corresponds with the *vertical* hexagon axis. However, such topologies, for reasons given before, are singular limits; the real cell-wise topology emerges for arbitrarily small perturbations and comprises of a family of tori centered on the (hexagon) axis similar to Fig. 36(b) (left).

Flow topologies consisting of complete tori admit inter-cellular transport across separatrices (e.g. plane “a” in Fig. 44(a)) only by diffusion. Fig. 44(b) experimentally visualises such diffusion-enabled global transport by the spreading of dye (red) in silicon oil across the “honeycomb” demarcated by the cell interfaces (bright pattern) [213]. The kinematic analogy with electro-hydrodynamic and thermo-capillary droplet flows (i.e. similar baseline topology and dominant poloidal circulation) strongly suggests that, upon weak perturbation, the tori in convection cells generically develop defects by the same resonance phenomena.²¹ This facilitates crossing of separatrices following Fig. 37 and thus enables *advective* inter-cellular transport as demonstrated in Fig. 44(c) by a typical simulated 3D trajectory of a tracer released at position P_7 in a weakly-perturbed flow [214].

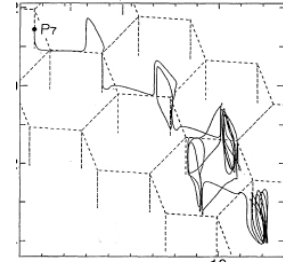
Experimental evidence of such resonance-induced inter-cellular transport is given in Fig. 44(d) by the dispersion of fluorescent tracer particles in an array of vortices set up in sulfuric acid by MHD forcing. (Each vortex corresponds with a hexagonal convection cell in Fig. 44(a) in top view.) Shown is the initial (top) and final (bottom) distribution of tracers released in one vortex (bright) in the unperturbed flow driven by steady MHD forcing (left) versus the perturbed flow by additional time-periodic forcing (right) [144]. This reveals a dramatic difference. Tracers in the unperturbed flow remain trapped in the original vortex; tracers in the perturbed flow, on the other hand, exhibit global dispersion due to the resonance-induced separatrix crossing. The essential role of time-periodicity in this process implies that here (in particular) resonance according to (13) – and thus RID fol-



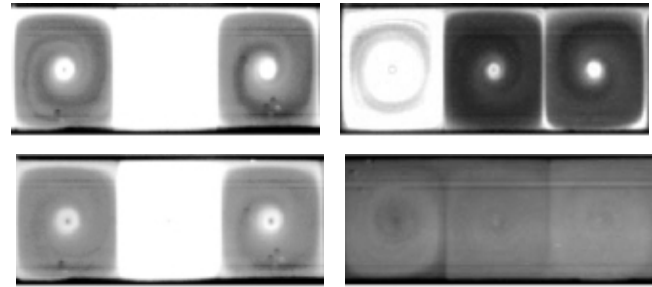
(a) 3D streamline pattern in two neighbouring hexagonal cells



(b) Global diffusive transport



(c) Global advective transport



(d) Restricted (left) versus global (right) advective transport

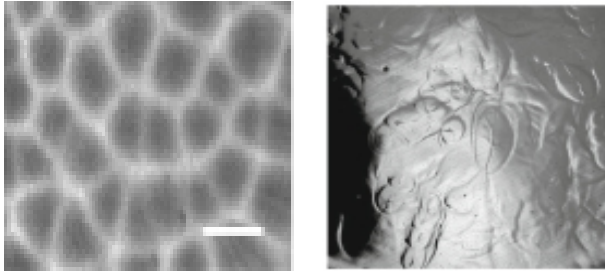
Fig. 44. Global 3D transport in network of convection cells: (a) 3D streamline pattern in neighbouring cells consisting (cell-wise) of closed streamlines within vertical cross-sections (surface “b” centered around the hexagon axis (line “d”) (adapted from [212]); (b) global diffusive transport visualised experimentally by dye spreading (red) across cell interfaces (bright pattern) (adapted from [213]); (c) global advective transport visualised by simulated 3D trajectory (starting at P_7) in perturbed flow (adapted from [214]); (d) restricted (left) versus global (right) advective transport in unperturbed and perturbed array of vortices, respectively, visualised experimentally by initial (top) and final (bottom) tracer distribution (adapted from [144]).

lowing Fig. 27(a) (right) – is the key player.

Convection cells: materials and fabrication technology

Important for the fabrication and application of coatings as paints or epoxy resins is homogeneous distribution of solvents and agents. Inhomogeneity of certain additives may result in the formation of convection cells due to Bénard-Marangoni convection (Fig. 43(a)) and, by the ensuing restriction of the advective transport of (other) additives to toroidal LCSs following Fig. 44(a), thus compromise the coating quality [195, 196, 197]. Typical surface defects arising from this are corrugated patterns, as visualised for a

²¹That is, due to “true” resonance by synchronised poloidal/rotational rotations following (13) and (14) and/or its generalisation, viz. significant local slow-down of Lagrangian motion (Sec. 3.3.2 and Sec. 4.6.2).



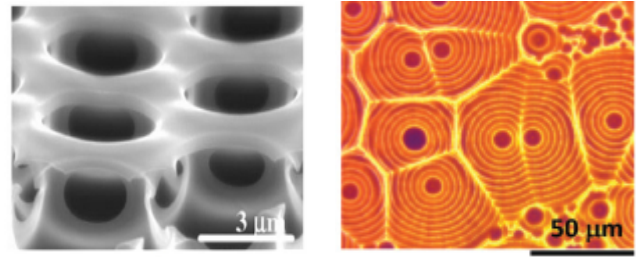
(a) drying polymer solution (b) drying paint films

Fig. 45. Surface defects in coatings and films due to Bénard-Marangoni convection cells: (a) corrugated pattern in polymer film on glass substrate visualised by shadowgraphy (bar represents 2.5 mm) (reproduced from [196]); (b) “orange peel” texture in paint on stainless steel ($23 \times 23 \text{ mm}^2$ area.) (reproduced from [197]).

drying polymer film on a glass substrate in Fig. 45(a) by shadowgraphy [196] and “orange peel” textures, as shown in Fig. 45(b) for a drying paint film on stainless steel [197]. Fundamental insights into 3D Lagrangian transport in convection cells may deepen the understanding of these adverse effects and offer ways to mitigate or eliminate them. The global advective transport across convection cells in Fig. 44(d) (right) is systematically induced by weak time-periodic perturbation of the flow using a frequency resonant with the typical circulation frequencies. This means that, given the particular nature of the perturbation is immaterial for small magnitudes, basically *any* perturbation during (industrial) fabrication and application of coatings – e.g. weak vibrations attuned to the natural frequencies – may promote global transport as in Fig. 44(d) (right) and thus counteract the convection cells.

Cell formation due to Bénard-Marangoni convection may, rather than being an undesired phenomenon, also find utilisation in materials technology for the fabrication of textured coatings and films [198, 199, 200, 201]. Certain micro-structured polymer films e.g. rely on the formation of so-called “breath figures” due to the condensation of moisture (contained in air) on cold solid or liquid surfaces. Running moist air over a polymer solution leads to the formation of water droplets on the liquid surface that (while sinking) congregate into hexagonal patterns due to their Lagrangian transport by the convection cells. The subsequent evaporation of solvent and water during solidification of the polymer solution leaves an imprint of the entrained water droplets as pores in the shape of the convection cells in the solid polymer matrix. Fig. 46(a) demonstrates this principle for the honeycomb porous micro-structure thus created in a thin polymer film on a glass substrate visualised by scanning electron imaging [200]. Lagrangian transport in the convection cells evidently is crucial to this fabrication technique and utilisation of fundamental insights – to e.g. actively manipulate droplet migration and congregation – may enable its further development.

An approach intimately related to the above has been proposed for the micro-structuring of photonic crystals,



(a) Micro-structured polymer film (b) Micro-structured solar cell

Fig. 46. Utilisation of Bénard-Marangoni convection cells for fabrication: (a) honeycomb porous micro-structure in polymer film visualised by scanning electron imaging (adapted from [200]); (b) micro-structured photonic crystals for solar cells in perovskite film visualised by microscopy (adapted from [202]).

which is key to the optical properties and, inherently, the performance of solar cells [202]. Here convection cells due to Bénard–Marangoni convection in a liquid perovskite film on a heated substrate determine the advective solvent transport during solidification and thus “assemble” micro-structures in the crystals as visualised in Fig. 46(b) by microscopy. The convection cells and, in consequence, the micro-structure admit manipulation by the substrate temperature and solution concentration. Further development of this process may also greatly benefit from exploitation of fundamental insights into 3D Lagrangian transport in convection cells.

Porous media: generic characteristics Porous media typically consist of a web of pores with random orientation and connectivity and throughflows, in consequence, spread transverse to the main flow direction. Fig. 47(a) demonstrates this by the xy -wise spreading of 3D streamlines in a steady z -wise throughflow in such a medium described by tracer particles (distinguished by colour) released on a line in a single pore at the inlet $z = 0$ [215, 216]. The global transverse particle dispersion is dictated by the 3D structure of the pore network and, given its random composition, converges on a Gaussian distribution with progressing stream-wise position z .

The local flow through consecutive pores undergoes repeated splitting and recombination similar as in partitioned duct flows (Sec. 3.2). A fundamental difference between these systems and porous media is that the random (instead of systematic) reorientation in the latter generically results in chaotic advection at the pore level [215]. This is demonstrated in Fig. 47(a) (inset) by the typical evolution of the transverse mixing pattern within pores (of circular cross-section) with stream-wise position z_n (starting from inlet $n = 1$), revealing the characteristic stretching and folding that signifies chaotic advection. Note the particular resemblance of the pore-scale mixing pattern with the patterns in the Quatro and serpentine mixers in Fig. 12(a) and Fig. 13(c), respectively, which also come about by splitting and recombination.

The LCSs associated with pore-scale chaotic advection in 3D steady flows are the manifolds emerging from stagna-

tion points $\vec{\tau} = \vec{0}$ of the skin-friction field

$$\vec{\tau} = \vec{n} \cdot \vec{\nabla} \vec{u} \Big|_{\Gamma} = \frac{\partial \vec{u}}{\partial n} \Big|_{\Gamma}, \quad (18)$$

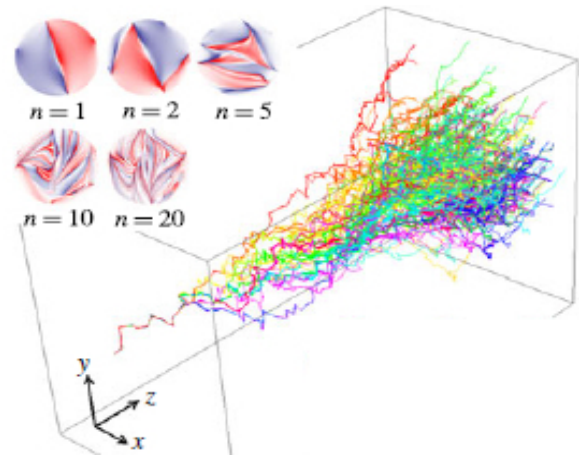
on the no-slip pore wall Γ with outward normal \vec{n} [215]. Fig. 47(b) gives typical 1D and 2D manifolds emanating from such points in a porous matrix consisting of disordered spheres (flow from right to left) [217]. These entities are the direct counterpart to manifolds of internal stagnation or periodic points shown in e.g. Fig. 26(b) and the 2D manifolds generically act as separatrices between e.g. circulation zones or the diverging streams of impinging jets [218]. Here the 2D manifolds of adjacent pores, ensuing from impingement and flow separation, interact transversally in a manner akin to the stable (blue) and unstable (red) manifolds in Fig. 5(a) and thus accomplish pore-scale chaotic advection.

Global *transverse* dispersion as in Fig. 47(a) originates from the random distribution of trajectories over pores comparable to the downstream distribution over multiple blood vessels in the aneurysm flow in Fig. 29(b) and depends primarily on the network geometry. Pore-scale chaos enhances transverse stretching of fluid elements and thus promotes their split-up during change-over between consecutive pores, but its effect on global transverse dispersion, though not yet conclusively established, seems marginal [217].

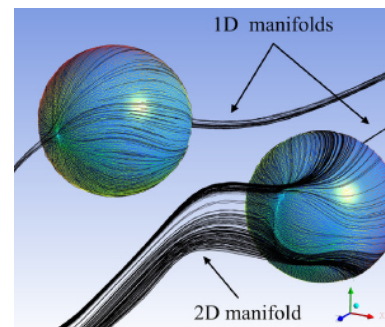
Global *stream-wise* dispersion, on the other hand, is significantly affected by pore-scale chaos. It causes streamlines to “sample” the entire pore cross-section and the full pore-scale velocity distribution, meaning that particles effectively migrate downstream by the cross-wise *averaged* velocity, as opposed to the *local* velocity in the Poiseuille-like throughflows in 2D steady systems. This chaos-induced averaging of the particle velocity tends to homogenise the pore-wise residence time and thus retards stream-wise particle dispersion – diminishing stream-wise “diffusion” of the global particle concentration – relative to 2D porous media devoid of pore-scale chaos [216, 217].²²

The above findings are relevant to randomly-structured porous media yet equally non-trivial Lagrangian transport is anticipated for 3D steady throughflows in case of structure imparted by a natural heterogeneity (as e.g. anisotropy in fractured media) or engineered by design. This reinforces the link with periodic duct flows (which rely on *structural* re-orientation) and thus likely yields pore-scale flow topologies where, similar to Fig. 7(a), chaotic regions coexist with LCSs as separatrices or stream tubes. Such intricate topologies are expected to cause fundamental departures of the global transport in 3D porous media from their 2D counterparts in a comparable way as before. However, essentially 3D pore-scale Lagrangian transport and its upscaling to global transport (as well as the interplay with diffusion) remain largely open problems [217, 194]. This concerns in particular the proper

²² The same chaos-induced averaging occurs in periodic duct flows and, besides homogenisation of particle velocities, furthermore promotes stream-wise throughflow of *all* particles, or equivalently, suppresses particle entrapment in e.g. localised recirculation zones [86].



(a) Global and pore-scale transport



(b) Manifolds of skin-friction field

Fig. 47. Transport in random porous media: (a) *global* transverse spreading of *z*-wise throughflow visualised by simulated streamlines (distinguished by colour) starting in single pore at inlet and corresponding *pore-scale* chaotic advection (inset) visualised by simulated mixing pattern; (b) manifolds emanating from stagnation points in skin-friction field on pore walls. Adapted from [217]

upscaling of microscopic pore-scale behaviour to the mesoscopic level of “representative elementary volumes” (REVs). REVs are the smallest elementary volumes in a macroscopic system admitting averaged representations of flow and transport over both the fluid domain and porous matrix [219]. Such averaged representations make complex problems computationally tractable and thus are of great importance for practical analyses. This is elaborated below.

Natural porous media: subsurface transport Natural porous layers in the subsurface typically possess a random structure and the above findings on both 3D pore-scale and 3D global transport demonstrated in Fig. 47(a) have important ramifications for practical situations. Consider for example the contamination of soil and groundwater via the spreading of a methane plume due to leakage during enhanced oil recovery. Fig. 48 shows a typical instantaneous 3D methane gas plume (via a concentration iso-surface) visualised by ground-penetrating radar in a field experiment in an actual aquifer following controlled injection at the indicated “shallow” and “deep” positions and spreading by the groundwater (“GW”) flow [220]. The analogy with the configuration

in Fig. 47(a) strongly suggests similar 3D transport characteristics: pore-scale chaotic advection and, in consequence, suppressed downstream diffusion of the global plume front.

Crucial for large-scale practical problems such as the plume spreading in Fig. 48 are tractable (computational) models for the global flow and transport. Full prediction and simulation of pore-scale behaviour namely is (i) physically impossible due to a lack of detailed microscopic information and, even if available, (ii) prohibitively expensive. The concept of REV for description of mesoscopic flow and transport introduced before is a common approach towards such macroscopic models [219]. (The entire sample in Fig. 43(a) constitutes an REV typical of sands or bead packs.) The standard Darcy model is a well-known REV-based macroscopic model and assumes that the REV-averaged volumetric flux density \vec{q} [m/s] (commonly denoted as the “Darcy velocity”) is proportional to the driving pressure gradient following

$$\vec{q} = -\frac{\kappa}{\mu} \nabla p, \quad (19)$$

with κ and μ the permeability and fluid viscosity, respectively, at the mesoscopic REV scale [219]. The average pore-scale velocity \vec{v} is given by the Darcy-Forchheimer relation $\vec{v} = \vec{q}/\phi$, with $0 < \phi < 1$ the porosity, and e.g. corresponds with the mean stream-wise (“GW”) plume flow in Fig. 48.

The transverse and stream-wise spreading (of e.g. the plume in Fig. 48) by the dispersion of particles in the porous matrix is in conventional (Darcy-type) REV models incorporated via Fickian diffusion. This expands the governing equations for the particle motion to an advection-diffusion equation of the form (1), with C representing the particle “concentration” [219]. However, such upscaling from pore-scale to REV-scale transport does not account for phenomena as pore-scale chaos and its impact on global dispersion thus likely produces incorrect predictions of e.g. the plume spreading in Fig. 48, which may have significant practical consequences. Hence development of faithful REV models that adequately incorporate non-trivial 3D pore-scale transport is absolutely critical for reliable analyses of practical problems in complex porous media [217, 194].

Subsurface REV models, besides mere analysis and prediction of transport in large-scale systems, furthermore enable utilisation of Lagrangian concepts for enhanced subsurface transport. This has great potential for a range of applications including enhanced geothermal systems [20, 21], *in situ* recovery of minerals or oil [22, 23] and groundwater remediation [24, 25]. LCSs associated with the average pore-scale velocity $\vec{v} = \vec{q}/\phi$, with \vec{q} according to (19), determine the global subsurface transport characteristics and admit manipulation by the pumping schemes for the injection and extraction wells that must be used in such applications to drive the subsurface flow. Thus purposeful conditions can (in principle) be systematically accomplished: global chaotic advection for efficient distribution of e.g. leaching solutions for minerals extraction or creation of large-scale islands as *in situ* processing zones for groundwater remediation. First exploratory studies on 2D reservoirs serve as

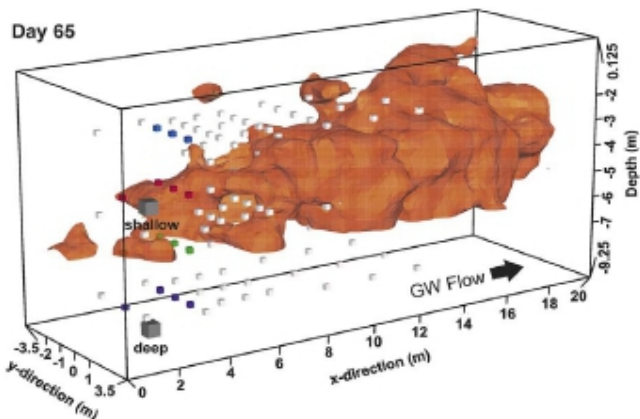


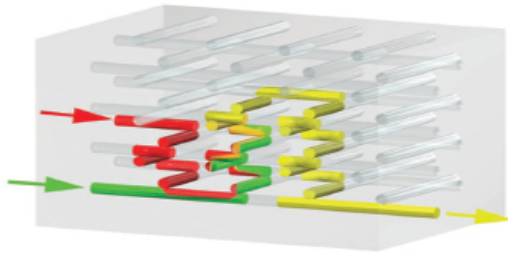
Fig. 48. Transport in natural porous media illustrated by subsurface spreading of methane plume through groundwater flow (“GW”) visualised (via instantaneous concentration iso-surface) by ground-penetrating radar in field experiment following controlled injection at “shallow” and “deep” positions. Adapted from [220].

promising “proof of principle” of this Lagrangian approach and may pave the way to new technologies for subsurface flow engineering [221, 222, 223, 224, 225, 226, 227].

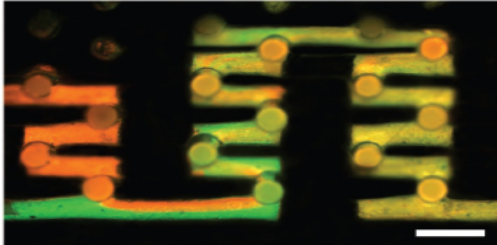
Engineered porous media: transport enhancement Engineering porous media with a given structure enables systematic manipulation of the (pore-scale) flow and transport and e.g. finds application in engineered 3D micro-vascular networks for mixing purposes. These configurations in essence expand on inline partitioned-duct mixers (Sec. 3.2.2) by progressive splitting and recombination of multiple fluid streams in a network of interconnected ducts to achieve “pore-scale” chaos akin to that in random porous media (Fig. 47(a)). Fig. 49(a) schematically demonstrates this by the interaction between two incoming fluid streams (red and green) and their mixing into a homogeneous outgoing fluid stream (yellow) during progression through a micro-vascular network fabricated of cylindrical duct segments [207]. Fig. 49(b) gives an experimental visualisation of the actual process using fluorescent dye.

The above example concerns a duct connectivity such that two incoming streams combine into one outgoing stream as per Fig. 49(a); this renders each such connection within the porous matrix analogous to the T-shaped micro-mixer in Fig. 14 yet with a more complicated duct geometry. However, the same duct architecture admits more elaborate connectivity tailored to attain different transport characteristics as e.g. simultaneous “pore-scale” chaos and global transverse distribution as in Fig. 47(a) or a certain heterogeneity in global dispersion properties.

Engineered porous media may furthermore aim at enhancing scalar transfer *between* flow and porous matrix. An important application exists in compact heat exchangers for heating/cooling of fluid flows based on metal foams (Fig. 50(a)) [208, 209, 210]. The metal foam realises the favourable attributes of a heat exchanger in a small volume: high interfacial area between solid and fluid; high ther-



(a) Mixing of incoming fluid streams



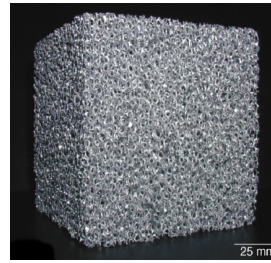
(b) Experimental visualisation (top view)

Fig. 49. Transport in engineered porous media illustrated by mixing in engineered 3D micro-vascular network: (a) mixing of incoming fluid streams (red/green) into homogeneous outgoing fluid stream (yellow); (b) experimental visualisation by fluorescent dye (bar represents $500\ \mu\text{m}$). Adapted from [207].

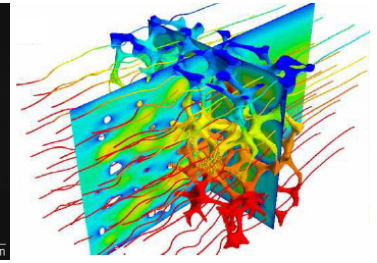
mal conductivity in the solid; complex flow geometry promoting mixing and, in consequence, enhancing convective heat transfer. Fig. 50(b) demonstrates a typical situation by the simulated cooling of a hot fluid flow entering (from the left) a metal foam with an imposed cold top side and adiabatic bottom [209]. This reveals an essentially 3D flow and temperature field and thus implies a non-trivial interplay of heat transfer by 3D pore-scale (chaotic) advection and diffusion in both fluid and solid. Foam-based heat exchangers generically involve dense structures comparable to Fig. 50(a), necessitating, similar to the above subsurface systems, REV representations for modelling and analysis of practical devices. However, 3D pore-scale transport phenomena as demonstrated in Fig. 50(b) are, for reasons given before, typically beyond conventional REV models, meaning that proper upscaling is again crucial for reliable description of the global transport characteristics.

3.5.3 Relevance beyond industry

Plate tectonics Convection cells set up in the mantle of the Earth (consisting of viscous molten rock) by its hot inner core are a major driving mechanism behind plate tectonics in the lithosphere (i.e. the outer crust) [228,35]. The associated up- and downwellings by hot and cold thermal plumes, respectively, namely cause the formation of ridges and trenches (via so-called “subduction”) due to viscous friction exerted on the crust in a way as illustrated in Fig. 51(a) and thus contribute to shaping the topography of the Earth’s surface. This configuration is analogous to Bénard-Marangoni convection in a liquid film by concerning a fluid layer inside a 3D spherical shell as in Fig. 27(a) (left) that is heated from below by



(a) Fe-Cr-Al-Y metal foam



(b) Cooling of hot fluid

Fig. 50. Transport in engineered porous media illustrated by compact heat exchanger based on metal foam: (a) typical metal foam (Fe-Cr-Al-Y alloy) for heat-transfer purposes (reproduced from [210]); (b) simulated cooling of hot fluid flow entering (from the left) metal foam with cold top/adiabatic bottom visualised by temperature of foam surface and streamlines (blue/red: min/max) and velocity magnitude (blue/red: zero/max) in planar cross-sections (adapted from [209]).

the hot inner sphere and subject to lithosphere-induced surface stresses at the outer sphere. Hence the system tends to form a pattern of convection cells akin to Fig. 45 with corresponding up- and downwellings due to thermal plumes centred on lines “d” and “c”, respectively, in Fig. 44(a). However, different (material) compositions of oceanic versus continental lithospheres and complex mantle rheologies significantly complicate this process, resulting in highly irregular patterns of up- and downwellings as illustrated in Fig. 51(b) by level sets of “low” (blue) and “high” (yellow) temperatures, respectively [229]. This irregularity suggests comparably disordered surficial patterns (i.e. in the lithosphere) tending to that of drying paint in Fig. 45(b).

The computational study by [230], modeling mantle and lithosphere as a single continuum with an appropriate rheology, reveals that crust deformation is essential to the single-sided subduction (i.e. one tectonic plate sliding below another as in Fig. 51(a)) that in reality occurs at downwellings. Fig. 51(c) demonstrates this process by a cross-section of the temperature field, representing (via its strong correlation with the viscosity) the material composition, where low (blue) and high (red) temperature corresponds with crust and mantle, respectively. This reveals the downward intrusion of a high-viscosity “plume” of crust material (blue) into the mantle (red) at the contact line (position 1) of two converging plates driven by the convective circulation. The corresponding velocity (black arrows) exposes a localised circulation zone to the left of the intruding plume, meaning that the latter primarily consists of material stemming from the right plate, signifying its single-sided subduction below the left plate.

Entrainment and transport of crust material into the mantle is central to the subduction and is, by its essentially Lagrangian nature, determined by the 3D flow topology. This, by analogy with convection cells, implies a scenario as before: breakdown of separatrices as plane “a” in Fig. 44(a) in response to some perturbation and onset of dynamics as e.g. global dispersion according to Fig. 44(c). Shown behaviour strongly suggests that here the non-trivial rheology renders these separatrices unstable and thus induces the de-

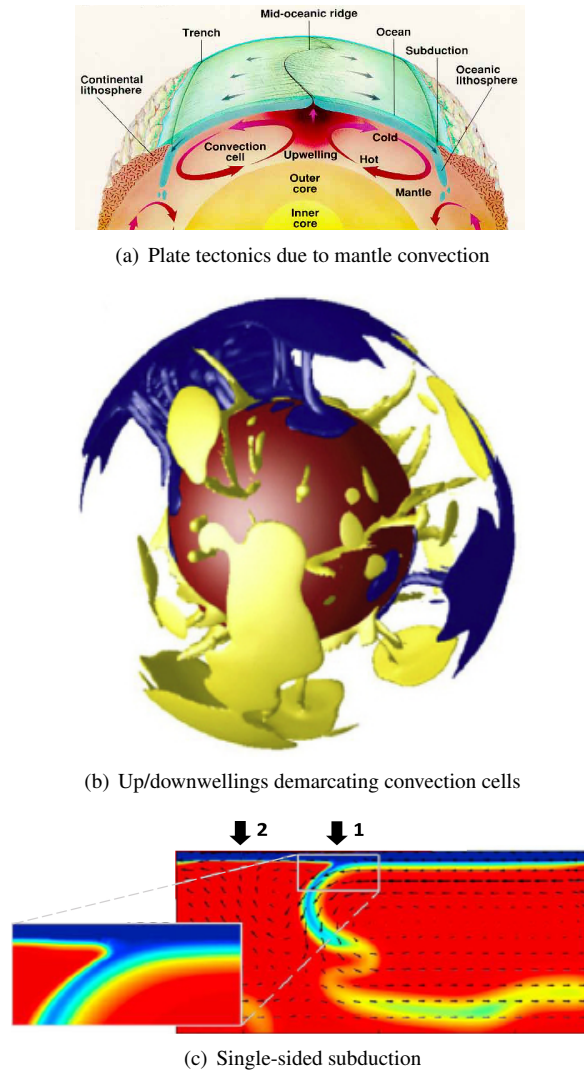


Fig. 51. Plate tectonics induced by mantle convection as geophysical instance of convection cells: (a) mechanism (reproduced from [228]); (b) up- and downwellings demarcating convection cells visualised by “low” (blue) and “high” (yellow) simulated temperatures (adapted from [229]); (c) single-sided subduction demonstrated by intrusion of low-temperature (blue) crust material into high-temperature (red) mantle at position 1 and resulting circulation zone between positions 1 and 2 (adapted from [230]).

velopment of an asymmetric flow field and topology. The local circulation zone in Fig. 51(c) implies, besides the contact line at position 1, a further stagnation point near position 2 and, given the clock-wise flow, interaction of the unstable and stable manifolds associated with former and latter, respectively. These considerations implicate LCSs emerging from the lithosphere at such stagnation points/lines in the subduction, which in 3D likely yields (local) chaotic advection. Dedicated Lagrangian analyses enable further exploration of these phenomena.

Micro-circulation in living tissue Exchange of oxygen, carbon dioxide and nutrients with living tissue occurs via so-called “micro-circulation” through a local network of mi-

croscopic blood vessels [32]. Each organ has its own dedicated micro-circulation; e.g. lung alveoli (Sec. 3.3.3) are covered by pulmonary capillaries for oxygen transfer into the blood stream. Fig. 52(a) illustrates the complexity of micro-vascular networks by that of the somatosensory cortex in the brain of a rat visualised by 3D imaging using X-ray tomographic microscopy [231]. The tissue and embedded network effectively constitutes a random porous medium, implying, by analogy with such media, generic transport characteristics as demonstrated in Fig. 47(a): chaotic advection locally within the vessels and, in consequence, relatively weak global stream-wise dispersion.

Important in a physiological context is the impact of local disruptions or malformations of the vascular network on the global transport by the micro-circulation. The computational study by [231] investigates the effect of a vascular occlusion (i.e. blockage) of the blood vessel at the arrow in Fig. 52(a) by reduction of its diameter by a factor 1,000 using a model based on graph representations of the micro-vasculature. Blue and red vessels in Fig. 52(a) have a significantly lower and higher flow rate, respectively, compared to the unobstructed situation (green vessels are unaffected) and, by emerging throughout the entire network, expose a substantial impact of the occlusion on the 3D global throughflow (from bottom to top). This is likely to cause departures from the transport properties of healthy networks. Typical vessel-wise residence times, irrespective of the nature of the local transport, directly correlate with flow rates. Moreover, local transport depends, similar to periodic duct flows (Sec. 3.2), strongly on the flow rate. Hence, though probably retaining its chaotic nature due to the random connectivity, quantitative changes may nonetheless alter the residence-time distributions of affected blood vessels. The occlusion thus is expected to considerably affect the 3D global (stream-wise) dispersion properties. Insights into both local and global impact of occlusions on 3D transport are crucial for deeper understanding of the physiology of strokes, since reduced or disrupted cerebral oxygen delivery is a major cause for this brain condition [232].

Occlusions, by altering the flow rate, are malformations in the micro-vascular network that affect the (local) *permeability* (i.e. parameter κ in (19)). Malformations in the tissue itself mainly alter another key mesoscopic transport property, namely the (local) *porosity* ϕ . Notorious examples are cancerous tumors that, due to their rapid growth, typically have underdeveloped vascular networks and thus effectively reduce ϕ . Hence tumors rely strongly on diffusion of oxygen from surrounding healthy tissue and, given this is a relatively slow process, tend to become hypoxic, which attributes to their malignant behaviour [233]. Fig. 52(b) demonstrates this for the simulated 3D oxygen transport in a realistic vascular network (red) containing several tumors (green) using the computational model by [234, 235]. The lower-right inset shows the local oxygen distribution in the grey cross-section and reveals a one-to-one correspondence between the oxygen-poor (blue) and oxygen-rich (yellow) regions and the tumor and healthy tissue, respectively.

Micro-vascular networks, unlike subsurface porous re-

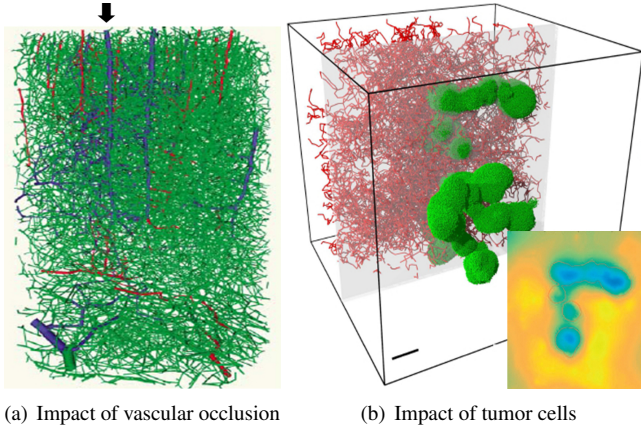


Fig. 52. Micro-circulation in living tissue as physiological instance of transport in porous networks: (a) impact of vascular occlusion (arrow) on global throughflow (from bottom) in somatosensory cortex in rat brain visualised by simulated flow rate (red/blue: relatively larger/lower flow rate; green: unaffected region) (adapted from [231]); (b) impact of tumor cells (green) on oxygen distribution via vascular network (red) visualised by simulated oxygen levels (yellow/blue: healthy/hypoxic) in grey cross section (inset) (adapted from [234]).

gions (Sec. 3.5.2), admit full characterisation to ever greater detail via medical imaging techniques, which paves the way to dedicated (REV-like) computational models incorporating the specific structure as demonstrated in Fig. 52. This has great potential for computer-aided diagnosis and treatment based on numerical simulation of flow and transport in the patient-specific micro-vasculature and surrounding tissue [236, 237, 238]. Such computational medical tools may thus enable identification of regions affected by occlusions, prediction of the progression of hypoxic tumors or development of strategies for optimal drug delivery for chemotherapy. The results shown in Fig. 52 are obtained with the model by [234] that in fact incorporates the specific vascular structure. However, it relies on a simplified diffusion-only transport model that represents the oxygen supply via the blood stream as line sources of oxygen at the vessel locations; advective and Lagrangian transport associated with this stream is omitted. Hence, besides network structure and tissue composition, incorporation of the relevant (Lagrangian) transport phenomena in both modelling and data interpretation is equally important.

4 Unified Lagrangian framework for 3D transport

The discussion in this section seeks to reconcile the above flow categorisation with theoretical/fundamental concepts and methods so as to (i) outline a unified framework for systematic 3D Lagrangian transport analyses of practical flows and (ii) provide a “gateway” to further literature on this subject matter. To this end the essentials of Lagrangian transport are treated in a tutorial-like approach via *capita selecta* and exemplified with the systems highlighted in Sec. 3.

4.1 Critical points as organising entities

Key organising entities of the Lagrangian flow topology are so-called “critical points” associated with the Lagrangian motion described by kinematic equation (2). Critical points “shape” the flow topology by geometrically and topologically governing the proliferation of fluid trajectories. These entities are common (or even inherent) in confined geometries both in the flow interior and on no-slip (internal) walls and thus are of great relevance to practical flows. The emergence and nature of critical points is elaborated below for 2D and 3D flows under steady and time-periodic conditions.

4.1.1 Critical points in 2D flows

Critical points in *steady* flows $\vec{u} = \vec{u}(\vec{x})$ correspond with stagnation points, that is, positions \vec{x}_0 at which the fluid motion vanishes:

$$u(\vec{x}_0) = 0 \quad \Rightarrow \quad \vec{x}(t) = \vec{\Phi}_t(\vec{x}_0) = \vec{x}_0. \quad (20)$$

The flow topology near stagnation points \vec{x}_0 is determined by the linearisation $G(t)$ of flow $\vec{\Phi}_t$, i.e.

$$\vec{x}'(t) = G(t)\vec{x}'_0, \quad G(t) = e^{At}, \quad A = \left. \frac{\partial \vec{u}}{\partial \vec{x}} \right|_{\vec{x}_0}, \quad (21)$$

with $\vec{x}' = \vec{x} - \vec{x}_0$ the local position vector and A the strain-rate tensor. The linearised flow in spectral representation reads

$$G(t) = \sum_{i=1}^2 e^{\lambda_i t} \vec{v}_i, \quad \lambda_{1,2} = \frac{J_1 \pm \sqrt{J_1^2 - 4J_2}}{2}, \quad (22)$$

with (λ_i, \vec{v}_i) the eigenvalue-eigenvector pairs of A and

$$J_1 = \vec{\nabla} \cdot \vec{u} \Big|_{\vec{x}_0}, \quad J_2 = \left. \frac{\partial u_x}{\partial x} \frac{\partial u_y}{\partial y} \right|_{\vec{x}_0} - \left. \frac{\partial u_x}{\partial y} \frac{\partial u_y}{\partial x} \right|_{\vec{x}_0}, \quad (23)$$

the invariants of its characteristic equation $\lambda^2 - J_1 \lambda + J_2 = 0$. Solenoidality through $J_1 = \text{tr}(A) = \sum_i \lambda_i = 0$ yields $\lambda_1 = -\lambda_2 = \sqrt{-J_2}$ and thus implies two kinds of stagnation points depending on the sign of $J_2 = \det(A)$. Case $J_2 > 0$ gives a complex-conjugate pair of eigenvalues $(i\lambda, -i\lambda)$, with $i = \sqrt{-1}$ and $\lambda = \sqrt{J_2}$, and the local Lagrangian motion (21) in polar coordinates becomes

$$r'(t) = r'_0, \quad \theta'(t) = \theta'_0 + \lambda t, \quad (24)$$

describing concentric circular streamlines around \vec{x}_0 following Fig. 53(a) (left). Case $J_2 < 0$ gives a pair of real eigenvalues $(\lambda, -\lambda)$, with $\lambda = \sqrt{|J_2|} > 0$, resulting in

$$\vec{x}'(t) = \sum_{i=1}^2 \eta_i(t) \vec{v}_i, \quad \eta_i(t) = \eta_i(0) e^{\lambda_i t}, \quad (25)$$

as local Lagrangian motion, with $\vec{\eta} = (\eta_1, \eta_2)$ the canonical coordinates associated with the principal strain axes (\vec{v}_1, \vec{v}_2) , describing hyperbolic streamlines following Fig. 53(a) (right). Stagnation points “shape” the flow topology by imparting the topology of the linearised flow on their vicinity (i.e. the surrounding region devoid of other stagnation points). The step-wise steady flows in Fig. 3 in fact contain only a single stagnation point of the former kind ($J_2 > 0$) and the global streamline portrait, in consequence, is topologically equivalent to Fig. 53(a) (left).

Critical points in *time-periodic* flows correspond with periodic points (6) and are direct counterparts of stagnation points (20). Local linearisation of mapping (5) namely gives

$$\vec{x}'_p = F^p \vec{x}'_0, \quad F = \left. \frac{\partial \vec{\Phi}_T}{\partial \vec{x}} \right|_{\vec{x}_0}, \quad (26)$$

yielding an identical (spectral) structure as (22) and (23) upon substitution $\vec{u} \rightarrow \vec{\Phi}_T$ and $e^{\lambda_i t} \rightarrow \lambda_i$, with (λ_i, \vec{v}_i) here the eigenvalue-eigenvector pairs of deformation tensor F . Solenoidality through $J_2 = \det(F) = \prod_i \lambda_i = 1$ yields

$$\lambda_1 = 1/\lambda_2 = J_1/2 + \sqrt{(J_1/2)^2 - 1}, \quad (27)$$

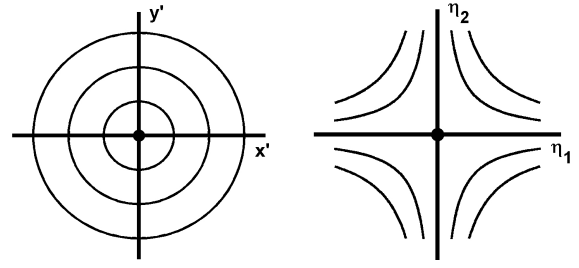
and again implies two kinds of points yet here depending on $J_1 = \text{tr}(F)$ due to the different emergence of the eigenvalues in the spectral structure. Case $|J_1| < 2$ gives a complex-conjugate pair of eigenvalues (λ, λ^*) , with $\lambda = J_1/2 + i\sqrt{1 - (J_1/2)^2}$ and $\lambda^* = 1/\lambda$; case $|J_1| > 2$ gives a pair of real eigenvalues $(\lambda, 1/\lambda)$, with $\lambda = \lambda_1 > 1$. This results for former and latter case in

$$(r'_p, \theta'_p) = (r'_0, \theta'_0 + p\phi), \quad \vec{x}'_p = \sum_{i=1}^2 \eta_i \lambda_i^p \vec{v}_i, \quad (28)$$

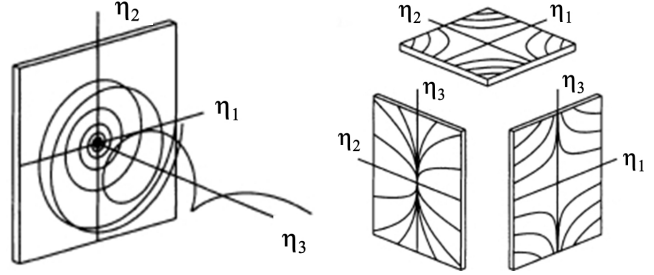
respectively, with $\phi = \arg(\lambda) = \arctan(\sqrt{(2/J_1)^2 - 1})$, revealing local Lagrangian motion identical to that near the stagnation points following (24) and (25). (Note $|\lambda| = 1$ for complex λ .) Hence the periodic points for $|J_1| < 2$ and $|J_1| > 2$ are indeed *direct* counterparts to the above stagnation points for $J_2 > 0$ and $J_2 < 0$, respectively [131].

Stagnation/periodic points for complex-conjugate and real eigenvalue pairs are denoted *elliptic* and *hyperbolic* points, respectively, based on the structure of the local flow topology (Fig. 53).²³ Elliptic and hyperbolic points create LCSs that are topologically equivalent to Fig. 53(a) (left) and Fig. 53(a) (right), respectively. Thus elliptic points constitute centres of the islands in e.g. Fig. 3(a) and Fig. 5(a); principal axes \vec{v}_1 and \vec{v}_2 of hyperbolic points are the origin of unstable and stable manifolds, respectively, as shown e.g. in Fig. 5(a).

²³Elliptic and hyperbolic stagnation points are in literature commonly denoted “center” and “saddle”, respectively [239]. The current nomenclature is adopted to underscore the essential similarity with periodic points.



(a) Elliptic (left) and hyperbolic (right) point in 2D flows



(b) Hyperbolic focus (left) and hyperbolic node (right) in 3D flows

Fig. 53. Flow topology near critical points \vec{x}_0 in the local reference frame $\vec{x}' = \vec{x} - \vec{x}_0$ with hyperbolic points represented in the associated canonical reference frame (η_1, η_2) and (η_1, η_2, η_3) in 2D and 3D flows, respectively. Panel (b) adapted from [136].

The above reveals that elliptic and hyperbolic points are the only critical points possible in 2D solenoidal flows. This has the fundamental implication that the corresponding flow topologies are *always* composed of arrangements of LCSs corresponding with these points. Hence flow topologies with islands embedded in chaotic regions demarcated by manifolds following Fig. 5(a) are characteristic for generic 2D time-periodic flows. However, important to note is that hyperbolic points and manifolds, though typically present, do not imply chaos *per se*; decisive for chaotic advection is the particular behaviour of the manifolds (Sec. 4.6.1).

4.1.2 Critical points in 3D flows

Stagnation points and associated flow topologies are in 3D steady flows also determined by the spectral properties of strain-rate tensor A following (21), which are governed by the characteristic equation $\lambda^3 - J_1 \lambda^2 + J_2 \lambda - J_3 = 0$, with invariants $J_1 = \text{tr}(A)$, $J_2 = (\text{tr}^2(A) - \text{tr}(A^2))/2$ and $J_3 = \det(A)$. Solenoidality again yields $J_1 = 0$ and real A implies (at least) one real eigenvalue (say λ_3). Hence the dynamics in the η_3 -direction (spanned by eigenvector \vec{v}_3) is always described by

$$\eta_3(t) = \eta_3(0) e^{\lambda_3 t}, \quad (29)$$

meaning that stagnation points differ solely by the behaviour in the (η_1, η_2) -plane. Two kinds can again be distinguished.

Case $J_3 > \lambda_3^3/4$ yields (besides real λ_3) a complex-conjugate pair of eigenvalues $(\lambda_R + i\lambda_I, \lambda_R - i\lambda_I)$, with

$$\lambda_R = -\lambda_3/2, \quad \lambda_I = \sqrt{J_3/\lambda_3 - (\lambda_3/2)^2}, \quad (30)$$

resulting in local Lagrangian motion (21) in the (η_1, η_2) -plane (in polar coordinates) according to

$$r'(t) = r_0' e^{\lambda_R t}, \quad \theta'(t) = \theta_0' + \lambda_I t, \quad (31)$$

describing spiralling streamlines about the η_3 -axis following Fig. 53(b) (left). This kind of stagnation point is denoted *hyperbolic focus* and is a 3D generalisation of the elliptic points of 2D flows. Principal difference with the latter is the (generically) non-constant radius – and ensuing spiralling motion – due to $\lambda_R = -\lambda_3/2 \neq 0$. Two situations may occur: (i) distancing from the (η_1, η_1) -plane while contracting around the η_3 -axis for $\lambda_3 > 0$; (ii) approaching the (η_1, η_2) -plane while diverging from the η_3 -axis for $\lambda_3 < 0$. Said plane and axis define the 2D unstable (stable) and 1D stable (unstable) manifolds, respectively, in the former (latter) case. The infinitesimal plane spanned by principal axes $\vec{v}_{1,2}$ is the origin of the 2D manifold in physical space; principal axis \vec{v}_3 is the origin of the corresponding 1D manifold.

Case $J_3 < \lambda_3^3/4$ gives (besides real λ_3) real eigenvalues

$$\lambda_{1,2} = -\lambda_3/2 \pm \sqrt{(\lambda_3/2)^2 - J_3/\lambda_3}, \quad (32)$$

and (upon properly redefining the canonical frame) can always be chosen such that λ_1 and $\lambda_{2,3}$ are of opposite sign. Thus Lagrangian motion in both the (η_1, η_2) and (η_1, η_3) -planes is essentially similar to the hyperbolic points of 2D flows according to (25) and yields 3D dynamics following Fig. 53(b) (right). Hence the present kind of stagnation point is a generalisation of said points and denoted *hyperbolic node* hereafter.²⁴ Here the (η_2, η_3) -plane and η_1 -axis define the 2D unstable (stable) and 1D stable (unstable) manifolds, respectively, for $\lambda_1 < 0$ ($\lambda_1 > 0$). The steady lid-driven cylinder flow for $Re > 0$ in Fig. 23(b) and Fig. 23(c) e.g. accommodates a hyperbolic focus (not shown) at the intersection of the toroidal axis of the tori and the symmetry plane $y = 0$. Said axis and plane in fact define the corresponding 1D and 2D manifolds, respectively.

The direct analogy between stagnation and periodic points is retained for 3D flows [136]. The local behaviour near periodic points remains dependent on the deformation tensor F following (26) that, upon the substitution adopted before, again assumes the same spectral structure as A . Solenoidal flow gives $J_3 = \det(F) = 1$ and real F implies (at least) one real eigenvalue (say λ_3) and, in consequence, η_3 -wise dynamics similar to (29): $\eta_{3,p} = \eta_{3,0} \lambda_3^p$. Hence the kind of periodic points in 3D flows is also determined by the behaviour in the (η_1, η_1) -plane. Case $J < 2/\sqrt{\lambda_3}$ and $J > 2/\sqrt{\lambda_3}$, where $J = \lambda_1 + \lambda_2 = J_1 - \lambda_3$, define the counter-

parts to (30) and (32), respectively, with here

$$\lambda_R = J/2, \quad \lambda_I = \sqrt{1/\lambda_3 - (J/2)^2}. \quad (33)$$

as real and imaginary parts of the complex eigenvalue and

$$\lambda_{1,2} = J/2 \pm \sqrt{(J/2)^2 - 1/\lambda_3}, \quad (34)$$

as real eigenvalues. The local Lagrangian motion in the (η_1, η_2) -plane is a generalisation of (28) and becomes

$$(r'_p, \theta'_p) = (|\lambda|^p r'_0, \theta'_0 + p\phi), \quad \vec{x}'_p = \sum_{i=1}^2 \eta_i \lambda_i^p \vec{v}_i, \quad (35)$$

with $\phi = \arctan(\sqrt{(2/J)^2/\lambda_3 - 1})$ and $|\lambda| = 1/\sqrt{\lambda_3}$. (Principal difference with 2D flows is that generically $|\lambda| \neq 1$ and $\lambda_1 \lambda_2 = 1/\lambda_3 \neq 1$.) Thus cases $J < 2/\sqrt{\lambda_3}$ and $J > 2/\sqrt{\lambda_3}$ result in dynamics according to Fig. 53(b) (left) and Fig. 53(b) (right), respectively, and indeed are entirely equivalent to the above stagnation points. Hence former and latter are also denoted *hyperbolic focus* and *hyperbolic node*. The isolated periodic point in the time-periodic cylinder flow in Fig. 26(b) (not shown) e.g. is a hyperbolic focus. The highly-convoluted 2D and 1D manifolds emanate from the (η_1, η_2) -plane and η_3 -axis, respectively, of the local canonical frame in Fig. 53(b) (left) and demonstrate the global complexity that these entities may assume. However, key for the nature of the Lagrangian dynamics, that is, chaotic versus non-chaotic, is – in steady and time-periodic 3D flows – again the particular behaviour of these manifolds (Sec. 4.6.1).

Critical points of the skin friction field $\vec{\tau}$ of 3D steady flows following (18) have a flow topology that corresponds with the hyperbolic focus and emerge in a “saddle” and “node” configuration if the canonical (η_1, η_2) -plane and (η_2, η_3) -plane, respectively, in Fig. 53(b) (right) coincides with the wall [215, 217]. (The fact that generically $\vec{\nabla} \cdot \vec{\tau} \neq 0$ is immaterial here.) The associated 1D and 2D manifold give rise to a *streamline* and *stream surface* extending from the wall into the domain in the node and saddle configurations, respectively, in a way as demonstrated in Fig. 47(b).

4.1.3 Critical lines in 3D flows

Stagnation points may merge into continuous curves and thus form so-called “stagnation lines” that, by definition, are characterised by absence of motion – and, inherently, deformation – in the tangent direction \vec{e}_t . This implies $G\vec{e}_t = \vec{e}_t$ for the linearised flow (21) and thus renders the tangent an eigenvector of the strain-rate tensor A , say $\vec{v}_3 = \vec{e}_t$, with corresponding eigenvalue $\lambda_3 = 0$. Tensor A becomes singular for $\lambda_3 = 0$ (i.e. $J_3 = 0$) and invalidates expressions (30) and (32) for the remaining eigenvalues $\lambda_{1,2}$ due to an undefined fraction J_3/λ_3 . Alternative relations are found via the simplified characteristic equation in the singular state, i.e.

²⁴The nomenclature of [136] is adopted as uniform terminology for stagnation and periodic points. The classification for (instantaneous) 3D streamline patterns by [240] refers to the hyperbolic focus as “focus” and the hyperbolic node as “node-saddle-saddle” due to the saddle-like and node-like dynamics in the (η_1, η_2) , (η_1, η_3) -planes and (η_2, η_3) -plane, respectively.

$\lambda(\lambda^2 - J_1\lambda + J_2) = 0$, that through $J_1 = 0$ yields $\lambda_{1,2} = \sqrt{-J_2}$ and thus gives the same form as for stagnation points in 2D steady flows. Hence the dynamics in the canonical (η_1, η_2) -plane transverse to each point on the stagnation line is either elliptic ($J_2 > 0$) or hyperbolic ($J_2 < 0$) according to Fig. 53(a) (left) and Fig. 53(a) (right), respectively. This has the fundamental implication that stagnation lines in 3D flows signify (locally) essentially 2D dynamics. The common centre (dots) of the global family of closed streamlines in the Stokes limit ($Re = 0$) of the steady cylinder flow in Fig. 23(a) e.g. is a stagnation line consisting entirely of elliptic points.

Periodic points may in a similar way merge into so-called “periodic lines” and are the counterpart to stagnation lines in 3D time-periodic flows. Here absence of motion in tangent direction \vec{e}_t implies $F\vec{e}_t = \vec{e}_t$ for the linearised stroboscopic map (26) and thus gives an eigenvalue-eigenvector pair $(\lambda_3, \vec{v}_3) = (1, \vec{e}_t)$. Relations (33) and (34) for $\lambda_3 = 1$ collapse on relation (27) for $|J| < 2$ and $|J| > 2$, respectively, and consequentially identify with the spectral signatures for elliptic and hyperbolic points in 2D time-periodic flows. The dynamics transverse to periodic lines is, entirely analogous with stagnation lines, therefore also essentially 2D.

The periodic line in the time-periodic cylinder flow in Fig. 27(b) e.g. is partitioned into segments of elliptic (normal) and hyperbolic (heavy) points, yielding local transverse dynamics following Fig. 53(a) (left) and Fig. 53(a) (right), respectively. The quasi-2D chaos in the time-periodic cylinder flow driven by alternating x -wise translation of top and bottom walls in Fig. 26(a) (centre) e.g. emanates from multiple periodic lines arranged transverse to the moving walls and consisting entirely of elliptic or hyperbolic points (not shown) [136]. The “holes” in the chaotic layer outline tubes formed by merger of islands of the constituent periodic points of the elliptic lines. Both the stable and unstable manifolds of the hyperbolic lines (in time-periodic as well as steady flows) are 2D surfaces that, similarly, result from merger of the manifold pairs of its individual points.

4.1.4 Closed trajectories in 3D flows

An important generalisation of critical points and lines exists in closed streamlines in 3D steady flows and closed trajectories in stroboscopic maps of 3D time-periodic flows.

Closed streamlines in 3D steady flows are described by fluid parcels that return to their initial position after a finite cycle time τ , i.e. $\vec{\Phi}_\tau(\vec{x}_0) = \vec{x}_0$, meaning that the parcel position $\vec{x}(t)$ is a periodic solution of kinematic equation (2): $\vec{x}(t) = \vec{x}(t + \tau)$. The local dynamics near a fluid parcel with momentary position $\vec{x}_0(t)$ is governed by a linearised flow of the form (21) in the co-moving reference frame $\vec{x}'(t) = \vec{x}(t) - \vec{x}_0(t)$. The periodic nature of the strain-rate tensor, i.e. $A(t + \tau) = A(t)$, admits a linear coordinate transformation $\vec{y}(t) = P(t)\vec{x}'(t)$, with periodic transformation matrix $P(t) = P(t + \tau)$, such that the linearised kinematic

equation (2) near $\vec{x}_0(t)$ becomes time-independent, i.e.

$$\frac{d\vec{x}'}{dt} = A(t)\vec{x}'(t) \quad \Rightarrow \quad \frac{d\vec{y}}{dt} = B\vec{y}(t), \quad (36)$$

with B the constant strain-rate tensor in the \vec{y} -frame [241]. The equivalence with the flow (21) near stagnation points readily yields $\vec{y}(t) = e^{Bt}\vec{y}_0$ and, in turn, leads to

$$\vec{x}'(t) = G(t)\vec{x}'_0, \quad G(t) = P(t)e^{Bt}P^{-1}(t), \quad (37)$$

as linearised flow in the co-moving physical frame. Note that flow G generically is non-periodic: $G(t) \neq G(t + \tau)$.

Relation (37) exposes the flow near a closed streamline as a local similarity transform of the steady flow in the \vec{y} -frame, meaning that the dynamics is determined by the spectral properties of B , which has important ramifications. Material line elements of the streamline return to their initial position after time τ , implying $G(\tau)\vec{e}_t(\tau) = \vec{e}_t(\tau) = \vec{e}_t(0)$, with $\vec{e}_t(t) = \vec{e}_t(t + \tau)$ again the tangent, resulting in an eigenvalue-eigenvector pair $(\lambda_3, \vec{v}_3) = (0, P^{-1}(\tau)\vec{e}_t(\tau))$ for B . This situation is identical to that for stagnation lines and thus gives

$$\lambda_{1,2} = \sqrt{-J_2(B)}, \quad (38)$$

for the eigenvalues in the direction transverse to the closed streamline, rendering also here the behaviour essentially 2D. Moreover, given B characterises the entire closed streamline, the dynamics is qualitatively the same everywhere (i.e. the behaviour remains either fully elliptic or hyperbolic during the excursion of a fluid parcel).

Closed streamlines are key LCSs in many of the practical steady flows considered in Sec. 3. The tori in the impeller-driven flow in Fig. 18(b) are centred on elliptic closed streamlines and the surrounding chaotic sea emanates from accompanying hyperbolic closed streamlines. The inherent 2D nature of the transverse dynamics established above explains the qualitative resemblance of the cross-sectional topology in Fig. 18(c) and Fig. 18(d) with 2D time-periodic systems (Fig. 5(a)). The tori and chaotic regions in e.g. the rotating-lid and translating-lid cylinder flows in Fig. 22 and Fig. 23, respectively, the ACEO-driven flow in Fig. 24 as well as the baseline topologies of microdroplets in Fig. 36(b) correspond in a similar way with elliptic/hyperbolic streamlines.

Streamlines reconnecting via the periodic inlet-outlet of steady duct flows (denoted “periodic streamlines” hereafter) must always exist in these systems and thus are crucial to the Lagrangian transport properties of e.g. industrial inline mixers [86]. These LCSs namely invariably result in a flow topology as demonstrated for the RAM in Fig. 7(a): stream-wise tori centered on elliptic streamlines embedded in chaotic regions “driven” by hyperbolic streamlines. Former and latter emerge as elliptic and hyperbolic periodic points, respectively, in the cross-sectional topology

in Fig. 7(b). The magnetic flux surfaces in MHD representations of tokamak fusion reactors in Fig. 17 are, by analogy with periodic duct flows (Sec. 3.2.3), centered on elliptic magnetic field lines. The “o-points” and “x-points” in Fig. 17(b) are poloidal intersections of elliptic and hyperbolic field lines. The invariable emergence of closed (magnetic) streamlines in these systems also here explains their essentially 2D (chaotic) dynamics.

Closed trajectories in 3D time-periodic flows correspond with stroboscopic maps (4) of individual fluid parcels that densely fill closed loops over infinitely many periods. To this end the associated mapping (5) must be *aperiodic*, that is, the individual parcel positions in (4) remain distinct at all times. Such closed trajectories e.g. sit at the centre of the tori in the rheology-induced time-periodic cylinder flow in Fig. 25(a) and the time-periodic annular flow in Fig. 27(a).

Closed trajectories thus described are, irrespective of the progression of fluid parcels along discrete positions, smooth and continuous closed curves reminiscent of a closed streamline. Continuity then suggests an equally smooth and continuous topology in their direct proximity that, in consequence, may be considered equivalent to the streamline portrait of a fictitious steady solenoidal “flow” $\vec{v} = \vec{v}(\vec{x})$. Fluid parcels are in this representation mapped along streamlines of \vec{v} governed by kinematic equation $d\vec{x}/ds = \vec{v}$, with s a fictitious time, and the closed trajectory – analogous to “true” closed streamlines – is its periodic solution $\vec{x}(s) = \vec{x}(s + \tau)$.

Fictitious time s acts as a spatial coordinate along the streamlines of \vec{v} and thus admits expression of the positions \vec{x}_p of a fluid parcel on the closed trajectory in terms of a corresponding s_p . This, via (37), readily yields

$$\vec{x}'_p = F_p \vec{x}'_0, \quad F_p = P(s_p) e^{B s_p} P^{-1}(s_p), \quad (39)$$

as local mapping in the co-moving reference frame and, by analogy, implies the same behaviour as near closed streamlines: essentially 2D dynamics governed by eigenvalue pair (38) of either fully elliptic or fully hyperbolic nature.

The extent of the tori in the beforementioned rheology-induced time-periodic cylinder flow in Fig. 25(a) demonstrates that the essentially 2D behaviour associated with closed trajectories may impact a sizeable region. However, the 2D dynamics imparted by these entities can also be very localised, as exemplified by the defective tori – signifying 3D dynamics – in the time-periodic annular flow in Fig. 27(a) due to RID. Similar restriction of the 2D dynamics of closed trajectories by resonance-induced tori breakdown is suspected in e.g. time-periodic droplet flows driven by electro-wetting in Fig. 38 and the time-periodic flow in the vitreous chamber of the eye (Fig. 42). The basic mechanisms of RID are elaborated in Sec. 4.6.2.

4.1.5 Symmetries as organising mechanisms

Symmetries play a critical role in the structure of the flow topology and, inherently, the Lagrangian dynamics of

3D (un)steady flows [43]. Insight into this role is important especially for industrial flows, since manufactured devices and engineered flows often have symmetries due to the geometry and/or the repetitive nature of the process such as the systematic flow reorientation in periodic duct flows (Sec. 3.2.2).

Discrete geometrical and dynamical symmetries in particular are key organising mechanisms for critical points/lines and closed trajectories as well as their associated LCSs. An important class exists in reflectional symmetries S (i.e. mirroring positions or LCSs about some symmetry plane \mathcal{P}) and two important instances can be distinguished within the present scope: *ordinary* and *time-reversal* reflectional symmetries. Former and latter are for both flow $\vec{\Phi}_t$ and mapping $\vec{\Phi}_T$ following (2) and (5) given by

$$\vec{\Phi} = S\vec{\Phi}S, \quad \vec{\Phi} = S\vec{\Phi}^{-1}S, \quad (40)$$

respectively, and relate the (reversed) dynamics on either side of the symmetry plane \mathcal{P} . Fig. 54(a) illustrates this for the time-reversal reflectional symmetry about plane $x = 0$ (i.e. $S_x : (x, y) \rightarrow (-x, y)$): the trajectory in the forward flow starting from \vec{x} is the mirror image of that in the reversed flow starting from $S(\vec{x})$ about $x = 0$.

Both ordinary and time-reversal reflectional symmetries following (40) imply emergence of LCSs \mathcal{L} as either entities symmetric about S , i.e. $S(\mathcal{L}) = \mathcal{L}$ or as symmetric pairs $\{\mathcal{L}, S(\mathcal{L})\}$. Time-reversal reflectional symmetries furthermore imply stagnation lines (steady flow) and periodic lines (time-periodic flow) in symmetry plane \mathcal{P} [136, 124]. The steady cylinder flow for $Re = 0$ in Fig. 23(a) e.g. has an ordinary reflectional symmetry $S_y : (x, y, z) \rightarrow (x, -y, z)$ and time-reversal reflectional symmetry $S_x : (x, y, z) \rightarrow (-x, y, z)$ about plane $y = 0$ and plane $x = 0$, respectively, resulting in the (elliptic) stagnation line in the former and symmetric streamline pairs about the latter plane. Symmetry S_y is preserved under inertial conditions ($Re > 0$) and thus dictates a symmetric arrangement of tori and chaotic trajectories in Fig. 23(b) and Fig. 23(c) about plane $y = 0$ (mirror images not shown). The periodic line in plane $y = -x$ of the time-periodic cylinder flow in Fig. 27(b) (right) in a similar way emanates from a time-reversal reflectional symmetry $S_{xy} : (x, y, z) \rightarrow (-y, -x, z)$ [124]. Symmetries may also manifest themselves locally. The time-reversal reflectional symmetry $S_\alpha : (r, \theta, z) \rightarrow (r, \alpha - \theta, z)$ of the base flow \vec{v} of the 2.5D RAM flow about the centerline $\alpha/2$ ($= \pi/8$) of the first aperture results in a reflectional symmetry $S_\gamma : (r, \theta) \rightarrow (r, \alpha - \Theta - \theta)$ about axis $\theta = (\alpha - \Theta)/2$ ($= -3\pi/40$) in the cross-section (Fig. 7(b)) of the 3D flow topology in Fig. 7(b) [83].

Time-reversal reflectional symmetries furthermore imply that streamlines (within a confined flow domain) crossing the symmetry plane \mathcal{P} must cross twice and form closed streamlines [122, 126]. Thus symmetry S_x of the non-inertial steady cylinder flow gives rise to a continuous family of closed streamlines centered on said stagnation line (of which one specimen is shown in Fig. 23(a)). Conversely, breaking of such a symmetry (if existent) is necessary for non-trivial

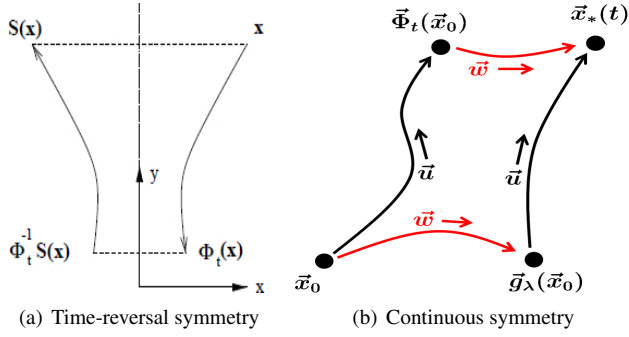


Fig. 54. Symmetries in the Lagrangian dynamics: (a) discrete time-reversal reflectional symmetry $S : (x, y, z) \rightarrow (-x, y, z)$ about plane $x = 0$ (reproduced from [131]); (b) continuous symmetry \vec{w} commuting with flow \vec{u} according to $\vec{x}_*(t) = \vec{g}_\lambda(\vec{\Phi}_t(\vec{x}_0)) = \vec{\Phi}_t(\vec{g}_\lambda(\vec{x}_0))$.

(chaotic) dynamics; the emergence of tori embedded in chaos in Fig. 23(b) and Fig. 23(c) is e.g. a direct consequence of the breakdown of S_x by fluid inertia.

The above global organisation of the flow topology generalises to stroboscopic maps with a time-reversal reflectional symmetry. Islands emerge either as symmetric pairs or as symmetric entities about \mathcal{P} as demonstrated in Fig. 5(a) for the time-periodic 2D lid-driven flow, which has a time-reversal reflectional symmetry about the horizontal centerline (not shown). The chaotic sea is subject to the same organisation in that the stable and unstable manifolds of hyperbolic points/lines within \mathcal{P} form symmetric pairs about this plane. Thus the stable (blue) and unstable (red) manifolds in Fig. 5(a) are mirror images about said centerline. The 2D manifolds associated with the hyperbolic segments of the periodic line in Fig. 27(b) (right) in a similar way are mirror images about the symmetry plane of S_{xy} .

LCSs as islands/tori and manifolds are robust and therefore satisfy the global symmetry. Individual trajectories within chaotic seas, on the other hand, are generically *asymmetric* due to their extreme sensitivity to initial conditions. The slightest asymmetry in the initial positions of the forward/reversed flows in Fig. 54(a), i.e. \vec{x} versus $S(\vec{x}) + \vec{e}$, with $|\vec{e}| \ll 1$, eventually always leads to symmetry breaking.

Symmetries other than reflections may play important roles as well. An ordinary *non-reflectional* symmetry e.g. relates the tube segments on the elliptic segments of the (perturbed) periodic line in Fig. 27(b) (right) and in fact dictates their merger with an inner/outer shell to form one LCS via RIM [139, 147]. Moreover, *continuous* symmetries according to Fig. 54(b) may emerge with far-reaching consequences for the dynamics. This is elaborated in Sec. 4.4.1.

4.2 Hamiltonian structure of 2D flows

Sec. 3 revealed that Lagrangian transport in many 3D flows is (locally) similar to that of 2D unsteady flows and the above advanced critical lines (Sec. 4.1.3) and closed trajectories (Sec. 4.1.4) as LCSs underlying such (effectively) 2D behaviour. Isolated critical points (Sec. 4.1.2), on the other hand, are key indicators of essentially 3D dynamics.

Hence the emergence (or absence) of such LCSs offers important insights into the nature of the Lagrangian motion. However, a more rigorous distinction of true 3D from (essentially) 2D dynamics than just based on LCSs is relevant for analysis and design of practical flows. Batch mixers using time-periodic stirring must e.g. operate at conditions yielding global 3D chaos such as in Fig. 26(a) (right); any (local) 2D behaviour implies sub-optimal performance of such devices. The ability to unambiguously distinguish between 2D and 3D dynamics enables identification and accomplishment of favourable operating conditions.

The 2D–3D distinction may rely upon the fundamental property that kinematic equation (2) for solenoidal 2D unsteady flows has a Hamiltonian structure, viz.

$$\frac{dx}{dt} = u_x = \frac{\partial H}{\partial y}, \quad \frac{dy}{dt} = u_y = -\frac{\partial H}{\partial x}, \quad (41)$$

with function $H = H(\vec{x}, t)$ its so-called ‘‘Hamiltonian’’ [242, 52]. The latter for steady conditions, i.e. $H = H(\vec{x})$, satisfies

$$\frac{dH}{dt} = \vec{u} \cdot \vec{\nabla} H = 0, \quad (42)$$

and thus restricts the motion of fluid parcels to its level sets. Property (42) renders H a so-called ‘‘constant of motion’’ (COM) and here defines the conventional stream function of 2D steady flows. Restriction of fluid motion to level sets of H precludes chaotic advection and thus puts forth unsteadiness, i.e. $H = H(\vec{x}, t)$, as a *necessary* (though not *sufficient*) condition for chaos in 2D flows [242, 52]. This namely invalidates property (42) by virtue of $dH/dt = \partial H/\partial t \neq 0$.²⁵ Flows devoid of chaotic behaviour due to the restriction of Lagrangian dynamics to level sets of a COM H are termed *integrable* [243]; H namely implicitly gives the solution $\vec{x}(t) = \vec{\Phi}_t(\vec{x}_0)$ to kinematic equation (2) via $H(\vec{x}(t)) = H(\vec{x}_0)$.

The Hamiltonian structure furthermore dictates that chaos, if occurring, emanates from the breakdown of islands following specific scenarios described by the well-known KAM and Poincaré-Birkhoff theorems [52, 243]. This results in the characteristic composition of flow topologies of systems exhibiting Hamiltonian chaos, i.e. large central islands encircled by island chains and embedded in a chaotic sea, as happening in e.g. the cross-sectional dynamics of the 3D steady flows shown in Fig. 18(d), Fig. 22 or Fig. 23(d). Counterparts to these theorems exist for such 3D steady flows exhibiting essentially 2D behaviour [43].

4.3 Hamiltonian dynamics in 3D steady flows

4.3.1 General

The fact that the Lagrangian dynamics in 2D solenoidal flows is always governed by Hamiltonian mechanics offers a way to establish whether a 3D steady flow exhibits (essentially) 2D dynamics. This notion namely implies that any

²⁵Steady/unsteady Hamiltonian systems are in dynamical-systems terminology commonly denoted autonomous/non-autonomous systems [243].

such flow must admit a (formal) transformation \mathcal{F} following (11) into a 2D unsteady system with a Hamiltonian structure according to (41). This transformation rests on three cornerstones. First, a coordinate transformation

$$\mathcal{G} : \vec{x} \rightarrow \vec{\xi}, \quad (43)$$

from the Cartesian frame $\vec{x} = (x, y, z)$ to an appropriate curvilinear reference frame $\vec{\xi} = (\xi_1, \xi_2, \xi_3)$ with scaling factors $h_i = |\partial\vec{x}/\partial\xi_i|$ and Jacobian $J = |\partial\vec{x}/\partial\vec{\xi}| = h_1 h_2 h_3$ following [244]. Second, the vector potential $\vec{\mathcal{A}}$ of \vec{u} for vanishing ξ_2 -component, i.e. $\vec{\mathcal{A}} = (\mathcal{A}_1, 0, \mathcal{A}_3)$, defined implicitly as

$$\begin{aligned} h_2 h_3 u_1 &= \tilde{u}_1 = \frac{\partial \tilde{\mathcal{A}}_3}{\partial \xi_2}, \\ h_1 h_3 u_2 &= \tilde{u}_2 = \frac{\partial \tilde{\mathcal{A}}_1}{\partial \xi_3} - \frac{\partial \tilde{\mathcal{A}}_3}{\partial \xi_1}, \\ h_1 h_2 u_3 &= \tilde{u}_3 = -\frac{\partial \tilde{\mathcal{A}}_1}{\partial \xi_2}, \end{aligned} \quad (44)$$

with $\tilde{\mathcal{A}}_i = h_i \mathcal{A}_i$ and $\tilde{u}_i = Ju_i/h_i$ the vector potential and flow, respectively, in the *Cartesian* frame spanned by $\vec{\xi}$. Third, expression of kinematic equation (2) in terms of $\vec{\xi}$ and $\vec{\mathcal{A}}$, i.e.

$$\begin{aligned} \frac{d\xi_1}{dt} &= \frac{u_1}{h_1} = \frac{\tilde{u}_1}{J} = \frac{1}{J} \frac{\partial \tilde{\mathcal{A}}_3}{\partial \xi_2}, \\ \frac{d\xi_2}{dt} &= \frac{u_2}{h_2} = \frac{\tilde{u}_2}{J} = \frac{1}{J} \left[\frac{\partial \tilde{\mathcal{A}}_1}{\partial \xi_3} - \frac{\partial \tilde{\mathcal{A}}_3}{\partial \xi_1} \right], \\ \frac{d\xi_3}{dt} &= \frac{u_3}{h_3} = \frac{\tilde{u}_3}{J} = -\frac{1}{J} \frac{\partial \tilde{\mathcal{A}}_1}{\partial \xi_2}, \end{aligned} \quad (45)$$

which reveals that the Lagrangian motion corresponds with rescaled flow \tilde{u}/J in said Cartesian $\vec{\xi}$ -frame: $d\vec{\xi}/dt = \tilde{u}/J$.

The simplest class of 3D steady flows with an embedded Hamiltonian structure involves cases that admit a transformation (43) such that the ξ_3 -wise flow in $\vec{\xi}$ -space is independent of ξ_3 and uni-directional: $\tilde{u}_3 = \tilde{u}_3(\xi_1, \xi_2) > 0$. This via (44) implies $\mathcal{A}_1 = \mathcal{A}_1(\xi_1, \xi_2)$ and, in turn, a Hamiltonian structure for the $\xi_{1,2}$ -wise component of (45) according to

$$\frac{d\xi_1}{dt} = \frac{\tilde{u}_1}{J} = \frac{1}{J} \frac{\partial H}{\partial \xi_2}, \quad \frac{d\xi_2}{dt} = \frac{\tilde{u}_2}{J} = -\frac{1}{J} \frac{\partial H}{\partial \xi_1}, \quad (46)$$

with $H = \mathcal{A}_3(\xi_1, \xi_2, \xi_3)$ the corresponding Hamiltonian. Property $d\xi_3/dt = \tilde{u}_3/J > 0$ (due to $\tilde{u}_3 > 0$ and non-singular transformation (43)) admits inversion of $\xi_3(t)$ and thus expression of the Hamiltonian as $H = H(\xi_1, \xi_2, t) = \mathcal{A}_3(\xi_1, \xi_2, \xi_3(t))$. Hence transformation (11) here becomes

$$\mathcal{F} : \zeta_1 = \xi_1, \quad \zeta_2 = \xi_2, \quad \tau = t. \quad (47)$$

Moreover, a steady Hamiltonian $H = H(\xi_1, \xi_2)$ yields

$$\frac{dH}{dt} = \vec{u} \cdot \vec{\nabla} H = \sum_{i=1}^3 \frac{u_i}{h_i} \frac{\partial H}{\partial \xi_i} = \sum_{i=1}^3 \frac{\tilde{u}_i}{J} \frac{\partial H}{\partial \xi_i} = 0. \quad (48)$$

demonstrating consistency of (46) with (41) and (42).

3D steady flows satisfying only the relaxed condition of a uni-directional ξ_3 -component of the physical flow, i.e. $u_3 > 0$ yet permitting $\partial\mathcal{A}_1/\partial\xi_3 \neq 0$ in (44) and (45), define a second class with an embedded Hamiltonian structure. Transformation (11) following [245], given by

$$\mathcal{F} : \zeta_1 = \xi_1, \quad \zeta_2 = -\tilde{\mathcal{A}}_1(\vec{\xi}), \quad \tau = \xi_3, \quad (49)$$

namely yields a Hamiltonian system according to (41) in canonical space $\vec{\zeta} = (\zeta_1, \zeta_2)$ and time τ , i.e.

$$\frac{d\zeta_1}{d\tau} = \frac{\partial H}{\partial \zeta_2}, \quad \frac{d\zeta_2}{d\tau} = -\frac{\partial H}{\partial \zeta_1}, \quad (50)$$

with Hamiltonian $H = H(\zeta_1, \zeta_2, \tau) = \tilde{\mathcal{A}}_3(\zeta_1, f(\zeta_1, \zeta_2, \tau), \tau)$ and $\xi_2 = f(\zeta_1, \zeta_2, \tau)$ implicitly defined via (49). Transformation (49) effectively translates the ζ_3 -wise flow into a time evolution, rendering ζ_3 a fictitious time.

4.3.2 Periodic duct flows

An important subclass of reoriented duct flows (9) belonging to the above *first class* of flows with an embedded Hamiltonian form are the so-called 2.5D duct flows, that is, simplified configurations where the base flow depends only on the transverse coordinates: $\vec{v} = \vec{v}(r, \theta)$ and $\tilde{u}_3(\xi_1, \xi_2) = v_z(r, \theta) > 0$. Transformation (47) applied to the Cartesian frame $\vec{\xi} = \vec{x}$ thus readily yields Hamiltonian form (46), with $H = H(r, \theta) = A_z(r, \theta)$, and here in fact identifies with (41). This renders the duct flow \vec{u} a cell-wise reorientation of a steady Hamiltonian system, meaning that chaotic advection can occur only due to jumping of tracers between cell-wise reorientations of the KAM tori of the base flow at the cell interfaces $z = kL$. The embedded Hamiltonian structure causes *all* 2.5D duct flows to behave according to one universal Hamiltonian scenario [83]. The 2.5D approximation is a standard modelling approach for periodic duct flows and inline mixers (Sec. 3.2.2) and is therefore adopted in many studies on such devices [52, 50]. The flow topology in the RAM in Fig. 7 is e.g. simulated with the 2.5D model from [83] and computational analyses on the PPM commonly use the 2.5D models by [52] and [87].

Smooth transition between cells yields – even in the Stokes limit – an essentially 3D duct flow $\vec{u}(x, y, z)$ that precludes Hamiltonian structure (46). However, such flows readily admit the *second class* of embedded Hamiltonian forms in case of uni-directional axial flow: $u_z(\vec{x}) > 0$ for all \vec{x} . This namely enables application of transformation (49)

directly to the Cartesian coordinates \vec{x} , resulting in

$$(\zeta_1, \zeta_2) = (x, -A_x(\vec{x})), \quad \tau = z, \quad H = A_z, \quad (51)$$

for the associated Hamiltonian form (50). Consider for example the 2.5D RAM flow in Fig. 7, which has an axial Poiseuille flow $v_z = u_z = 2U(1-r^2)$, with U the mean throughflow. Performing transformation (51) for the rescaled flow $\vec{u}' = \vec{u}/U$, which can be done without loss of generality, via $u'_z = 2(1-r^2)$ yields $A_x = 2y(y^2/3 + x^2 - 1)$ and a canonical versus physical cross-section following Fig. 55(a). The canonical representation of the cross-sectional topology in Fig. 7(b) is shown in Fig. 55(b) and retains its structure, signifying consistency. The 2.5D RAM flow also admits form (41) for reasons given above and can thus be reconciled with two equivalent Hamiltonian systems that employ either real time t or axial coordinate z as canonical time.²⁶

Transformation (51) applies to any duct flow with $u_z > 0$ everywhere and translates into a canonical space/topology that is an y -wise deformed version of the physical cross-section/topology akin to Fig. 55. The RAM flow in Fig. 9(a) and micro-mixer flow in Fig. 10 following [88] and [89], respectively, e.g. qualify for this approach.

3D steady duct flows with local axial backflow ($u_z < 0$) admit the second class of Hamiltonian forms (50) upon transformation (49) in the net throughflow region following Sec. 3.2.2, that is, the subregion connecting the periodic inlet-outlet allowing for a non-singular transformation (43) such that $u_3 > 0$ [86]. The remaining flow regions relate to essentially 3D LCSs as e.g. stagnation/periodic points due to internal recirculation zones or separatrices/manifolds emanating from critical points of the skin-friction field (18) on internal walls (as demonstrated in Fig. 47(b) for the flow inside a porous matrix). This happens in the RAM under essentially 3D conditions with significant fluid inertia [86] and is suspected in 3D partitioned-duct flows as e.g. the Quatro mixer in Fig. 11 or the CSM in Fig. 13.

4.3.3 Steady circulatory flows

Steady confined circulatory flows as e.g. the impeller-driven flow in Fig. 18 and the swirling flow in Fig. 22 for appropriate conditions admit the above embedded Hamiltonian forms in the reordered cylindrical frame $\vec{\xi} = (z, r, \theta)$ ($h_1 = h_2 = 1, h_3 = J = r$) using θ as time-like variable. Axisymmetric angular velocity $\omega = u_\theta/r = \omega(r, z) > 0$ yields

$$\frac{dr}{d\tau} = \frac{1}{r} \frac{\partial H}{\partial z}, \quad \frac{dz}{d\tau} = -\frac{1}{r} \frac{\partial H}{\partial r}, \quad (52)$$

as specific Hamiltonian form (46), with $H = r\mathcal{A}_\theta$ the Stokes stream function. Non-axi-symmetric angular velocity $\omega > 0$

²⁶Using the rescaled flow for transformation (51) ensures a straightforward link between the Hamiltonian forms. A uniform axial flow $u_z = U$ in that case namely results (via $u'_z = 1$) in $A_x = -y$ and thus identical canonical and physical spaces: $(\zeta_1, \zeta_2) = (x, y)$. Moreover, Hamiltonian systems (41) and (50) then identify upon substituting $H = UA_z$ and $t = \tau/U$ in the former.

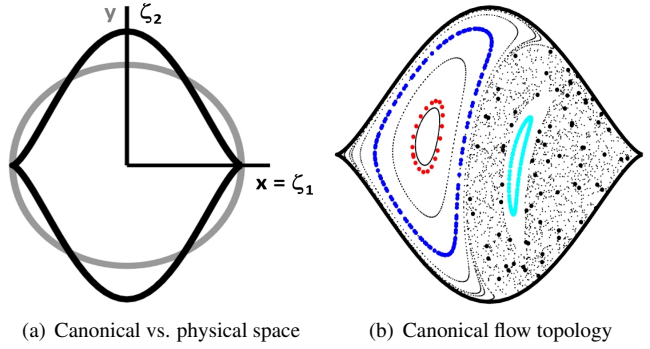


Fig. 55. Hamiltonian representation of the cross-sectional flow topology of the RAM in Fig. 7(b) following transformation (51).

gives Hamiltonian form (50) for

$$(\zeta_1, \zeta_2) = (z, -\mathcal{A}_z(\vec{x})), \quad \tau = \theta, \quad H = rA_\theta, \quad (53)$$

and constitutes the swirling-flow counterpart to transformation (51) for duct flows. Transformation (53), rescaling the flow with the mean angular velocity Ω , yields $\zeta_2 = -A_z = r^2/2$ for a uniform angular velocity ($\omega' = 1$) and, upon substitution into (50), coincides with (52). Hence uniform ξ_3 -wise flow also here causes the first and second class of embedded Hamiltonian forms to identify.

Swirling flows with local angular backflow ($\omega < 0$) admit Hamiltonian form (50) upon transformation (49) in a “net throughflow region” as in the above duct flows. Moreover, any circulatory flow can for appropriate conditions be reconciled with Hamiltonian form (50) in a similar way. The primary circulations about the toroidal axis in the tokamak in Fig. 17, the stagnation line (dots) in the steady cylinder flow in Fig. 23(a) as well as the black axis in the droplet flow in Fig. 36(b) correspond with canonical time τ , meaning that these systems admit a transformation equivalent to (53) upon connecting said axes with the z -axis.

4.4 Hamiltonian dynamics in 3D unsteady flows

4.4.1 Flows with continuous symmetry

A generalisation of the above first class of steady flows with embedded Hamiltonian forms (Sec. 4.3.1) concerns unsteady flows where \vec{u} following (44) becomes independent of one coordinate direction, say ξ_3 , for an appropriate transformation (43): $\vec{u} = \vec{u}(\xi_1, \xi_2, t)$. This happens if a steady solenoidal “flow” $\vec{w}(\vec{x})$ exists, with $\vec{x}(\lambda) = \vec{g}_\lambda(\vec{x}_0)$ the flow along its “streamlines” parameterised by “time” λ , such that each fluid trajectory $\vec{x}(t) = \vec{\Phi}_t(\vec{x}_0)$ has a companion

$$\vec{x}_*(t) = \vec{g}_\lambda(\vec{\Phi}_t(\vec{x}_0)) = \vec{\Phi}_t(\vec{g}_\lambda(\vec{x}_0)), \quad (54)$$

that is also a fluid trajectory [246]. Thus $\vec{x}_*(t)$ can be reached from \vec{x}_0 via two paths and the companion of a fluid trajectory follows from its advection by “flow” \vec{w} according to Fig. 54(b). This holds for any $\lambda \in \mathbb{R}$ and therefore gives

rise to a continuous family of companion trajectories. Hence \vec{w} defines a *continuous* symmetry and its “streamlines” coincide with fixed positions (ξ_1, ξ_2) in the curvilinear frame, or equivalently, the intersections of the coordinate surfaces of $\xi_{1,2}$ (implying $\vec{w} = w\vec{e}_3$ or, conversely, $\vec{e}_3 = \vec{w}/|\vec{w}|$).

Property (54) is equivalent to

$$\vec{w} \cdot \vec{\nabla} \vec{u} - \vec{u} \cdot \vec{\nabla} \vec{w} = 0, \quad (55)$$

and renders \vec{u} and \vec{w} commutative, meaning that a given position can be reached via flow by, first, \vec{u} and, second, \vec{w} or in reversed order as per Fig. 54(b). Condition (55) in conjunction with solenoidality of \vec{u} and \vec{w} through vector identity

$$\vec{\nabla} \times (\vec{u} \times \vec{w}) = \vec{w} \cdot \vec{\nabla} \vec{u} - \vec{u} \cdot \vec{\nabla} \vec{w} + \vec{u}(\vec{\nabla} \cdot \vec{w}) - \vec{w}(\vec{\nabla} \cdot \vec{u}), \quad (56)$$

yields

$$\vec{\nabla} \times (\vec{u} \times \vec{w}) = 0 \quad \Rightarrow \quad \vec{u} \times \vec{w} = -\vec{\nabla} H, \quad (57)$$

implying a COM H due to $\vec{u} \cdot \vec{\nabla} H = -\vec{u} \cdot \vec{u} \times \vec{w} = 0$ that defines a Hamiltonian for the $\xi_{1,2}$ -wise dynamics [246, 247]. Property $\vec{u} = \vec{u}(\xi_1, \xi_2, t)$ namely yields via vector potential (44) a Hamiltonian form (46), with here $H = \mathcal{A}_3(\xi_1, \xi_2, t)$, and a corresponding structure for \vec{u} satisfying (57) for $\vec{w} = h_3 \vec{e}_3$.²⁷ The independence of the Hamiltonian H on spatial coordinate ξ_3 has the important consequence that a continuous symmetry in a steady flow implies $H = H(\xi_1, \xi_2)$ and thus inherently non-chaotic dynamics.

Consider for example the RAM flow in Fig. 7 without reorientation, i.e. $\Theta_R = 0$ in (9), causing \vec{u} to identify with base flow \vec{v} and, given $\vec{v} = \vec{v}(x, y)$ here, resulting in $\vec{u} = \vec{u}(x, y)$. This puts forth uniform axial “flow” $\vec{w} = \vec{e}_z$ as symmetry and a Hamiltonian form of the cross-sectional flow following (41). The same symmetry and Hamiltonian form emerge for diminishing rotation rate of the outer cylinder; tracers then only “feel” the averaged flow $\vec{u} = N^{-1} \sum_{k=0}^{N-1} \vec{v}(r, \theta - k\Theta) = \vec{u}(r, \theta)$ [83]. The impeller-driven steady flow in Fig. 18 becomes axi-symmetric, i.e. $\vec{u} = \vec{u}(r, z)$, for tilt angle $\alpha = 0$ and thus in a similar way leads to a symmetry $\vec{w} = r\vec{e}_\theta$ and corresponding Hamiltonian form (52). Steady conditions preclude chaos in these flows for reasons mentioned before.

The time-periodic flow in Fig. 26(a) (left) due to reorientations of the steady lid-driven Stokes flow in Fig. 23(a) about the z -axis accommodates a continuous symmetry as above yet in a highly non-trivial manner. Time-reversal and ordinary reflectional symmetries according to (40) about planes $x = 0$ and $y = 0$, respectively, impose the structure

$$u_{r,z}(\vec{x}) = \check{u}_{r,z}(r, z) \cos \theta, \quad u_\theta(\vec{x}) = \check{u}_\theta(r, z) \sin \theta, \quad (58)$$

²⁷The coordinate transformation associated with the continuous symmetry in fact results in $d\vec{\xi}/dt = \hat{u}(\xi_1, \xi_2, t)$ for kinematic equation (45) and $J = J(\xi_1, \xi_2)$ [246]. Hence relation $\vec{u} = \vec{u}/J$ implies $\vec{u} = \hat{u}(\xi_1, \xi_2, t)$.

upon the steady base flow [136, 124]. This, via separation of variables of $dF_{1,2}/dt$ following (42), yields two COMs, i.e.

$$F_1(\vec{x}) = f_1(r, z), \quad F_2(\vec{x}) = f_2(r, z) \sin \theta, \quad (59)$$

that can be shown to relate to (58) through

$$\frac{\check{u}_r}{f_2} = \frac{1}{r} \frac{\partial f_1}{\partial z}, \quad \frac{\check{u}_z}{f_2} = -\frac{1}{r} \frac{\partial f_1}{\partial r}, \quad (60)$$

exposing f_1 as the Stokes stream function of flow $(\check{u}_r/f_2, \check{u}_z/f_2)$ in the rz -plane. This suggests an embedded Hamiltonian structure and associated continuous symmetry. Its isolation embarks on expressing kinematic equation $d\vec{x}/dt = \vec{u}$ in terms of the curvilinear frame $\vec{\xi} = (z, r, \alpha)$, with $\alpha = \ln(\sin \theta)$ substituting angular coordinate θ , yielding

$$\frac{d(r, z)}{dt} = \check{u}_{r,z} \cos \theta(\alpha), \quad \frac{d\alpha}{dt} = \frac{u_\theta}{h_\alpha} = \frac{\check{u}_\theta \cos \theta(\alpha)}{r}, \quad (61)$$

where $h_\alpha = J = r \tan \theta$, $\vec{e}_\alpha = \vec{e}_\theta$ and $u_\alpha = \vec{u} \cdot \vec{e}_\alpha = u_\theta$.²⁸ Introducing the rescaled flow $\vec{u}^* = \vec{u}/F_2$ via (60) gives

$$\frac{dz}{dt} = u_1^* = \frac{\check{u}_1^*}{J}, \quad \frac{dr}{dt} = u_2^* = \frac{\check{u}_2^*}{J}, \quad \frac{d\alpha}{dt} = \frac{u_3^*}{h_\alpha} = \frac{\check{u}_3^*}{J}, \quad (62)$$

as counterpart to (61), with

$$\vec{u}^* = \left(-\frac{\partial f_1}{\partial r}, \frac{\partial f_1}{\partial z}, \frac{\check{u}_\theta}{f_2} \right) = \vec{u}^*(\xi_1, \xi_2), \quad (63)$$

the corresponding flow (44) in the Cartesian $\vec{\xi}$ -frame. Its independence of ξ_3 signifies indeed a continuous symmetry and, in consequence, a Hamiltonian structure (46) exists. The underlying relation (57) follows in the Cartesian frame spanned by $\vec{\xi}$ from vector identity (56) as before: flow \vec{u}^* commutes with field $\vec{w}_1^* = \vec{e}_\alpha$ according to (55) and, given both fields are solenoidal, thus satisfy (57) for $H = -f_1 = -F_1$. However, counterparts \vec{u}^* and $\vec{w}_1^* = h_\alpha \vec{e}_\alpha$, or equivalently, \vec{u} and $\vec{w}_1 = (h_\alpha/F_2) \vec{e}_\alpha$ in *physical* space are non-commutative and, instead, via property

$$\vec{w} \cdot \vec{\nabla} \vec{u} - \vec{u} \cdot \vec{\nabla} \vec{w} = -\vec{u}(\vec{\nabla} \cdot \vec{w}), \quad (64)$$

yield

$$\vec{u}^* \times \vec{w}_1^* = \vec{u} \times \vec{w}_1 = \vec{\nabla} F_1, \quad (65)$$

from (56), since \vec{w}_1^* and \vec{w}_1 are non-solenoidal. Both \vec{u} and \vec{u}^* satisfying (65) reflects the fact that they relate by a scalar

²⁸Considering range $0 < \theta < \pi/2$ is sufficient due to symmetries; this gives $\sin \theta > 0$ and $\tan \theta > 0$ and thus a non-singular transformation.

multiplication factor F_2 and thus have coinciding streamlines and, in turn, the same embedded Hamiltonian structure.²⁹

COM F_2 in (59) emanates from interaction between \vec{u} and a second (non-solenoidal) field \vec{w}_2 following (64), i.e.

$$\vec{u} \times \vec{w}_2 = \vec{\nabla} F_2, \quad \vec{w}_2 = \check{w}_r \vec{e}_r + \check{w}_z \vec{e}_z, \quad (66)$$

with

$$\check{w}_r = \frac{1}{\check{\omega}r} \frac{\partial f_2}{\partial z}, \quad \check{w}_z = -\frac{1}{\check{\omega}r} \frac{\partial f_2}{\partial r}, \quad (67)$$

advancing f_2 as the Stokes stream function of $\check{\omega} \vec{w}_2$. The analogy with (60) implies an embedded Hamiltonian structure (46), with $H = -f_2$, in the ‘‘flow topology’’ of ‘‘flow’’ \vec{w}_2 . The latter emerges from essentially the same continuous symmetry as for axi-symmetric steady circulatory flows. Rescaled field $\vec{w}_2^* = (\check{\omega} \check{w}_z, \check{\omega} \check{w}_r, 0) = \vec{w}_2^*(r, z)$ in the reordered cylindrical frame $\vec{\xi} = (z, r, \theta)$ namely commutes with $\vec{g} = r \vec{e}_\theta$ following (55) and via (56) results in

$$\vec{w}_2^* \times \vec{g} = \vec{\nabla} f_2, \quad (68)$$

assuming form (57) for $H = -f_2$. This, given streamlines of both \vec{u} and \vec{w}_2 (and thus \vec{w}_2^*) are restricted to level sets of F_2 by virtue of (66), indirectly constitutes an embedded Hamiltonian structure for the fluid motion.

The above reveals that COMs $F_{1,2}$ following (59) can be reconciled with continuous symmetries according to [246], albeit in a non-trivial way. Solenoidal symmetries \vec{w} *directly* commuting with \vec{u} following (55) are non-existent in the lid-driven cylinder flow; COMs $F_{1,2}$ instead originate from interaction of \vec{u} with non-solenoidal fields $\vec{w}_{1,2}$ following (64) and thus via (56) lead to (65) and (66). Hence solenoidal symmetries \vec{w} commuting with \vec{u} as per (55) in fact constitute a subclass of systems that yield COMs via relation (57).

Relation (60) identifies the level sets of F_1 with surfaces of revolution of the level sets of Stokes stream function f_1 , or equivalently, the streamlines of flow $(\check{u}_r, \check{u}_z)$ in the rz -plane. Conversely, this causes the projection of 3D streamlines in the rz -plane to coincide with the level sets of f_1 [136, 124]. Axi-symmetry preserves COM F_1 in time-periodic flows involving reorientations of the bottom wall and the spheroids in Fig. 26(a) (left) and Fig. 27(b) (left) thus correspond with its level sets. COM F_2 , on the other hand, exists only in the steady base flow and the intersections of its level sets with those of F_1 define the closed streamlines in Fig. 23(a).

The restriction of the dynamics to invariant surfaces (i.e. the spheroidal level sets of $H_1 = -f_1$) implies (in terms of the intra-surface coordinates) an alternative Hamiltonian structure, with $H_2^* = F_2$, to that associated with $H_2 = -f_2$ in the base flow. This is elaborated in Sec. 4.4.2. Hamiltonian H_2^* *directly* (instead of *indirectly* through \vec{w}_2 following

(66)) governs the intra-surface dynamics and, via the reorientation of the base flow, becomes *non-autonomous* in the time-periodic flow, thus leading to intra-surface Hamiltonian chaos as demonstrated in Fig. 26(a) (left).

The two COMS $F_{1,2}$, or equivalently, the autonomous Hamiltonians H_1 and H_2^* in the steady base flow (by confining the dynamics to individual streamlines) implicitly define the full solution to kinematic equation (2) via $F_{1,2}(\vec{x}(t)) = F_{1,2}(\vec{x}_0)$. This renders the system *fully integrable* and, in consequence, entirely non-chaotic. The remaining single COM F_1 (or Hamiltonian H_1) in the corresponding time-periodic flow constitutes an only partial solution to (2), implying *partially integrability*, and permits 2D chaos within its level sets.

4.4.2 Flows with invariant surfaces

The flow topology of 3D unsteady flows with a single COM according to (42) is foliated into a continuous family of invariant surfaces defined by its level sets (as e.g. the spheroids associated with COM F_1 following (59)). The restriction of the Lagrangian dynamics to invariant surfaces implies an embedded Hamiltonian structure that may coexist with a possible Hamiltonian structure underlying these LCSs (as e.g. occurring in the cylinder flow).

Consider to this end kinematic equation (45) in a curvilinear frame $\vec{\xi} = (\xi_1, \xi_2, \xi_3)$ such that coordinates (ξ_1, ξ_2) and ξ_3 are tangent and normal, respectively, to said surfaces (i.e. the latter coincide with coordinate surfaces of ξ_3). Restriction to invariant surfaces implies $u_3 = 0$ and thus via $\vec{\nabla} \cdot \vec{u} = \sum_i \partial \tilde{u}_i / \partial \xi_i = 0$ a solenoidal intra-surface 2D flow (u_1, u_2) with, inherently, a Hamiltonian structure:

$$\frac{\partial \tilde{u}_1}{\partial \xi_1} + \frac{\partial \tilde{u}_2}{\partial \xi_2} = 0 \quad \Rightarrow \quad (\tilde{u}_1, \tilde{u}_2) = \left(\frac{\partial H}{\partial \xi_2}, -\frac{\partial H}{\partial \xi_1} \right). \quad (69)$$

This identifies with vector potential (44) for $\vec{\mathcal{A}}_1 = 0$ and $H = \mathcal{A}_3$, leading to Hamiltonian form (46) for the intra-surface dynamics described by (ξ_1, ξ_2) . Hamiltonian $H = H(\vec{\xi}, t)$ can be interpreted in two ways. First, as the union of intra-surface Hamiltonians $H = H(\xi_1, \xi_2, t; \xi_3)$ parameterised by normal coordinate ξ_3 . Second, as the global Hamiltonian $H = H(\xi_1, \xi_2, \xi_3; t)$ for the system ‘‘frozen’’ at a given time instance t . Here ξ_3 acts as a time-like variable reminiscent of the 3D steady duct and circulatory flows in Sec. 4.3, where ξ_3 -wise progression through the 3D flow topology is similar to uni-directional ‘‘flow’’ $u_3 > 0$.

The beforementioned spheroids define the invariant surfaces in the flow topology of the time-periodic cylinder flow in Fig. 27(b) (left). Tracers are within these LCSs restricted to streamlines defined by intersections of level sets of COMS F_1 and F_2 . This implies $H = F_2(\xi_1, \xi_2; \xi_3)$ as Hamiltonian in (69) for the corresponding base flow and a non-autonomous counterpart $H = H(\xi_1, \xi_2, t; \xi_3)$ constructed from its reorientation for the time-periodic flow. The typical Hamiltonian dynamics in ‘‘smaller’’ spheroids is demonstrated in Fig. 56(a) by the 3D (left) and corresponding intra-surface (right) stroboscopic map expressed in terms of the angu-

²⁹The embedded Hamiltonian structure associated with transformation (49) is equally invariant to rescaling of the flow field [245].

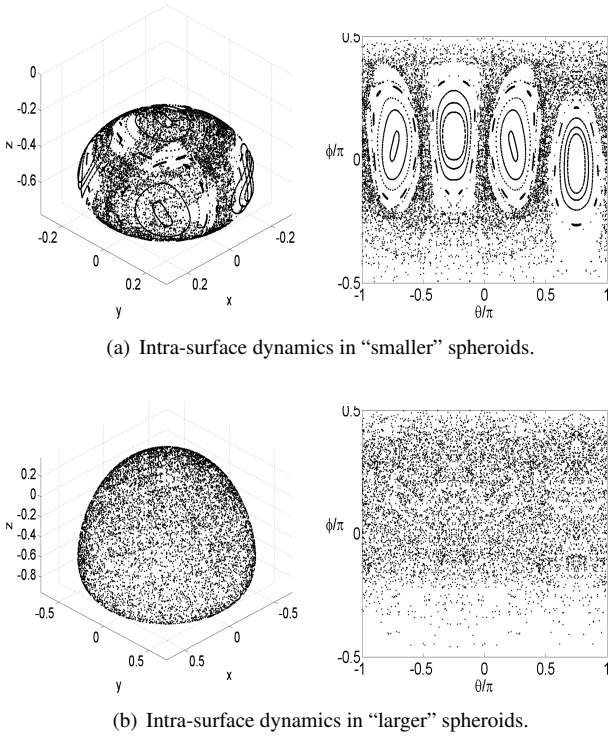


Fig. 56. Hamiltonian dynamics within invariant spheroids of non-inertial ($Re = 0$) time-periodic cylinder flow following Fig. 26(a) (left).

lar coordinates $(\xi_1, \xi_2) = (\theta, \phi)$ of the spherical reference frame attached to the common centre of the spheroids. (The cylinder mantle and top/bottom walls correspond with $r = 1$ and $z = \pm 1$, respectively. The common spheroid centre sits at $z \approx -0.56$.) This reveals a characteristic Hamiltonian topology consisting of (chains of) islands embedded in a chaotic sea. The intra-surface dynamics tends to become more chaotic upon progressing outwards in ξ_3 -direction as demonstrated in Fig. 56(b) for a “larger” spheroid. (Note that $\phi = \pm\pi/2$ corresponds with the spheroid poles; hence the lower tracer density in these regions.)

Fig. 56 exposes a substantial variation in intra-surface dynamics and this in fact reflects a fundamental difference with the abovementioned 3D steady flows. The latter are ξ_3 -wise periodic and thus invariably accommodate closed trajectories, which (besides possible localised phenomena) precludes qualitative topological changes in ξ_3 -direction (Sec. 4.1.4). Hence e.g. the tubes in the RAM in Fig. 7(a). The flow topology of 3D unsteady flows with invariant surfaces as the time-periodic cylinder flow, on the other hand, is generically *aperiodic* in ξ_3 and thus permits such changes. Hence the intra-surface dynamics in Fig. 56 and, inextricably linked with this, the partitioning of the periodic line in Fig. 27(b) into elliptic and hyperbolic segments.

The flow topology of the spherical tumbler for mixing of granular media in Sec. 3.3.2 for certain operating conditions also consists of invariant spheroids, meaning that the intra-surface dynamics shown in Fig. 28(b) (left) is of essentially the same Hamiltonian nature as in Fig. 56. Trans-

port studies using kinematic models for stroboscopic maps associated with 3D time-periodic flows reveal similar intra-surface Hamiltonian dynamics and chaos for a variety of surface topologies [140]. This substantiates its universality.

4.5 Link with 3D volume-preserving flows and maps

Steady solenoidal fluid flows and the stroboscopic maps of time-periodic solenoidal flows belong to the broader class of volume-preserving flows and maps,³⁰ respectively. Such generic flows and maps are widely used for studies on 3D (chaotic) advection, since they typically rely on simple kinematic models that are easy to treat computationally and often even admit analytical investigations. The well-known ABC flow e.g. first demonstrated the emergence of chaos in 3D steady flows and its discrete counterpart enabled first investigations on RID shown in Fig. 27(a) [141, 249, 248]. Moreover, both the ABC flow and map offered insights into the mechanisms underlying the particle clustering in Fig. 21 [119, 120]. Similar kinematic models established the generic nature of Hamiltonian chaos within invariant surfaces as shown for the time-periodic cylinder flow in Fig. 26(a) (left) and the emergence of RIM upon their perturbation as per Fig. 27(b) [140, 149].

Important in the present context is that kinematic models for volume-preserving flows and maps generically do *not* satisfy momentum conservation and thus, inherently, can capture only kinematic features of 3D Lagrangian transport. This includes the above embedded Hamiltonian structures yet excludes the fluid-dynamical mechanisms that facilitate such behaviour. Necessary for said structures is namely only the vector potential of the flow following (44), which exists solely by the grace of solenoidality, in combination with a kinematic condition as e.g. uni-directional flow or a continuous symmetry. Actual occurrence of a kinematic condition for a given Hamiltonian structure, on the other hand, depends essentially on dynamic conditions governed by momentum conservation. The continuous symmetry underlying the intra-surface Hamiltonian dynamics within the spheroids of the time-periodic cylinder flow in Fig. 56 e.g. hinges on the particular flow structure (58) that, in turn, results from geometric symmetries imparted on the flow due to the linearity of the momentum equation in the Stokes limit. Hence comprehensive 3D transport studies on realistic fluid flows must at some point always employ descriptions that satisfy both mass and momentum conservation. Refer to [43] for further discussion of kinematic versus dynamic conditions.

Furthermore relevant is that volume-preserving maps in the present scope derive from continuous time-periodic fluid flows and thus incorporate their dynamics. A stroboscopic map therefore has an embedded Hamiltonian structure only if this already exists in the underlying flow. Conversely, an essentially non-Hamiltonian time-periodic flow cannot produce a stroboscopic map with Hamiltonian dynamics. The intra-surface Hamiltonian structure within the spheroids of the beforementioned time-periodic cylinder flow e.g. is a direct consequence of the presence of these LCSs in the base

47 ³⁰Volume-preserving maps are also denoted “Liouvillian maps” [248].

flow and their invariance to reorientations of the driving wall. However, time-periodic flows thus constructed from reorientations of an essentially Hamiltonian base flow must not necessarily adopt the Hamiltonian nature. Said time-periodic cylinder flow for $Re = 100$ is essentially non-Hamiltonian, as reflected by the emergence of an isolated periodic point with global manifolds shown (Fig. 26(b)), notwithstanding the Hamiltonian behaviour of the base flow (Fig. 23(c)).

4.6 Towards essentially 3D (chaotic) dynamics

4.6.1 Conditions for chaos

The inherent Hamiltonian structure (41) of 2D flows makes a non-autonomous Hamiltonian $H = H(\vec{x}, t)$ a necessary kinematic condition for chaos (Sec. 4.2). Essentially 3D steady flows (i.e. dependent on all spatial coordinates) are in their simplest form dynamically equivalent to a 2D unsteady flow and thus a non-autonomous Hamiltonian system (Sec. 4.3). This has the fundamental implication that *any* 3D (un)steady flow meets the necessary kinematic criteria for chaos.³¹ Whether (and to what degree) chaos actually happens is dictated by momentum conservation. The structure of the momentum equation implies that realistic laminar flows (i.e. subject to both viscous and inertial forces) generically lack a universal dynamical restriction to chaos [43]. Hence such flows in principle always exhibit chaos in (at least) some regions and typically have a flow topology consisting of LCSs surrounded by chaos as illustrated by the RAM in Fig. 7. Global restrictions to chaos occur only for case-specific dynamic conditions as e.g. the symmetry-induced confinement to spheroids and, inherently, essentially 2D (chaotic) dynamics, in the non-inertial time-periodic cylinder flow following Fig. 26(a) (left).³²

The necessary *topological condition for chaos* is the transversal intersection of stable and unstable manifolds associated with hyperbolic points/lines/trajectories as per Sec. 4.1 [52, 243, 43]. Such interactions are denoted *homoclinic* and *heteroclinic* if involving (un)stable manifolds of the same or two different hyperbolic LCSs, respectively. Fig. 5(a) e.g. shows the homoclinic intersection of the stable (blue) and unstable (red) manifolds of the central hyperbolic point (cross) in the archetypal 2D time-period flow; these LCSs furthermore interact heteroclinically with manifolds (not shown) of the two adjacent hyperbolic points. The actual mechanism leading to exponential stretching of fluid parcels and, in consequence, chaotic advection is the accumulation of intersections upon approaching a periodic point along the stable/unstable manifold during forward/backward progression in time.

³¹ This more formally follows from the Poincaré–Bendixson theorem, which states that continuous dynamical systems – here kinematic equation (2) – admit chaos only for a corresponding phase space – here the space-time domain – that is at least 3D [243]. 3D flows evidently meet this condition.

³² Steady inviscid flows (i.e. so-called “Euler flows”) are, in stark contrast, generically *non-chaotic* due to the restriction of Lagrangian dynamics to level sets of the Bernoulli function $\zeta = p + \rho gz + \vec{u} \cdot \vec{u}/2$, with p the pressure, ρ the density and g the gravitational acceleration acting in $-z$ direction [43].

3D steady flows Transversal manifold interaction may in 3D steady flows occur via various scenarios. This generically excludes stagnation lines, since these entities are atypical of realistic flows. The elliptic stagnation lines that e.g. shape the idealised streamline topology of the cylinder flow in Fig. 23(a) and droplet flows in Fig. 36(a) for basically any perturbation give way to a hyperbolic focus and elliptic closed streamlines, respectively, in the corresponding non-ideal (i.e. realistic) topologies shown in Fig. 23(c), Fig. 23(b) and Fig. 36(b). Hence only isolated stagnation points and closed/periodic hyperbolic streamlines are of practical relevance. (This includes critical points of the skin-friction field on grounds of their equivalence to hyperbolic nodes; Sec. 4.1.) The 1D manifolds of stagnation points can immediately be ruled out from transversal interaction scenarios; they can intersect 2D manifolds namely only at stagnation points. However, this prevents progression of tracers along these intersections and thus violates the nature of manifolds. This constraint e.g. prohibits intersection of the 1D and 2D manifolds of the skin-friction field in Fig. 47(b).

Heteroclinic interaction between stagnation points and hyperbolic *closed* streamlines is possible via 9 scenarios following [250] (Fig. 57). Heteroclinic *transversal* interaction is restricted to 2D manifolds and, given the latter are stream surfaces, thus defines streamlines (denoted “heteroclinic trajectories”) with corresponding dynamics as follows:³³

- **Point–point interaction** (Sec. 4.1 of [250]): a single heteroclinic trajectory connects both points; exponential stretching is absent and thus dynamics are non-chaotic.
- **Point–line interaction** (Sec. 4.3 of [250]): two heteroclinic trajectories emerge from the point and asymptotically spiral towards a limit cycle defined by the closed streamline; accumulation of windings of the spiralling trajectories upon approaching the closed streamline and elongation of the 2D manifold of the line along the 1D manifold of the point signifies exponential stretching of both 2D manifolds and thus chaos.³⁴
- **Line–line interaction** (Sec. 4.4 of [250]): the intersecting (topologically cylindrical) manifolds yield two heteroclinic trajectories that asymptotically spiral both forward and backward in time to limit cycles defined by the closed streamlines; accumulation of windings upon approaching the latter again produces chaos. The cylindrical shape of the manifolds in fact implies intermediate heteroclinic trajectories (i.e. “Birkhoff’s signature” [250]) that, through the formation of so-called “lobes” [251], greatly increase the rate of stretching.

The 2D manifolds of single closed streamlines admit *homoclinic* intersection similar to the heteroclinic line–line interaction (Ch. 5 in [250]). These findings put forth point–line

³³ The flow topology of the convection cells in Fig. 44(a) e.g. results from heteroclinic *non-transversal* interactions between hyperbolic nodes in the stress-free fluid surface and free-slip bottom wall.

³⁴ This describes the topology of the interaction; the progression in time depends on the manifold stabilities. Interaction of the 2D unstable and 2D stable manifold of a point and line, respectively, yields spiralling forward and elongation backward in time. This reverses for opposite stabilities.

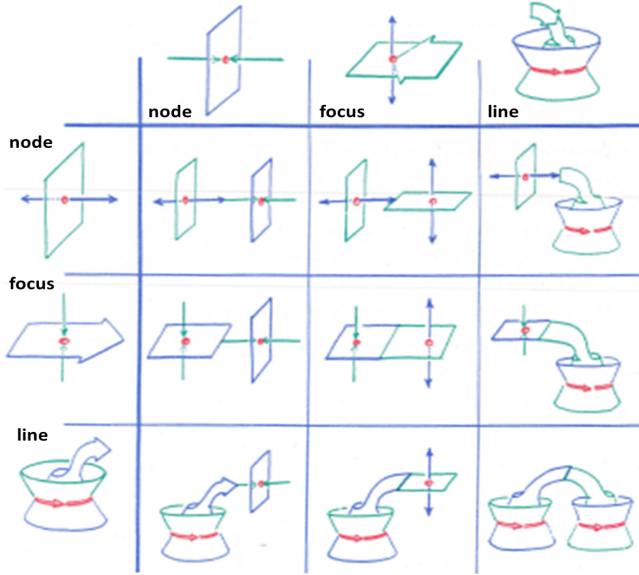


Fig. 57. Scenarios for heteroclinic interaction between stagnation points (red dots) and hyperbolic closed streamlines (red circles) in 3D steady flows. Blue/green lines/surfaces indicate unstable/stable 1D/2D manifolds. Adapted from [250].

and, by their topological complexity, particularly line–line interactions as “drivers” of chaos in 3D steady flows. However, 2D manifolds may also impede chaos in their capacity as barriers to 1D/2D manifolds of the same stability.

Hyperbolic *periodic* streamlines are also closed in the sense of reconnecting via a periodic inlet–outlet and thus admit the same point–line and line–line interactions as elaborated above. (Heteroclinic trajectories here “spiral” towards the limit cycle(s) via repeated reconnection.) However, heteroclinic interaction between *closed* and *periodic* streamlines is impossible (Conjecture 1 in [86]). Moreover, point–line interaction is possible only if the 2D stable (unstable) and 2D unstable (stable) manifolds of the point and streamline are exclusively interacting with each other (which follows from Conjecture 3 in [86]). These topological constraints are e.g. crucial to the emergence of a net throughflow region in periodic duct flows and, in consequence, the persistence of an embedded Hamiltonian structure in this subregion [86].

3D unsteady flows Topological freedom – and, inherently, the scenarios for transversal interaction – increases substantially for 3D unsteady flows. The 1D manifolds of isolated periodic points in stroboscopic maps can, for instance, intersect with 2D manifolds, thus permitting the homoclinic transversal manifold interaction for the hyperbolic focus in the time-periodic cylinder flow in Fig. 26(b).

Unsteady conditions furthermore allow for non-trivial point–point interactions leading to chaos. Consider e.g. the ideal buoyant droplet in Fig. 36(a) (left); its spherical surface and internal (black) axis are the merged 2D and 1D manifolds, respectively, of hyperbolic nodes at the axis endpoints. Aperiodic unsteady perturbation triggers transversal interaction of the manifolds of DHTs (aperiodic counterparts of hy-

perbolic nodes) following Fig. 40 and thus chaotic advection due to lobe formation akin to transversal line–line interactions. Similar behaviour occurs upon subjecting a droplet immersed in a steady swirling flow (its surface and axis emanate in a similar way as before from interacting hyperbolic foci) to time-periodic perturbations. This is demonstrated in Fig. 15 of [251] (originally from [252]).

The above examples concern chaos directly resulting from relaxation of topological restrictions of 3D steady flows. However, insights into the full set of transversal manifold interactions possible under essentially 3D unsteady conditions remain incomplete.

4.6.2 Conditions for 3D dynamics

Lagrangian transport in 2D solenoidal flows is governed by Hamiltonian mechanics due to the Hamiltonian structure (41) of kinematic equation (2) (Sec. 4.2). This notion enables rigorous distinction of essentially 2D dynamics from truly 3D dynamics in 3D solenoidal flows. The former namely implies an embedded Hamiltonian structure according to Sec. 4.3 and Sec. 4.4 in kinematic equation (2) relating to the physical flow via (formal) transformation (11); the latter implies (local) absence of such a structure.

The essentially 2D nature of the dynamics imparted by an embedded Hamiltonian structure suggests that the flow topology of such 3D flows is basically a “3D extrusion” of the typical Hamiltonian topology of 2D flows illustrated in Fig. 5(a) in the ξ_3 -direction of an appropriate curvilinear frame (43) following Sec. 4.3 and Sec. 4.4. Thus islands become tubes/tori centered on elliptic lines/closed trajectories defined in Sec. 4.1.3 and Sec. 4.1.4 surrounded by chaotic streamlines/trajectories as e.g. for the RAM in Fig. 7. Hence the emergence of such LCSs in the various configurations in Sec. 3 are clear indicators of (local) intrinsically 2D Hamiltonian dynamics. The breakdown of tubes/tori into chaos is described by 3D counterparts to the beforementioned KAM and Poincaré–Birkhoff theorems (Sec. 4.2) [253, 254].

The above advances (local) departure from or *a priori* absence of an embedded Hamiltonian structure in (2) as necessary kinematic condition for truly 3D (chaotic) dynamics in 3D (un)steady flows. Two important mechanisms in this respect are elaborated below: singularities and resonances.

Singularities Actual local breakdown of an embedded Hamiltonian structure manifests itself mathematically in singularities in the corresponding transformation (11). Consider as an instructive example the 2.5D duct flows introduced before, which (for $\bar{\xi} = \bar{x}$) adopt both Hamiltonian form (46) and (50) via transformation (47) and (49), respectively, due to the axial component of the base flow meeting $v_z(x, y) > 0$ (Sec. 4.3.2). The latter changing sign at $v_z = 0$ implies a non-monotonic relation $z(t)$, prohibiting its global inversion, and thus a singularity in transformation (47). Vanishing $u_3 = v_z$, similarly, yields a singular Jacobian $J_* = |\partial\bar{\zeta}/\partial\xi| = -\partial\tilde{A}_1/\partial\xi_2 = \tilde{u}_3$, with $\bar{\zeta} = (\zeta_1, \zeta_2, \tau)$, for transformation (49). Hence both cases only admit a local transformation into the respective Hamiltonian forms in sub-

regions $v_z > 0$ and $v_z < 0$ that, given continuity, are separated by (a) smooth surface(s) $v_z = 0$. Superposition of e.g. the previous 2.5D RAM flow with a uniform axial backflow of relative strength $0 \leq \alpha \leq 1$, i.e.

$$v_z = u_z = 2U(1 - r^2) - 2\alpha U = 2U(r_*^2 - r^2), \quad (70)$$

results in flow reversal from $v_z > 0$ to $v_z < 0$ at the cylindrical surface with radius $r_* = \sqrt{1 - \alpha}$. Transformation (51), again using $\vec{u}' = \vec{u}/U$, gives $J_* = 2(r_*^2 - r^2)$ and indeed becomes singular at $r = r_*$, implying a partitioning of the global dynamics into two coexisting Hamiltonian systems. Property $v_z = 0$ thus precluding a single global Hamiltonian structure, despite local dynamics retaining their Hamiltonian nature, is already an essentially 3D situation. Tracers generically namely can cross surfaces $v_z = 0$ and, within one global flow, switch between local Hamiltonian systems.³⁵

Partitioning into multiple Hamiltonian systems and/or restriction of Hamiltonian dynamics to subregions may furthermore stem from singularities in coordinate transform (43). Periodic duct flows, by expression in the curvilinear frame aligned with the 3D streamlines according to [86], e.g. in principle always meet condition $u_3 > 0$ necessary for a non-singular transformation (49). However, stagnation points and (further) topological complexity of the streamlines often rule out a single global transformation (43) and thus restrict embedded Hamiltonian structures to subregions admitting non-singular \mathcal{G} . Topological considerations strongly suggest that periodic duct flows accommodate at least one such subregion, viz. the beforementioned net throughflow region (possibly partitioned into multiple throughflow regions). Hence absence of a single global Hamiltonian structure again reflects an essentially 3D situation. Moreover, the net throughflow region (though itself accommodating Hamiltonian dynamics) may assume a complex structure particularly in partitioned-duct flows. Stagnation points and corresponding manifold interactions in the stagnation area of the T-shaped micro-mixer (Fig. 15b) are e.g. likely to have a major impact on the dynamics and structure of the (multiple) throughflow region(s).

Generic 3D (un)steady flows are likely to develop singularities in the transformation from physical to canonical space as well as in that from the Cartesian to an appropriate curvilinear frame – causing breakdown/restriction of (local) Hamiltonian structures – as exemplified above. Moreover, the number and/or region of influence of singularities generically grow with increasing departure from an originally Hamiltonian structure and thus progressively diminish the latter in favour of essentially 3D dynamics. The global topological complexity of the transversally-interacting 1D/2D manifolds of the isolated periodic point in the time-periodic cylinder flow for $Re = 100$ in Fig. 26(b) e.g. strongly suggests full breakdown of the Hamiltonian structure of the corresponding non-inertial limit ($Re = 0$) in Fig. 56.

³⁵This means that here $v_z \neq 0$, or generically, $u_3 \neq 0$ is sufficient for a non-singular transformation (49); the condition $u_{1,2,3} \neq 0$ (i.e. absence of stagnation points) according to [245] is unnecessarily stringent.

Resonances Resonances are a further mechanism that may lead to 3D dynamics by causing essentially 3D departures from 2D Hamiltonian dynamics. This may promote 3D chaos as well as formation of intricate LCSs as demonstrated in Fig. 27 by RID and RIM, respectively. The essence of these fundamentally distinct resonance phenomena is exemplified below by way of simplified maps.

RID may occur in (local) flow topologies consisting of tori as in Fig. 27(a) (left) described by trajectories spiralling around the toroidal axis. The Lagrangian motion is qualitatively similar to the helical trajectories along concentric tubes in a cylindrical periodic duct following

$$r_{p+1} = r_p, \quad \theta_{p+1} = \theta_p + \omega, \quad z_{p+1} = z_p + \gamma, \quad (71)$$

with $\omega = \omega(\vec{x}_0)$ and $\gamma = \gamma(\vec{x}_0)$ the period-wise azimuthal and axial displacement, respectively. The transverse (xy -wise) mapping is identical to the 2D elliptic mapping in (28) and (θ, z) represents the local poloidal/toroidal coordinates (ϕ, φ) following (13). Reconnection – and thus resonance – occurs for ω and γ forming rational fraction $\omega/\gamma = m/n$ as per (13). Generically $\omega = \omega(r)$ and $\gamma = \gamma(r)$, meaning that tori are either entirely non-resonant or resonant. Non-resonant tori survive weak perturbations according to the (3D counterpart of the) KAM theorem; resonant tori disintegrate following the corresponding Poincaré-Birkhoff theorems due to violation of the “averaging principle” first mentioned in Sec. 3.3.2 [243, 254]. (This violation in fact occurs both for “true” resonance and slow-down of motion along trajectories to the same order of magnitude as the perturbation.³⁶) Such torus-wise survival *or* breakdown is the “conventional” Hamiltonian route to chaos. Fig. 58(a) gives 3 neighbouring trajectories (distinguished by colour) in a periodic duct of unit radius and length 2π starting at the inlet $z = 0$ (bottom) from the marked positions on a typical resonant torus for $\gamma = 0.3$ and $(m, n) = (2, 3)$; thus reconnection occurs after 3 cycles and single trajectories appear as 3 segments. This torus disintegrates for any perturbation in an actual flow. Irrational ω/γ (e.g. $\omega/\gamma = \sqrt{2}$) yields a non-resonant (and surviving) torus densely filled by the trajectories (not shown).

However, 3D flows also admit resonances in subregions within tori, causing only local interruption of the averaging process and, in consequence, local defects in tori (rather than full breakdown). This may occur upon weak perturbation of a flow topology consisting entirely of reconnected

³⁶Consider for illustration the 2D simplification of (71) subject to a weak perturbation $\varepsilon \ll r_0$: $(r_{p+1}, \theta_{p+1}) = (r_p + \varepsilon \cos \theta_p, \theta_p + \omega)$. Non-resonant circulation (e.g. $\omega = \sqrt{2}$) yields angular positions θ_p that densely fill the range $0 \leq \theta \leq 2\pi$ and corresponding radii r_p that oscillate about r_0 with a bandwidth of $O(\varepsilon)$. Thus the tracer positions (r_p, θ_p) gradually describe a closed orbit that is approximately circular and has *average* radius $\bar{r} = \lim_{P \rightarrow \infty} \sum_{p=0}^{P-1} r_p / P = \int_0^{2\pi} r(\theta) d\theta / 2\pi = r_0$. This averaging process effectively neutralises the perturbations and the original circular orbit $r_p = r_0$ survives up to $O(\varepsilon)$. Resonant circulation $\omega = 2\pi$, on the other hand, yields $(r_p, \theta_p) = (r_0 + p\varepsilon \cos \theta_0, \theta_0)$ and thus causes a progressive radial drift of $O(p\varepsilon)$ and, in consequence, breakdown of the original circular orbit. This behaviour generalises to slow motion. Slow circulation $\omega = \varepsilon \ll 2\pi$ via $\cos \theta_p = \cos(\theta_{p-1} + \varepsilon) \approx \cos \theta_{p-1}$ namely gives $(r_p, \theta_p) \approx (r_0 + p\varepsilon \cos \theta_0, \theta_0 + p\varepsilon)$ and indeed results in a similar radial drift.

trajectories following Fig. 58(a) and, inherently, resonant tori. Consider for illustration an azimuthal displacement $\omega(r, \theta) = \omega_0(r) + \varepsilon \sin(\theta)$ such that ω_0 gives a rational fraction with γ as before and $\varepsilon = 0$ thus represents the unperturbed state. Perturbation $0 < \varepsilon \ll \omega_0$ breaks the rationality, except for isolated rational trajectories starting at $\theta_0 = 0$ and $\theta_0 = \pi$, and thus triggers dynamics as shown in Fig. 58(b) for $\omega_0/\gamma = m/n$, with (m, n) and U as before, and $\varepsilon = 5 \times 10^{-4}$: azimuthal drifting of tracers (black/blue) away from the rational trajectory (red). The drifting tracers delineate the torus segments partitioned by the rational trajectory; local defects develop at the latter and enable random jumps between tori and thus promote global dispersion of tracers (i.e. RID) as demonstrated in Fig. 27(a) (right) and observed or suspected in a range of other (un)steady 3D flows discussed in Sec. 3.³⁷

RID occurs if motion along unperturbed trajectories becomes of the same order as the perturbation due to resonance or local slow-down. This gives perturbed motion that is comparable in all coordinate directions and, in consequence, no longer restricted to the original tori. Behaviour akin to RID occurs if the (otherwise weak) perturbation has localised peaks of the same order as the typical motion along the unperturbed trajectories [255]. (Such peaks can e.g. develop in shear layers in granular media or non-Newtonian fluids.) The effect is similar as before: perturbed motion comparable in all coordinate directions that again causes local breakdown of tori. Thus both resonance/slow-down and perturbation peaks enable tracer dispersion across tori; differences primarily concern the intensity in that dispersion by former and latter mechanism is relatively slow and fast, respectively.³⁸

RIM may occur upon perturbation of flow topologies accommodating invariant surfaces “pierced” by (a) periodic line(s) as e.g. the spheroids in the Stokes limit $Re = 0$ of the time-periodic cylinder flow in Fig. 27(b) (left). Fluid inertia induces drift across the spheroids and yields Lagrangian motion transverse and parallel to the periodic line qualitatively similar to that near periodic points in 2D systems as per (26) and an axial uni-directional motion, respectively, i.e.

$$\vec{x}_{p+1}^\perp = F\vec{x}_p^\perp, \quad z_{p+1} > z_p, \quad (72)$$

with $\vec{x}^\perp = (x, y)$. Key to RIM is a z -dependent map $F = F(z)$ that smoothly changes its qualitative nature, determined by $J_1 = \text{tr}(F)$, at some axial position z_0 from $|J_1| < 2$ to $|J_1| > 2$, thus transiting from elliptic ($z < z_0$) to hyperbolic ($z > z_0$) dy-

namics, respectively. This happens in actual flows for (perturbed) periodic lines partitioned into elliptic ($|J_1| < 2$) and hyperbolic ($|J_1| > 2$) segments and thus merges tubes and shells – created on former and latter segments, respectively, by the averaging process – into intricate LCSs as demonstrated in Fig. 27(b) (right).

The degenerate points $|J_1| = 2$ separating elliptic and hyperbolic segments (denoted “parabolic points”) act as resonances by terminating and disconnecting the averaging processes that underlie the tube and shell formation and thus pave the way to their merger (i.e. RIM). Perturbations of the cylinder flow generically yield a uni-directional drift along the periodic line yet isolated periodic points may also emerge near the parabolic point as observed for some instances of RIM in the sphere-driven time-periodic flow studied in [149]. However, absence/presence of such periodic points is non-essential for RIM. The decisive kinematic condition is a qualitative change in dynamics due to segmentation of periodic lines.

Resonances as exemplified above occur for small departures from an intact embedded Hamiltonian structure comprising of complete LCSs and, unlike singularities, thus affect Lagrangian dynamics only under such conditions. Moreover, the topology of the LCSs is crucial for RID and RIM; former and latter phenomenon, if occurring, are inextricably linked to toroidal and spheroidal invariant surfaces, respectively Sec. 3.3.2. Chaotic advection resulting from RID and RIM (via e.g. “leaky shells; Sec. 3.3.2) therefore is relatively weak compared to a system far away from a Hamiltonian state as e.g. a flow topology dominated by manifolds of isolated periodic points following Fig. 26(b). Hence RID and RIM are (in a practical sense) primarily precursors to global chaos and of only limited use for (industrial) mixing purposes. The delicate and non-trivial LCSs formed by RID and RIM may, on the other hand, find practical applications other than mixing. Large departures from embedded Hamiltonian structures are in any case imperative to accomplish truly 3D (chaotic) dynamics yet insights into the response of 3D flow topologies – and their potential applications – to progressive perturbations are far from complete.

5 Commercialisation of chaotic advection

This section considers how the extensive scientific knowledge and insights of 3D Lagrangian transport developed over the last 30 years have migrated to industrial practice and technology. The success of translation is measured by the uptake of fluid chaos in patentable ideas, new devices that move beyond university laboratories and ultimately to the commercialisation and use of these ideas and devices in application. However, the process of taking a novel idea to a successful outcome is an arduous journey that is familiar to all who have attempted it. Although the practical uses of chaos are myriad, there is a general reluctance in traditional industries to adopt new technologies that are seen as untried and untested. Even in new industries and applications, the tendency to fall back on existing technology is strong.

Obtaining reliable information on commercialisation of

³⁷Resonances are often considered singularities as well. However, this is in the sense of interrupting the averaging process that underlies the formation/persistence of LCSs; they generically do *not* constitute singularities in the transformations to embedded Hamiltonian structures.

³⁸Reconsider for illustration the 2D simplification of (71) subject to a generally weak perturbation $\varepsilon \ll r_0$ as before yet with a localised peak of $O(r_0\omega)$ around radius $r = r_*$. Trajectories outside the vicinity of the peak (given non-resonant circulation) remain within a narrow band $|r_{p+1} - r_p| \sim O(\varepsilon)$ and thus again survive in an averaged way. Tracers on trajectories near this peak, on the other hand, undergo a radial “push” $|r_{p+1} - r_p| \sim O(r_0\omega)$ comparable to the azimuthal displacement of $O(r_0\omega)$ and thus are deflected. This deflection is essentially similar as for resonance/slow-down yet of greater intensity, i.e. $|r_{p+1} - r_p| \sim O(r_0\omega)$ versus $|r_{p+1} - r_p| \sim O(\varepsilon)$.

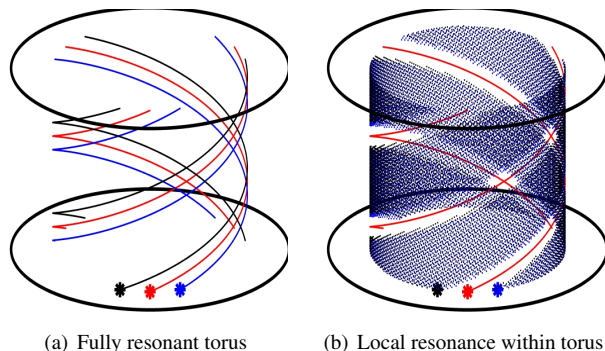


Fig. 58. Resonance demonstrated by 3 trajectories in a periodic cylindrical duct starting at the inlet $z = 0$ (bottom) from the marked positions: (a) fully resonant torus for $\omega = m\gamma/n$, $\gamma = 0.3$ and $(m, n) = (2, 3)$; (b) isolated resonant trajectory (red) separating torus segments delineated by drifting tracers (black/blue).

fluid chaos has proven difficult due to the sensitivity around intellectual property and a lack of clarity around ownership of ideas. Consequently, primarily the patent literature is examined. Although an application for patent protection is often a precursor for commercial applications, patent activity must be viewed cautiously from this viewpoint and can be seen only as an indicator. Most patents are never successfully commercialised and, conversely, some commercially successful ideas are never patented. This section finishes with a brief discussion of a number of technologies that have progressed to commercialisation.

5.1 Patents

An internet search using *Google Patent* (<https://patents.google.com>) with a search term of `''(chaos OR chaotic) AND (mixer OR mixing) AND fluid''` in October 2018 yielded a list of approximately 560 patents. This list was consolidated by removing duplicate patents in different jurisdictions, patents for identical devices claimed for different applications, devices that had nothing to do with fluid mixing and devices that claimed to use chaotic mixing as a loose terminology for turbulent mixing. Patents that mentioned in passing the use of unspecified “chaos/chaotic mixers” as one of many possibilities in a list of mixers were also discounted. Thus 293 patents remained and consisted of 173 patents for “stand alone” 3D chaos mixers and 120 patents in which chaotic mixing was explicitly mentioned as part of at least some embodiments of the patent. This latter group included patents where specific types of chaotic mixers were mentioned as well as those in which an unspecified “chaotic mixer” was explicitly mentioned as an integral part in at least some embodiments.

The cumulative number of chaotic mixing patents as a function of year is shown in Fig. 59, where mixer patents are clearly separated from those in which chaotic mixing is claimed only as part of the invention. The year plotted in this figure is based on the priority date, not the filing, publication or grant date because the priority date determines which is

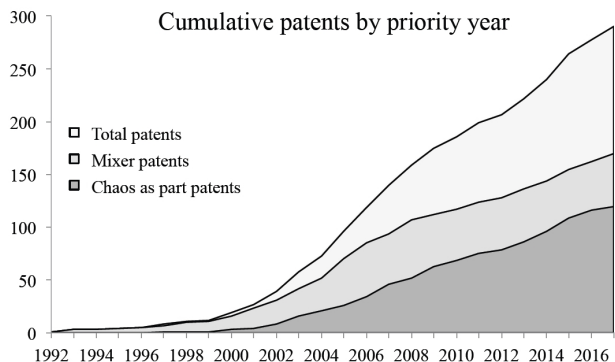


Fig. 59. Cumulative numbers of published chaotic mixing patents by priority year and category. Top curve is total patents, the middle curve is stand-alone mixers and the bottom curve is use of chaotic mixers as part of the invention in at least some embodiments

the “first application” in practice. The median time difference between priority and publication dates in this list was approximately 21 months, although time differences as high as 15 years were noted. The early history consists of patents that are fluid mixers only. In 1997 the first patent appears that specified the use of chaotic mixing as just part of the invention and by around 2005 the annual number of new mixers versus the use of chaos “in part” is approximately equal.

Several of the early patents are worth a special mention. Although the published patent record of chaotic advection begins in 1994 with the publication of four patents, the majority of these had earlier priority dates.

The patent with the earliest priority date (June 1992), and hence the honour of the first patented use of chaotic advection, belongs to Sen and Chang [256] of the Gas Research Institute in Illinois. Entitled “Process and Apparatus for enhancing In-Tube Heat Transfer by Chaotic Mixing”, their device exploits a twisted-pipe type of the duct flows following Sec. 3.2 used for heat exchange. The patent was allowed to lapse in 2002 and no record has been found regarding its use in application. With a priority date just 5 months later (Nov 1992), Castelain, Le Guer and Peerhossaini [257] also patented a twisted-pipe device for heat exchange. However, the record indicates the patent was disallowed and was withdrawn in 1998, possibly because the claims in Sen and Chang [256] encompassed those in [257].

Mackley, Skelton and Smith [258] patented a mixing vessel with a priority date in March 1993. It consisted of a duct with radial baffles that divides the tube into chambers and uses oscillatory flow (the first example of patenting time-dependent chaotic flow) to generate time-periodic separated flow with crossing streamlines in different phases of the period (similar to the reorientation of a base flow in the time-periodic cylinder flow in Fig. 26) and mixing throughout the tube. The record suggests this patent did not make it into the PCT stage and was abandoned in 1998; however, the technology has progressed as we detail later.

Tjahjadi and Foster of the General Electric company patented modifications to extruder screws (also belonging to the duct flows following Sec. 3.2) that generated chaotic mo-

tion in polymer melts to improve mixing and heat/mass transfer characteristics of the extruder. This patent had a priority date of September 1993, and appeared to have been maintained by General Electric until 2008 when it was assigned to Sabic Innovative Plastics B.V. of the Netherlands.

Also having a 1993 priority date, Logan [259] filed on a device to be inserted into ducts. Logan’s device has three long rods welded into an open triangular prism with sine wave baffles welded to the faces of the triangle, which the patent claims produces stretching, folding and chaotic mixing for viscous liquids. Most curiously, down the center of the triangle are acoustic horns claimed to provide additional mixing. We have been unable to find evidence that Logan’s device was ever tested and although payment was continued until 2006, the fate of the technology is unknown.

The only chaotic mixing patent with a 1994 priority date was that of Kwon and San [260] of the Pohang Iron and Steel company for another extruder screw that generated chaotic motion in polymers melts. Once again this patent was allowed to lapse in 2006, and no information has been found as to its commercialisation.

The early history of chaotic mixing patents is entirely filled by devices that are termed here “macro-scale” devices, operating at length scales from centimetres to metres. This changed in July 1997 with the first micromixing patent by Evans, Liepman and Pisano [261]. Unlike most subsequent micromixer designs, this device is not a duct. Instead it has a thin, planar chamber, into which fluid streams are pumped from alternating directions, making this system a container flow according to [Sec. 3.3](#). The time-periodic pulsation and their reorientation accomplish the mixing within the chamber. Fee payments on this patent were up to date in 2011.

The cumulative number of chaotic mixing patents is shown in Fig. 60, this time distinguishing between macro-scale and micro-scale patents. Again the year plotted in this figure is based on priority date. The most noticeable feature of this plot is that since approximately 2002, the number of patents filed annually at each scale is approximately constant, with micro-fluidic patents being filed approximately three times more frequently as macro-scale. A significant part of the micro-fluidic abundance is due to the “chaos as part of the working principle” patents seen in Fig. 59. With very few exceptions, these “chaos in part” patents involve the use of micromixers. Clearly the drive for miniaturisation and the concomitant drastic reduction in Reynolds number mentioned in [Sec. 1](#) has been one of the main drivers of new applications using chaotic advection. Moreover, the reduction of length scale has opened up the practical utilisation of diverse surface forces drive fluid motion on the micro scale, forces that are negligible at the macro scale.

Classification of patents according to the flow categories described in [Sec. 3](#) is also instructive and is shown in Table 1. Here screw extruders (10% of total patents) have been categorised as “partitioned-duct flows”, the majority of wall-driven container flows also involved unsteady driving and were categorised as “unsteady container flows” and that different inventions for mixing inside droplets were lumped together due to the small numbers – the majority (4% of to-

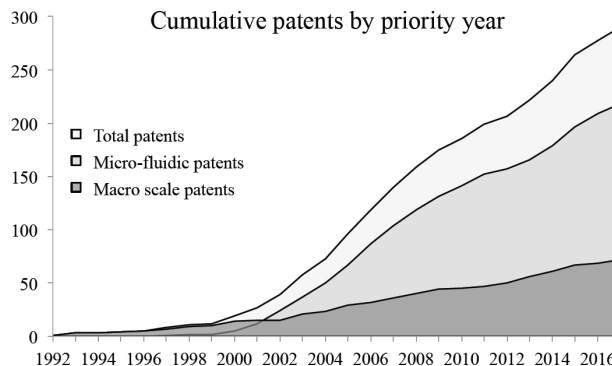


Fig. 60. Cumulative numbers of published chaotic mixing patents priority year and scale. Top curve is total patents, the middle curve is micromixers and the bottom curve is for macro-scale mixing devices.

tal patents) being background-flow driven. At 40% of total patents, open-duct flows have a clear majority, with approximately 50% of open-duct flow patents involving a means to drive a spatially or temporally varying cross flow either via patterned walls (e.g. a herringbone pattern) or via direct forcing (electro-kinetic, magnetic, varying wettability, mechanical). The other 50% of open-duct flow patents involve the use of duct geometry including 2D and 3D twisted and serpentine channels and/or wall baffles and/or varying channel cross section to generate secondary flows and streamline chaos. Worth noting is that very few fluid chaos patents involve flows that are spatially fully 3D, mirroring the nascent state of knowledge in such systems [43].

Table 1. Patent classification by percentage in terms of the flow categorisation following [Sec. 3](#).

Category	Percentage
Open-duct flows (Sec. 3.2.2)	40%
Partitioned-duct flows (Sec. 3.2.2)	13%
Unsteady container flows (Sec. 3.3.2)	8%
Branching and connecting (Sec. 3.2.2)	8%
Forced container flows (Sec. 3.3.2)	7%
Mixing inside droplets (Sec. 3.4.2)	7%
Other (various)	17%

5.2 Commercialisation attempts

The following presents a brief discussion of a few technologies that have attempted, and in some case succeeded, in commercialisation. Making connections between patents, inventors and current commercial activity has proven difficult, especially for patents that include chaotic mixing as part of the process. There are likely a number of other commercially available devices that have not been uncovered for this

review³⁹.

5.2.1 Kenics mixer

The Kenics mixer [92] is an in-line mixer with internal twisted, offset plates. It has been a commercial success for Chemineer Inc. (chemineer.com) since 1965 and has spawned numerous variations on the original theme (PPM, SMX, Quatro and a number of micro-fluidic equivalents). The inventors correctly identified the secondary flows induced by the twisted elements and the split-and-recombine nature of the flow (Sec. 3.2.2) as the source of effective mixing (“This results in an eddy current motion in each partial stream, which causes some mixing of components ... As the fluid meets the upstream edge of the second element it is forced to split again ...”). Although the device has been demonstrated numerous times to mix via the process of Lagrangian chaos, e.g. [262], the patent appeared well before the concept of Lagrangian fluid chaos had been described. Regardless, it is one of the stand-out examples of fluid chaos in practical application. The range of similar-style mixers to appear after the original patent lapsed points towards the difficulty in achieving successful commercialisation in the allowable 20-year window. It also suggests that opening up a concept to other minds provides the freedom to develop alternative, and potentially better, embodiments of the idea that could contribute to longer term success.

5.2.2 Oscillating Baffled Reactor

The patent by Mackley, Skelton and Smith [258] for “Processing of mixtures by means of pulsation” resulted in processes later termed Oscillatory Flow Mixing (malcolmmackley.com/innovation/oscillatory-flow-mixing) which is embodied in the Oscillatory Baffled Reactor (OBR). Although the original patent lapsed in 1998, at least two companies are commercialising the concept, Cambridge Reactor Design, (with the “Rattlesnake” continuous flow reactor (cambridgereactor.com)) and NiTech Solutions Ltd. (nitech.com) with chemical reactors and crystallisation vessels. Each company has more recent separate patents covering different aspects and applications of OBRs. NiTech Solutions has had commercial units operating in pharmaceutical manufacturing since 2007.⁴⁰ The advantages of the technology are clear when it is considered that one 2 m³ NiTech reactor operating at 100⁺ l/min has replaced two 150 m³ batch stirred tank reactors in one application. Other NiTech installations in a range of chemical manufacturing plants have been completed and around 50 lab-scale reactors have been installed in laboratories for pharma and chemical companies as well as in universities. The consistent message to emerge from installations of this type of reactor technology is that it makes the correct product reproducibly, creates less waste, there are less downstream unit operations required for separation and the process is generally greener and safer as a result.

³⁹Please contact the authors with information about successful commercial applications of chaos.

⁴⁰ Personal communication with Prof. Xiongwei Ni.

5.2.3 Rotated Arc Mixer

As introduced in Sec. 3.2, the Rotated Arc Mixer (RAM) is an in-line mixer without internal baffles designed on the basis of scientific insights into Lagrangian transport and the notion of chaotic advection (refer to www.youtube.com/watch?v=j0owt8XD6xM) The design was determined using *a priori* numerical simulation and the images shown in Fig. 8(a) are taken from the first experiment undertaken in the device in 1998. The poor and good mixing conditions and dye trace injection locations were identified *before* the experiment was run to highlight the robustness of the design methodology. The RAM can substantially outperform conventional inline mixers in terms of energy consumption and mixing quality, especially for highly viscous materials or materials in which fouling and scaling could rapidly clog internal mixing elements.

The elegance of the idea earned it recognition as one of the top designs in the “AIChE 10x Design Challenge” [263] in 2010. Two patents have been granted, one for flow mixing [264] and one for heat exchange [265]. Confidential trials of a full-scale RAM were undertaken in a plant owned and operated by a multinational food manufacturer. The outcome of the trial showed that the continuous-flow RAM increased line productivity by 25% (by fully accomplishing the desired material transformation so that downstream equipment could be operated at capacity) and reduced mixing energy by 95%, replacing two conventional mixers. Further, a sensory evaluation panel concluded that the RAM produced product had a “step change” improvement in product quality. Despite the apparent benefits of the RAM, implementation has not progressed beyond trials. This is a case-in-point of where a technology has been proven superior in application yet the conservatism inherent in large, traditional industries still results in a reluctance to adopt this.

Rights to develop the technology currently reside with Tasweld Engineering Pty Ltd. (tasweldengineering.com.au). Although the patents were allowed to lapse in 2018, in the case of the RAM, knowledge of the underlying Lagrangian transport is essential when designing a unit for a given application. It is this know-how – much of it encapsulated in this review – that will result in success or failure, not a knowledge of how to manufacture the physical device. This statement will be true of most devices based on Lagrangian chaos.

5.3 The future of commercial application

The approximately linear increase in fluid chaos patents year-on-year suggests that the technology field is still in the ascendancy or growth phase of the innovation S-curve. The difficulty in identifying successful commercialisations suggest it is likely in early growth. Significant take-off will require existing mixing processes to be increasingly replaced by those based on 3D deterministic Lagrangian chaos or will require emerging technologies that are created with fluid chaos as an integral part of their design.

Although some industries have used chaotic mixing devices for decades (for example screw extruders in polymer processing), most have not. The experience of the authors,

their colleagues and many companies they have talked to indicates there is a reluctance to utilise ideas and equipment that has not already been proven in other similar applications, even when pilot-scale testing has proven the utility and improved performance of fluid chaos in their applications. The difficulty in bootstrapping the use of fluid chaos is perhaps particularly disappointing given that it is generally possible to accurately predict the underlying deterministic flow which in turn allows good designs to be provided *a priori* that do not require significant iteration.

The proliferation of mixers spawned by the concepts embodied in the Kenics mixer might also suggest that a rush of commercialisation may arise once original patents have lapsed. This is potentially good news for processes where chaos has advantages, but less beneficial for the inventors and their financial backers. However, it seems likely that fluid chaos will make its impact felt in emerging technologies where it can be built in from the ground up. Indeed this appears to be the case in micro-fluidic applications, a large number of which require the use of 3D Lagrangian chaos in order to be viable. “Watch this space” seems to be an appropriate concluding instruction.

6 Concluding remarks

The scope of this review is transport and mixing of scalar quantities such as additives, chemical species, heat and nutrients in realistic three-dimensional (3D) fluid flows under laminar flow conditions. This is motivated by its ubiquity in many systems and processes both in industry and Nature. Transport and mixing is considered in terms of the Lagrangian motion of fluid parcels (“advection”) and thus admits description and investigation by the geometry, topology and coherence of fluid trajectories. This “Lagrangian flow topology” and corresponding advective transport has strong similarities and analogies across a wide range of practical flows in industry and beyond. This underlying universality of practical flows enables categorisation of laminar transport problems into four canonical configurations: flows in (i) ducts, (ii) containers, (iii) drops and (iv) webs.

The fundamental connections between many different instances of practical flows established by the proposed categorisation is the central outcome of the present review. This contributes to reaching its principal aim. *viz.* the stimulation of further development and utilisation of know-how on 3D Lagrangian transport, in three following ways. *First*, by exposing the ubiquity and diversity of Lagrangian transport phenomena and creating awareness of their broad relevance. *Second*, by enabling transfer of insights and knowledge between transport problems both within and across scientific disciplines. For example, the same mechanism of “chaotic advection” that yields efficient mixing in industrial inline mixers is also implicated in vascular diseases such as thrombosis and atherosclerosis. *Third*, by reconciling practical flows with fundamental and theoretical studies on Lagrangian transport and chaotic advection so as to bridge the still considerable gap between practice and theory. Studies and designs namely often insufficiently use the avail-

able scientific knowledge and expertise on laminar transport phenomena. Hence much can be gained by further cross-disciplinary research and these efforts should concentrate strongly on the fundamentals of Lagrangian transport in 3D realistic flows and its translation to design and understanding of practical applications.

Many challenges remain within this context. Those that have been exposed and suggested by this review include:

- *Lagrangian transport in realistic geometries* involving no-slip walls and non-periodic coordinates. The complex geometry of the flow domain is e.g. critical to transport in inline static (micro-)mixers or porous media.
- *Formation and interaction of Lagrangian coherent structures (LCSs) in 3D unsteady flows.* Transversal manifold interaction for critical points and lines in such flows remains elusive yet is key to truly 3D chaos.
- *Lagrangian (chaotic) transport far away from unperturbed states.* Fundamental studies often consider the response of non-chaotic systems to small perturbations and the resulting chaos due to e.g. RID and RIM is relatively weak and thus of limited use for practical mixing purposes. Hence *full* exploration of the routes that (via resonances and/or bifurcations) lead to strongly-3D (chaotic) conditions is of great practical relevance.
- *Lagrangian transport in aperiodic and finite-time (transient) flows.* Many realistic (particularly non-industrial) flows are aperiodic in space and/or time and thus beyond the existing Lagrangian machinery. This motivates the (ongoing) development of dedicated Lagrangian methods for such systems, which basically are generalisations of LCSs [266,59,75,190,251,267,268]. Important for practical usefulness is (at least) establishing consistency between the various definitions and interpretations of LCSs or, ideally, development of one comprehensive methodology for aperiodic/finite-time flows.
- *Lagrangian transport for non-mixing purposes.* The majority of Lagrangian transport studies attempt to destroy LCSs that obstruct transport in order to accomplish chaotic advection. However, LCSs may also be instrumentalised for non-mixing purposes such as e.g. “unmixing” of particle suspensions or the deliberate creation of coexisting mixing and entrapment regions [44,227]. Moreover, LCS-based concepts such as “burning invariant manifolds” to describe the propagation of reaction fronts may deepen insights into complex transport phenomena in chemically-reacting flows [269,270].
- *Lagrangian transport coupled to other physics.* Transport processes often involve significant contributions from diffusion and/or chemical reaction. Random-walk(-like) effects may come into play during advection of small particles or particle dispersion in random porous media. This enables crossing of topological barriers and thus tends to promote chaotic dynamics [60,216,194]. Such diffusive behaviour combines with advection into a net advective-diffusive flux that sets up scalar transport via well-defined “scalar transport paths”. This notion enables generalisation

of the concept of Lagrangian flow topology and LCSs to advective-diffusive transport – describing e.g. heat transfer by a “thermal topology” – and in fact any transport problem involving a continuous scalar flux [271,272]. This approach may pave the way to a unified Lagrangian formalism for scalar transport in fluid flows yet further development into a mature methodology is necessary for practical usefulness.

- *Lagrangian transport in discontinuous media.* Flowing media generically deform continuously due to the fact that the entire body of fluid remains smoothly connected. However, the flowing medium may under certain conditions be “cut up” into disconnected regions that are redistributed within the flow domain akin to the shuffling of a deck of cards. This happens, for instance, in case of extraction/injection of fluid via valves and discontinuous (i.e. “avalanche-like”) sliding within a granular medium. Here the front of the injected fluid and the sliding surface define material discontinuities that may significantly impact the Lagrangian flow topology and associated transport [273,274].
- *Experimental studies* Experimental studies must be an integral part of research efforts addressing these challenges so as to ensure physical meaningfulness and practical relevance of new insights.

A major challenge in its own right is instilling the “Lagrangian mindset” in scientists and practitioners in engineering and life sciences dealing with laminar transport phenomena in one form or another. This is also clearly reflected in the reluctance in industry to implement a proven principle as chaotic advection in actual mixing equipment, as suggested by the survey on relevant patents and commercial applications. This challenge can be overcome by, first, creating awareness of the relevance of these phenomena and the existence of dedicated machinery to describe and analyse them and, second, developing the necessary know-how and skills for its employment. The present review may be a first incentive to this end. Crucial in the long run is the structural integration of the “Lagrangian mindset” into education and training so as to expose students and practitioners alike to this approach and encourage its employment for analysis and design. Moreover, practical application necessitates its incorporation in handbooks and design strategies as well as in dedicated engineering and analysis tools such as CFD modules for Lagrangian transport studies.

Two of the authors (GM and MR) invented the RAM but retain no economic rights in its commercialisation.

References

[1] Harnby, N., Edwards, M., and Nienow, A., 1997. *Mixing in the Process Industries*. Butterworth-Heinemann, Oxford.

[2] Todd, D. B., 2004. *Mixing of Highly Viscous Fluids, Polymers, and Pastes*. Wiley-Blackwell, ch. 16, pp. 987–1025.

[3] Thakur, R., Vial, C., Nigam, K., Nauman, E., and Djelveh, G., 2003. “Static mixers in the process industries – a review”. *Trans IChemE*, **81**, p. 787.

[4] Weinekötter, R., 2009. “Compact and efficient continuous mixing processes for production of food and pharmaceutical powders”. *Trends Food Sci. Tech.*, **20**, p. S48.

[5] Erwin, L., 2011. “Mixing”. In *Encyclopedia of Polymer Science and Technology*, Encyclopedia of Polymer Science and Technology. John Wiley & Sons, Inc.

[6] Stone, H. A., Stroock, A. D., and Ajdari, A., 2004. “Engineering flows in small devices: microfluidics toward a lab-on-a-chip”. *Annu. Rev. Fluid Mech.*, **36**, p. 381.

[7] Squires, T. M., and Quake, S. R., 2005. “Microfluidics: Fluid physics at the nanoliter scale”. *Rev. Mod. Phys.*, **77**, pp. 977–1026.

[8] LaPorte, T., and Wang, C., 2007. “Continuous processes for the production of pharmaceutical intermediates and active pharmaceutical ingredients”. *Curr. Opin. Drug Discov. Devel.*, **10**, p. 738.

[9] Kockmann, N., 2007. *Trans. Phenom. Micro Process Engng.* Springer, Berlin.

[10] Becht, S., Franke, R., Geißelmann, A., and Hahn, H., 2007. “Micro process technology as a means of process intensification”. *Chem. Eng. Technol.*, **30**, p. 295.

[11] Mills, P. L., Quiram, D. J., and Ryley, J. F., 2008. “Microreactor technology and process miniaturization for catalytic reactions. a perspective on recent developments and emerging technologies”. *Chem. Engng Sci.*, **62**, p. 6992.

[12] Kjeang, E., Djilali, N., and Sinton, D., 2009. “Microfluidic fuel cells: A review”. *J. Power Sources*, **186**(2), pp. 353 – 369.

[13] Wu, Z., and Nguyen, N.-T., 2009. “Passive and active micromixers”. In *Micro Process Engineering*, J. C. S. V. Hessel, A. Renken and J.-I. Yoshida, eds., Micro Process Engineering. Wiley-VCH Verlag GmbH & Co. KGaA, pp. 175–203.

[14] Harmsen, J., 2010. “Process intensification in the petrochemicals industry: Drivers and hurdles for commercial implementation”. *Chem. Engng Process.: Process Intensif.*, **49**, pp. 70–73.

[15] Lutze, P., Gani, R., and Woodley, J. M., 2010. “Process intensification: A perspective on process synthesis”. *Chem. Engng Process.: Process Intensif.*, **49**, pp. 547–558.

[16] Suh, Y. K., and Kang, S., 2010. “A review on mixing in microfluidics”. *Micromachines*, **1**(3), pp. 82–111.

[17] Oh, P. P., Lau, H. L. N., Chen, J., Chong, M. F., and Choo, Y. M., 2012. “A review on conventional technologies and emerging process intensification (pi) methods for biodiesel production”. *Renew. Sustain. Energy Rev.*, **16**, pp. 5131–5145.

[18] Ward, K., and Fan, Z. H., 2015. “Mixing in microfluidic devices and enhancement methods”. *Journal of Micromechanics and Microengineering*, **25**(9), p. 094001.

- [19] Karimi, M., Bahrami, S., Mirshekari, H., Basri, S. M. M., Nik, A. B., Aref, A. R., Akbari, M., and Hamblin, M. R., 2016. “Microfluidic systems for stem cell-based neural tissue engineering”. *Lab Chip*, **16**, pp. 2551–2571.
- [20] Brown, D. W., Duchane, D. V., Heiken, G., and Hriscu, V. T., 2012. *Mining the Earth’s heat: hot dry rock geothermal energy*. Springer.
- [21] Chen, J., and Jiang, F., 2015. “Designing multi-well layout for enhanced geothermal system to better exploit hot dry rock geothermal energy”. *Renew. Ener.*, **74**, pp. 37–48.
- [22] Seredkin, M., Zabolotsky, A., and Jeffress, G., 2016. “In situ recovery, an alternative to conventional methods of mining: exploration, resource estimation, environmental issues, project evaluation and economics”. *Ore Geol. Rev.*, **79**, pp. 500–514.
- [23] Guo, K., Li, H., and Yu, Z., 2016. “In-situ heavy and extra-heavy oil recovery: A review”. *Fuel*, **185**, pp. 886 – 902.
- [24] Cunningham, J. A., and Reinhard, M., 2002. “Injection-extraction treatment well pairs: an alternative to permeable reactive barriers”. *Groundwater*, **40**(6), pp. 599–607.
- [25] Goltz, M. N., and Christ, J. A., 2012. “Recirculation systems”. In *Delivery and Mixing in the Subsurface: Processes and Design Principles for In Situ Remediation*, P. K. Kitanidis and P. L. McCarty, eds. Springer, New York, pp. 139–168.
- [26] Ottino, J. M., and Khakhar, D. V., 2000. “Mixing and segregation of granular materials”. *Annu. Rev. Fluid Mech.*, **32**(1), pp. 55–91.
- [27] Meier, S. W., Lueptow, R. M., and Ottino, J. M., 2007. “A dynamical systems approach to mixing and segregation of granular materials in tumblers”. *Adv. Phys.*, **56**(5), pp. 757–827.
- [28] Schlick, C. P., Isner, A. B., Freireich, B. J., Fan, Y., Umbanhowar, P. B., Ottino, J. M., and Lueptow, R. M., 2016. “A continuum approach for predicting segregation in flowing polydisperse granular materials”. *J. Fluid Mech.*, **797**, pp. 95–109.
- [29] Schelin, A., Károlyi, G., de Moura, A., Booth, N., and Grebogi, C., 2009. “Chaotic advection in blood flow”. *Phys. Rev. E*, **80**(1), p. 016213.
- [30] Tsuda, A., Laine-Pearson, F. E., and Hydon, P. E., 2011. “Why chaotic mixing of particles is inevitable in the deep lung”. *J. Theoret. Biol.*, **286**, pp. 57–66.
- [31] Henry, F. S., Haber, S., Haberthuer, D., Filipovic, N., Milasinovic, D., Schittny, J. C., and Tsuda, A., 2012. “The simultaneous role of an alveolus as flow mixer and flow feeder for the deposition of inhaled submicron particles”. *ASME. J. Biomech. Eng.*, **134**, pp. 121001–121001–11.
- [32] Pittman, R. N., 2013. “Oxygen transport in the microcirculation and its regulation”. *Microcirculation*, **20**(2), pp. 117–137.
- [33] Ferrua, M. J., Xue, Z., and Singh, R. P., 2014. “On the kinematics and efficiency of advective mixing during gastric digestion a numerical analysis”. *J. Biomech.*, **47**, pp. 3664–3673.
- [34] Koslover, E. F., Chan, C. K., and Theriot, J. A., 2017. “Cytoplasmic flow and mixing due to deformation of motile cells”. *Biophys. J.*, **113**(9), pp. 2077 – 2087.
- [35] Coltice, N., G erault, M., and Ulvrova, M., 2017. “A mantle convection perspective on global tectonics”. *Earth Sci. Rev.*, **165**, pp. 120 – 150.
- [36] Wiggins, S., 2004. “The dynamical systems approach to Lagrangian transport in oceanic flows”. *Annu. Rev. Fluid. Mech.*, **37**, pp. 295–328.
- [37] Dijkstra, H., 2005. *Nonlinear Physical Oceanography: A Dynamical Systems Approach to the Large Scale Ocean Circulation and El Nino*. Springer, New York.
- [38] Samelson, R., 2013. “Lagrangian motion, coherent structures, and lines of persistent material strain”. *Annu. Rev. Marine Sci.*, **5**(1), pp. 137–163.
- [39] Prants, S., Uleysky, M., and Budyansky, M., 2017. *Lagrangian Oceanography: Large-scale Transport and Mixing in the Ocean*. Physics of Earth and Space Environments. Springer International Publishing.
- [40] Dimotakis, P. E., 2005. “Turbulent mixing”. *Annu. Rev. Fluid Mech.*, **37**(1), pp. 329–356.
- [41] Aref, H., 1984. “Stirring by chaotic advection”. *J. Fluid Mech.*, **143**, p. 1.
- [42] Aref, H., 2002. “The Development of Chaotic Advection”. *Phys. Fluids*, **14**, pp. 1315–1323.
- [43] Aref, H., Blake, J. R., Budišić, M., Cardoso, S., Cartwright, J. H. E., Clercx, H. J. H., Feudel, U., Golestanian, R., Gouillart, E., Le Guer, Y., van Heijst, G. F., Krasnopolskaya, T. S., MacKay, R. S., Meleshko, V. V., Metcalfe, G., Mezić, I., de Moura, A. P. S., El Omari, K., Piro, O., Speetjens, M. F. M., Sturman, R., Thiffeault, J.-L., and Tuval, I., 2017. “Frontiers of chaotic advection”. *Rev. Mod. Phys.*, **89**, p. 025007.
- [44] Wang, S., Metcalfe, G., Stewart, R. L., Wu, J., Ohmura, N., Fenge, X., and Yang, C., 2014. “Solid-liquid separation by particle-flow-instability”. *Energy Environ. Sci.*, **7**, pp. 3982–3988.
- [45] Markl, M., Kilner, P. J., and Ebbers, T., 2011. “Comprehensive 4D velocity mapping of the heart and great vessels by cardiovascular magnetic resonance”. *J. Cardiovas. Magnet. Res.*, **13**(7).
- [46] Stocker Group, Civil and Environmental Engineering, MIT www.aps.org/units/dfd/pressroom/gallery/2012/fernandez12.cfm.
- [47] Shapiro, O. H., Fernandez, V. I., Garren, M., Guasto, J. S., Debailon-Vesque, F. P., Kramarsky-Winter, E., Vardi, A., and Stocker, R., 2014. “Vortical ciliary flows actively enhance mass transport in reef corals”. *Proc. Nat. Acad. Sci.*, **111**(37), pp. 13391–13396.
- [48] Shapiro, O. H., Kramarsky-Winter, E., Gavish, A. R., Stocker, R., and Vardi, A., 2016. “A coral-on-a-chip microfluidic platform enabling live-imaging microscopy of reef-building corals”. *Nature Comm.*, **7**, p. 10860.

- [49] Wiggins, S., 2010. “Coherent structures and chaotic advection in three dimensions”. *J. Fluid Mech.*, **654**(1986), pp. 1–4.
- [50] Ottino, J. M., and Wiggins, S., 2004. “Designing optimal micromixers”. *Science*, **305**, pp. 485–6.
- [51] Salmon, R., 1988. “Hamiltonian fluid mechanics”. *Annu. Rev. Fluid Mech.*, **20**(1), pp. 225–256.
- [52] Ottino, J. M., 1989. *The Kinematics of Mixing: Stretching, Chaos, and Transport*. Cambridge University Press.
- [53] Ottino, J. M., 1990. “Mixing, chaotic advection, and turbulence”. *Annu. Rev. Fluid Mech.*, **22**(1), pp. 207–254.
- [54] Meiss, J. D., 1992. “Symplectic maps, variational principles and transport”. *Rev. Mod. Phys.*, **64**, p. 795.
- [55] Wiggins, S., 1992. *Chaotic Transport in Dynamical Systems*. Interdisciplinary applied mathematics. Springer-Verlag.
- [56] Arnold, V. I., and Khesin, B. A., 1992. “Topological methods in hydrodynamics”. *Annu. Rev. Fluid Mech.*, **24**(1), pp. 145–166.
- [57] Morrison, P. J., 1998. “Hamiltonian description of the ideal fluid”. *Rev. Mod. Phys.*, **70**, pp. 467–521.
- [58] Mezić, I., 2013. “Analysis of fluid flows via spectral properties of the Koopman operator”. *Annu. Rev. Fluid Mech.*, **45**, pp. 357–37.
- [59] Haller, G., 2015. “Lagrangian coherent structures”. *Annu. Rev. Fluid Mech.*, **47**, p. 137.
- [60] Metcalfe, G., Speetjens, M. F. M., Lester, D. R., and Clercx, H. J. H., 2012. “Beyond passive: Chaotic transport in stirred fluids”. *Adv. Appl. Mech.*, **45**, pp. 109–188.
- [61] Villermaux, E., 2019. “Mixing versus stirring”. *Annu. Rev. Fluid Mech.*, **51**(1), p. null.
- [62] Hobbs, D., and Muzzio, F., 1997. “The Kenics static mixer: a three-dimensional chaotic flow”. *Chem Eng J.*, **67**, pp. 153–166.
- [63] Szalai, E. S., and Muzzio, F. J., 2003. “Fundamental approach to the design and optimization of static mixers”. *AIChE J.*, **49**, p. 26872699.
- [64] Stremmer, M. A., Haselton, F. R., and Aref, H., 2004. “Designing for chaos: applications of chaotic advection at the microscale”. *Phil. Trans. Roy. Soc. London A*, **362**(1818), pp. 1019–1036.
- [65] E.L. Paul, V.A. Atiemo-Obeng, S. K., 2004. *Handbook of Industrial Mixing: Science and Practice*. Wiley.
- [66] Metcalfe, G., Rudman, M., Brydon, A., Graham, L. J. W., and Hamilton, R., 2006. “Composing Chaos: An Experimental and Numerical Study of an Open Duct Mixing Flow”. *AIChE Journal*, **52**(1), pp. 9–28.
- [67] Zumbrennen, D. A., Subrahmanian, R., Kulshreshtha, B., and Mahesha, C., 2006. “Smart blending technology enabled by chaotic advection”. *Adv. Polymer Tech.*, **25**(3), pp. 152–169.
- [68] Tiwari, B., and Cullen, P. J., 2009. “Kinematics of flow and mixing mechanisms”. In *Food Mixing*, P. J. Cullen, ed., Food Mixing. Blackwell Publishing Ltd., pp. 21–49.
- [69] Zumbrennen, D. A., 2011. *Applied Plastics Engineering Handbook, Processing and Materials*. Elsevier Books, ch. Chaotic Advection and its Application to Extruding Micro- and Nano-Structured Plastic Materials, pp. 401–415.
- [70] Meijer, H. E., Singh, M. K., and Anderson, P. D., 2012. “On the performance of static mixers: A quantitative comparison”. *Prog. Polymer Sci.*, **37**(10), pp. 1333 – 1349.
- [71] Hessel, V., and Noël, T., 2012. “Micro process technology, 2. processing”. In *Ullmann’s Encyclopedia of Industrial Chemistry*, Ullmann’s Encyclopedia of Industrial Chemistry. Wiley-VCH Verlag GmbH & Co. KGaA.
- [72] Ghanem, A., Lemenand, T., Valle, D. D., and Peerhosaini, H., 2014. “Static mixers: mechanisms, applications, and characterization methods a review”. *Chem. Engng Res. Design*, **92**, pp. 205–228.
- [73] Cullen, P., and Misra, N., 2015. “Laminar mixing fundamentals”. In *Pharmaceutical Blending and Mixing*, N. A. P.J. Cullen, R. J. Romaach and C. D. RIELLY, eds., Pharmaceutical Blending and Mixing. John Wiley & Sons, Ltd, pp. 43–56.
- [74] Mezić, I., Loire, S., Fonoberov, V. A., and Hogan, P., 2010. “A new mixing diagnostic and gulf oil spill movement”. *Science*, **330**(6003), pp. 486–489.
- [75] Budišić, M., Siegmund, S., Son, D. T., and Mezić, I., 2016. “Mesochronic classification of trajectories in incompressible 3D vector fields over finite times”. *Disc. Contin. Dyn. Sys. - S*, **9**, pp. 923–958.
- [76] Kraume, M., Merz, C., and Henzler, H.-J., 2010. “Continuous mixing of fluids”. In *Ullmann’s Encyclopedia of Industrial Chemistry*, Vol. 10 of *Ullmann’s Encyclopedia of Industrial Chemistry*. Wiley-VCH Verlag GmbH & Co. KGaA.
- [77] Dickey, D. S., 2010. “Mixing and blending”. In *Kirk-Othmer Encyclopedia of Chemical Technology*, Kirk-Othmer Encyclopedia of Chemical Technology. John Wiley & Sons, Inc., pp. 1–71.
- [78] Freund, H., and Sundmacher, K., 2011. “Process intensification, 3. process unit level”. In *Ullmann’s Encyclopedia of Industrial Chemistry*, Ullmann’s Encyclopedia of Industrial Chemistry. Wiley-VCH Verlag GmbH & Co. KGaA.
- [79] Danckwerts, P. V., 1952. “The definition and measurement of some characteristics of mixtures”. *Appl. Sci. Res.*, **A3**, pp. 279–296.
- [80] Alberini, F., Simmons, M., Ingram, A., and Stitt, E., 2014. “Assessment of different methods of analysis to characterise the mixing of shear-thinning fluids in a kenics km static mixer using PLIF”. *Chem. Engng Sci.*, **112**, pp. 152 – 169.
- [81] “www.ansys.com/products/fluids”.
- [82] Moser, F., and Mathys, P., 2006. “A new tool for CFD simulation of laminar flow in mixers”. *Sulzer Technical Review 2*.
- [83] Speetjens, M. F. M., Metcalfe, G., and Rudman, M.,

2006. “Topological mixing study of non-Newtonian duct flows”. *Phys. Fluids*, **18**.
- [84] Baskan, O., Rajaei, H., Speetjens, M. F. M., and Clercx, H. J. H., 2017. “Scalar transport in inline mixers with spatially periodic flows”. *Phys. Fluids*, **29**, p. 013601.
- [85] Kusch, H. A., and Ottino, J. M., 1992. “Experiments on Mixing in Continuous Chaotic Flows”. *J. Fluid Mech.*, **236**, pp. 319–348.
- [86] Speetjens, M. F. M., Demissie, E. A., Metcalfe, G., and Clercx, H. J. H., 2014. “Lagrangian transport characteristics of a class of three-dimensional inline-mixing flows with fluid inertia”. *Phys. Fluids*, **26**, p. 113601.
- [87] Meleshko, V., Galaktionov, O., Peters, G., and Meijer, H., 1999. “Three-dimensional mixing in Stokes flow: the partitioned pipe mixer problem revisited”. *Eur. J. Mech. - B/Fluids*, **18**(5), pp. 783–792.
- [88] Singh, M. K., Anderson, P. D., Speetjens, M. F. M., and Meijer, H. E. H., 2008. “Optimizing the rotated arc mixer”. *AIChE J.*, **54**, pp. 2809–2822.
- [89] Suh, Y. K., Heo, S. G., Heo, Y. G., Heo, H. S., and Kang, S., 2007. “Numerical and experimental study on a channel mixer with a periodic array of cross baffles”. *J. Mech. Sci. Tech.*, **21**(3), pp. 549–555.
- [90] Stroock, A. D., and McGraw, G. J., 2004. “Investigation of the staggered herringbone mixer with a simple analytical model”. *Phil. Trans. Roy. Soc. London A*, **362**(1818), pp. 971–986.
- [91] Farshchian, B., Amirsadeghi, A., Choi, J., Park, D. S., Kim, N., and Park, S., 2017. “3D nanomolding and fluid mixing in micromixers with micro-patterned microchannel walls”. *Nano Convergence*, **4**(1), p. 4.
- [92] Armeniades, C., Johnson, W., and Raphael, T., 1965. Mixing device, Nov. 29. U.S. Patent 3,286,992.
- [93] Kim, D. S., Lee, I. H., Kwon, T. H., and Cho, D.-W., 2004. “A barrier embedded Kenics micromixer”. *J. Micromech. Microengng*, **14**(10), p. 1294.
- [94] Jilisen, R. T. M., Bloemen, P. R., and Speetjens, M. F. M., 2013. “Three-dimensional flow measurements in a static mixer”. *AIChE J.*, **159**, pp. 1746–1761.
- [95] Kumar, V., Shirke, V., and Nigam, K., 2008. “Performance of Kenics static mixer over a wide range of Reynolds numbers”. *Chem. Eng J.*, **139**, pp. 284–295.
- [96] Kang, T. G., Singh, M. K., Anderson, P. D., and Meijer, H. E. H., 2009. “A chaotic serpentine mixer efficient in the creeping flow regime: from design concept to optimization”. *Microfluid. Nanofluid.*, **7**(6), p. 783.
- [97] Kang, T. G., and Anderson, P. D., 2014. “The effect of inertia on the flow and mixing characteristics of a chaotic serpentine mixer”. *Micromachines*, **5**(4), pp. 1270–1286.
- [98] Hoffmann, M., Schaeter, M., and Raebiger, N., 2006. “Experimental investigation of liquid-liquid mixing in T-shaped micro-mixers using μ -LIF and μ -PIV”. *Chem. Engng Sci.*, **61**(9), pp. 2968 – 2976.
- [99] Vétel, J., Garon, A., and Pelletier, D., 2009. “Lagrangian coherent structures in the human carotid artery bifurcation”. *Exp. Fluids*, **46**(6), pp. 1067–1079.
- [100] Boozer, A., 2005. “Physics of magnetically confined plasmas”. *Rev. Mod. Phys.*, **76**, p. 1071.
- [101] Hazeltine, R. D., and Meiss, J. D., 1992. *Plasma Confinement*. Addison Wesley, Redwood City.
- [102] Pires, C. J. A., Saettone, E. A. O., Kucinski, M. Y., Vannucci, A., and Viana, R. L., 2005. “Magnetic field structure in the tcabr tokamak due to ergodic limiters with a non-uniform current distribution: theoretical and experimental results”. *Plasma Phys. Control. Fusion*, **47**(10), p. 1609.
- [103] Marcus, F., Kroetz, T., Roberto, M., Caldas, I., da Silva, E., Viana, R., and Guimares-Filho, Z., 2008. “Chaotic transport in reversed shear tokamaks”. *Nuclear Fusion*, **48**(2), p. 024018.
- [104] Onofri, M., Malara, F., and Veltri, P., 2011. “Role of anisotropic thermal conductivity in the reversed-field pinch dynamics”. *Phys. Plasmas*, **18**, p. 052502.
- [105] Caldas, I. L., Viana, R. L., Abud, C. V., Fonseca, J. C. D., Filho, Z. O. G., Kroetz, T., Marcus, F. A., Schelin, A. B., Jr, J. D. S., Toufen, D. L., Benkadda, S., Lopes, S. R., Morrison, P. J., Roberto, M., Gentle, K., Kuznetsov, Y., and Nascimento, I. C., 2012. “Shearless transport barriers in magnetically confined plasmas”. *Plasma Phys. Control. Fusion*, **54**(12), p. 124035.
- [106] Cardozo, N. L., 2006. “Anomalous transport due to magnetic turbulence”. *Trans. Fusion Sci. Tech.*, **49**, p. 300.
- [107] de Rover, M., Schilham, A. M. R., Montvai, A., and Cardozo, N. J. L., 1999. “Test particle transport in perturbed magnetic fields in tokamaks”. *Phys. Plasmas*, **6**, p. 2443.
- [108] Alexandroff, P., 1961. *Elementary Concepts of Topology*. Dover Books on Mathematics. Dover Publications.
- [109] Grumann, M., Geipel, A., Riegger, L., Zengerle, R., and Ducree, J., 2005. “Batch-mode mixing on centrifugal microfluidic platforms”. *Lab Chip*, **5**, pp. 560–565.
- [110] Gopalakrishnan, S., and Thess, A., 2010. “Chaotic mixing in electromagnetically controlled thermal convection of glass melt”. *Chem. Engng Sci.*, **65**(19), pp. 5309 – 5319.
- [111] Strohmeier, O., Keller, M., Schwemmer, F., Zehnle, S., Mark, D., von Stetten, F., Zengerle, R., and Paust, N., 2015. “Centrifugal microfluidic platforms: advanced unit operations and applications”. *Chem. Soc. Rev.*, **44**, pp. 6187–6229.
- [112] Petkovic, K., Metcalfe, G., Chen, H., Gao, Y., Best, M., Lester, D., and Zhu, Y., 2017. “Rapid detection of hendra virus antibodies: an integrated device with nanoparticle assay and chaotic micromixing”. *Lab Chip*, **17**, pp. 169–177.
- [113] Fountain, G. O., Khakhar, D. V., and Ottino, J. M., 1998. “Visualization of three-dimensional chaos”. *Science*, **281**, pp. 683–686.

- [114] Fountain, G. O., Khakhar, D. V., Mezić, I., and Ottino, J. M., 2000. “Chaotic mixing in a bounded three-dimensional flow”. *J. Fluid Mech.*, **417**, pp. 265–301.
- [115] Alvarez, M., Guzmán, A., and Elías, M., 2005. “Experimental visualization of mixing pathologies in laminar stirred tank bioreactors”. *Chem. Engng Sci.*, **60**(8-9), pp. 2449–2457.
- [116] Alvarez-Hernández, M., Shinbrot, T., Zalc, J., and Muzzio, F., 2002. “Practical chaotic mixing”. *Chem. Engng Sci.*, **57**(17), pp. 3749–3753.
- [117] Davidson, P. A., 1999. “Magnetohydrodynamics on materials processing”. *Annu. Rev. Fluid Mech.*, **31**(1), pp. 273–300.
- [118] Contreras, P. S., Speetjens, M. F. M., and Clercx, H. J. H., 2017. “Lagrangian transport in a class of three-dimensional buoyancy-driven flows”. *J. Fluid Mech.*, **832**, pp. 5–40.
- [119] Cartwright, J. H. E., Magnasco, M. O., Piro, O., and Tuval, I., 2002. “Bailout embeddings and neutrally buoyant particles in three-dimensional flows”. *Phys. Rev. Lett.*, **89**, p. 264501.
- [120] Sapsis, T., and Haller, G., 2010. “Clustering criterion for inertial particles in two-dimensional time-periodic and three-dimensional steady flows”. *Chaos*, **20**(1), p. 17515.
- [121] Sotiropoulos, F., Webster, D. R., and Lackey, T. C., 2002. “Experiments on Lagrangian transport in steady vortex-breakdown bubbles in a confined swirling flow”. *J. Fluid Mech.*, **466**, pp. 215–248.
- [122] Shankar, P. N., 1997. “Three-dimensional eddy structure in a cylindrical container”. *J. Fluid Mech.*, **342**, pp. 97–118.
- [123] Shankar, P. N., and Deshpande, M. D., 2000. “Fluid mechanics in the driven cavity”. *Annu. Rev. Fluid Mech.*, **32**, pp. 93–136.
- [124] Speetjens, M. F. M., Clercx, H. J. H., and van Heijst, G. J. F., 2004. “A numerical and experimental study on advection in three-dimensional Stokes flows”. *J. Fluid Mech.*, **514**, pp. 77–105.
- [125] Znaien, J., Speetjens, M. F. M., Trieling, R. R., and Clercx, H. J. H., 2012. “Observability of periodic lines in three-dimensional lid-driven cylindrical cavity flows”. *Phys. Rev. E*, **85**(6), p. 066320.
- [126] Shankar, P. N., 1998. “Three-dimensional Stokes flow in a cylindrical container”. *Phys. Fluids*, **10**(3), pp. 540–549.
- [127] Lackey, T. C., and Sotiropoulos, F., 2006. “Relationship between stirring rate and Reynolds number in the chaotically advected steady flow in a container with exactly counter-rotating lids”. *Phys. Fluids*, **18**(5), p. 53601.
- [128] Speetjens, M. F. M., de Wispelaere, H. N. L., and van Steenhoven, a. a., 2011. “Multi-functional Lagrangian flow structures in three-dimensional AC electro-osmotic micro-flows”. *Fluid Dyn. Res.*, **43**(3), p. 035503.
- [129] Cartwright, J. H. E., Feingold, M., and Piro, O., 1996. “Chaotic advection in three-dimensional unsteady incompressible laminar flow”. *J. Fluid Mech.*, **316**, pp. 259–284.
- [130] Mezić, I., 2001. “Break-up of invariant surfaces in action-angle-angle maps and flows”. *Phys. D*, **154**, pp. 51–67.
- [131] Speetjens, M. F. M., 2001. “Three-dimensional chaotic advection in a cylindrical domain”. PhD thesis, Eindhoven University of Technology - Department of Applied Physics.
- [132] Salafi, T., Zeming, K. K., and Zhang, Y., 2017. “Advancements in microfluidics for nanoparticle separation”. *Lab Chip*, **17**, pp. 11–33.
- [133] Liu, Z., Speetjens, M. F. M., Frijns, A. J. H., and van Steenhoven, A. A., 2014. “Application of astigmatism μ -PTV to analyze the vortex structure of AC electroosmotic flows”. *Microfluid. Nanofluid.*, **16**(3), pp. 553–569.
- [134] Arratia, P., Shinbrot, T., Alvarez, M., and Muzzio, F., 2005. “Mixing of non-Newtonian fluids in steadily forced systems”. *Phys. Rev. Lett.*, **94**(8), p. 084501.
- [135] Miles, K. C., Nagarajan, B., and Zumbrennen, D. A., 1995. “Three-dimensional chaotic mixing of fluids in a cylindrical cavity”. *J. Fluids Engng*, **117**(4), pp. 582–588.
- [136] Malyuga, V. S., Meleshko, V. V., Speetjens, M. F. M., Clercx, H. J. H., and van Heijst, G. J. F., 2002. “Mixing in the Stokes flow in a cylindrical container”. *Proc. Roy. Soc. A*, **458**, pp. 1867–1885.
- [137] Anderson, P. D., Ternet, D., Peters, G. W. M., and Meijer, H. E. H., 2006. “Numerical/Experimental Analysis of Chaotic Advection in a Three-Dimensional Cavity Flow”. In *International Polymer Processing XXI*, no. IPP0125, Carl Hanser Verlag, pp. 412–420.
- [138] Brouwer, L. E. J., 1911. “Über Abbildung von Mannigfaltigkeiten”. *Math. Annalen*, **71**, p. 97.
- [139] Speetjens, M. F. M., Clercx, H. J. H., and van Heijst, G. J. F., 2006. “Inertia-induced coherent structures in a time-periodic viscous mixing flow”. *Phys. Fluids*, **18**, p. 83603.
- [140] Gómez, A., and Meiss, J. D., 2002. “Volume-preserving maps with an invariant”. *Chaos*, **12**, pp. 289–299.
- [141] Dombre, T., Frisch, U., Greene, J. M., Hénon, M., Mehr, A., and Soward, A. M., 1986. “Chaotic streamlines in the ABC flows”. *J. Fluid Mech.*, **167**, pp. 353–391.
- [142] Rypina, I. I., Pratt, L. J., Wang, P., Özgökmen, T. M., and Mezić, I., 2015. “Resonance phenomena in a time-dependent, three-dimensional model of an idealized eddy”. *Chaos*, **25**(8), p. 087401.
- [143] Bajer, K., and Moffatt, H. K., 1992. *Chaos Associated with Fluid Inertia*. Springer Netherlands, Dordrecht, pp. 517–534.
- [144] Solomon, T. H., and Mezić, I., 2003. “Uniform resonant chaotic mixing in fluid flows”. *Nature*, **425**, pp. 376–380.
- [145] Vainchtein, D. L., Neishtadt, A. I., and Mezić, I.,

2006. “On passage through resonances in volume-preserving systems”. *Chaos*, **16**(4), p. 43123.
- [146] Arnold, V., 1978. *Mathematical Methods of Classical Mechanics*. Graduate Texts in Mathematics. Springer New York.
- [147] Speetjens, M. F. M., Clercx, H. J. H., and van Heijst, G. J. F., 2006. “Merger of coherent structures in time-periodic viscous flows”. *Chaos*, **16**, p. 43104.
- [148] Pouransari, Z., Speetjens, M. F. M., and Clercx, H. J. H., 2010. “Formation of coherent structures by fluid inertia in three-dimensional laminar flows”. *J. Fluid Mech.*, **654**, pp. 5–34.
- [149] Moharana, N. R., Speetjens, M. F. M., Trieling, R. R., and Clercx, H. J. H., 2013. “Three-dimensional Lagrangian transport phenomena in unsteady laminar flows driven by a rotating sphere”. *Phys. Fluids*, **25**, p. 093602.
- [150] Wu, F., and D. L. Vainchtein, M. F. M. S., Trieling, R. R., and Clercx, H. J. H., 2014. “Comparative numerical-experimental analysis of the universal impact of arbitrary perturbations on transport in three-dimensional unsteady flows”. *Phys. Rev. E*, **90**, p. 063002.
- [151] Christov, I., Lueptow, R., Ottino, J., and Sturman, R., 2014. “A study in three-dimensional chaotic dynamics: Granular flow and transport in a bi-axial spherical tumbler”. *SIAM J. Appl. Dyn. Sys.*, **13**(2), pp. 901–943.
- [152] Yagi, T., Sato, A., Shinke, M., Takahashi, S., Tobe, Y., Takao, H., Murayama, Y., and Umezumi, M., 2013. “Experimental insights into flow impingement in cerebral aneurysm by stereoscopic particle image velocimetry: transition from a laminar regime”. *J. Roy. Soc. Inter.*, **10**(82).
- [153] Závodszy, G., Károlyi, G., and Paál, G., 2015. “Emerging fractal patterns in a real 3D cerebral aneurysm”. *J. Theoret. Biol.*, **368**, pp. 95 – 101.
- [154] Tsuda, A., Henry, F. S., and Butler, J. P., 1995. “Chaotic mixing of alveolated duct flow in rhythmically expanding pulmonary acinus”. *J. Applied Physiol.*, **79**(3), pp. 1055–1063.
- [155] Butler, J. P., and Tsuda, A., 1997. “Effect of convective stretching and folding on aerosol mixing deep in the lung, assessed by approximate entropy”. *J. Applied Physiol.*, **83**(3), pp. 800–9.
- [156] Tsuda, A., Rogers, R. A., Hydon, P. E., and Butler, J. P., 2002. “Chaotic mixing deep in the lung”. *Proc. Nat. Acad. Sci.*, **99**(15), pp. 10173–10178.
- [157] Sznitman, J., 2013. “Respiratory microflows in the pulmonary acinus”. *J. Biomech.*, **46**(2), pp. 284–98.
- [158] Haber, S., Yitzhak, D., and Tsuda, A., 2003. “Gravitational deposition in a rhythmically expanding and contracting alveolus”. *J. Applied Physiol.*, **95**(2), pp. 657–71.
- [159] Kumar, H., Tawhai, M. H., Hoffman, E. A., and Lin, C.-L., 2009. “The effects of geometry on airflow in the acinar region of the human lung”. *J. Biomech.*, **42**(11), pp. 1635 – 1642.
- [160] Semmler-Behnke, M., Kreyling, W. G., Schulz, H., Takenaka, S., Butler, J. P., Henry, F. S., and Tsuda, A., 2012. “Nanoparticle delivery in infant lungs”. *Proc. Nat. Acad. Sci. USA*, **109**, pp. 5092–5097.
- [161] Arrieta, J., Cartwright, J. H. E., Gouillart, E., Piro, N., Piro, O., and Tuval, I., 2015. “Geometric mixing, peristalsis, and the geometric phase of the stomach”. *PLOS ONE*, **10**(7), pp. 1–17.
- [162] Bornhorst, G. M., 2017. “Gastric mixing during food digestion: Mechanisms and applications”. *Annual Review of Food Science and Technology*, **8**(1), pp. 523–542.
- [163] Beaumont, F., Liger-Belair, G., and Polidori, G., 2013. “Convective mass transfer in a champagne glass”. In *Mass Transfer - Advances in Sustainable Energy and Environment Oriented Numerical Modeling*, H. Nakajima, ed. InTech, Rijeka, ch. 12.
- [164] Bringer, M. R., Gerds, C. J., Song, H., Tice, J. D., and Ismagilov, R. F., 2004. “Microfluidic systems for chemical kinetics that rely on chaotic mixing in droplets”. *Phil. Trans. A*, **362**(1818), pp. 1087–104.
- [165] Stone, Z. B., and Stone, H. a., 2005. “Imaging and quantifying mixing in a model droplet micromixer”. *Phys. Fluids*, **17**(6), p. 063103.
- [166] Kintses, B., van Vliet, L. D., Devenish, S. R., and Hollfelder, F., 2010. “Microfluidic droplets: new integrated workflows for biological experiments”. *Curr. Opin. Chem. Biol.*, **14**(5), pp. 548 – 555.
- [167] Levin, I., and Aharoni, A., 2012. “Evolution in microfluidic droplet”. *Chemistry & Biology*, **19**(8), pp. 929 – 931.
- [168] Lagus, T. P., and Edd, J. F., 2013. “A review of the theory, methods and recent applications of high-throughput single-cell droplet microfluidics”. *J. Phys. D*, **46**(11), p. 114005.
- [169] Vitor, M. T., Sipoli, C. C., and Torre, L. G. D. L., 2015. “Droplet-based microfluidic systems for production and transfection in vitro of non-viral vectors for gene delivery”. *Res. Rev.: J. Pharmacy Pharmaceut. Sci.*, **4**, pp. 1–17.
- [170] Fair, R. B., 2007. “Digital microfluidics: is a true lab-on-a-chip possible?”. *Microfluid. Nanofluid.*, **3**(3), pp. 245–281.
- [171] Pollack, M. G., Pamula, V. K., Srinivasan, V., and Eckhardt, A. E., 2011. “Applications of electrowetting-based digital microfluidics in clinical diagnostics”. *Exp. Rev. Molec. Diagnos.*, **11**(4), pp. 393–407.
- [172] Choi, K., Ng, A. H., Fobel, R., and Wheeler, A. R., 2012. “Digital microfluidics”. *Annu. Rev. Analyt. Chem.*, **5**(1), pp. 413–440.
- [173] Jiang, L., Zeng, Y., Zhou, H., Qu, J.-Y., and Yao, S., 2012. “Visualizing millisecond chaotic mixing dynamics in microdroplets: A direct comparison of experiment and simulation”. *Biomicrofluid.*, **6**, pp. 012810–012810–12.
- [174] Kroujiline, D., and Stone, H. A., 1999. “Chaotic streamlines in steady bounded three-dimensional

- Stokes flows”. *Phys. D*, **130**, pp. 105–132.
- [175] Bajer, K., and Moffatt, H. K., 1990. “On a class of steady confined Stokes flows with chaotic streamlines”. *J. Fluid Mech.*, **212**, pp. 337–363.
- [176] Stone, H. A., Nadim, A., and Strogatz, S. H., 1991. “Chaotic streamlines inside drops immersed in steady stokes flows”. *J. Fluid Mech.*, **232**, pp. 629–646.
- [177] Chang, L. S., Carleson, T. E., and Berg, J. C., 1982. “Heat and mass transfer to a translating drop in an electric field”. *International Journal of Heat and Mass Transfer*, **25**(7), pp. 1023 – 1030.
- [178] Ward, T., and Homsy, G. M., 2003. “Electrohydrodynamically driven chaotic mixing in a translating drop. II. Experiments”. *Phys. Fluids*, **15**(10), pp. 2987–2994.
- [179] Ward, T., and Homsy, G. M., 2006. “Chaotic streamlines in a translating drop with a uniform electric field”. *J. Fluid Mech.*, **547**, pp. 215–230.
- [180] Xu, X., and Homsy, G. M., 2007. “Three-dimensional chaotic mixing inside drops driven by a transient electric field”. *Phys. Fluids*, **19**(1), p. 013102.
- [181] Grigoriev, R. O., Schatz, M. F., and Sharma, V., 2006. “Chaotic Mixing In Microdroplets”. *Lab Chip*, **6**, pp. 1369–1372.
- [182] Vainchtein, D. L., Widloski, J., and Grigoriev, R. O., 2007. “Mixing Properties of Steady Flow in Thermocapillary Driven Droplets”. *Phys. Fluids*, **19**, p. 67102.
- [183] Wu, F., Vainchtein, D., and Ward, T., 2015. “Perturbation analysis of steady and unsteady electrohydrodynamic chaotic advection inside translating drops”. *Phys. Rev. E*, **92**, p. 023030.
- [184] Mugele, F., Baret, J.-C., and Steinhauser, D., 2006. “Microfluidic mixing through electrowetting-induced droplet oscillations”. *Appl. Phys. Lett.*, **88**(20), p. 204106.
- [185] Mugele, F., Staicu, A., Bakker, R., and van den Ende, D., 2011. “Capillary Stokes drift: a new driving mechanism for mixing in AC-electrowetting.”. *Lab Chip*, **11**(12), pp. 2011–6.
- [186] Alghane, M., Fu, Y. Q., Chen, B. X., Li, Y., Desmulliez, M. P. Y., and Walton, A. J., 2011. “Streaming phenomena in microdroplets induced by Rayleigh surface acoustic wave”. *J. Appl. Phys.*, **109**(11), p. 114901.
- [187] Debon, A. P., Wootton, R. C., S., K., and Elvira, 2015. “Droplet confinement and leakage: Causes, underlying effects, and amelioration strategies”. *Biomicrofluidics*, **9**(2), p. 024119.
- [188] Zhu, P., Kong, T., Lei, L., Tian, X., Kang, Z., and Wang, L., 2016. “Droplet breakup in expansion-contraction microchannels”. *Scientif. Rep.*, **6**, p. 21527.
- [189] Branicki, M., and Wiggins, S., 2009. “An adaptive method for computing invariant manifolds in non-autonomous, three-dimensional dynamical systems”. *Phys. D*, **238**(16), pp. 1625–1657.
- [190] Ide, K., Small, D., and Wiggins, S., 2002. “Distinguished hyperbolic trajectories in time-dependent fluid flows: analytical and computational approach for velocity fields defined as data sets”. *Nonlin. Process. Geophys.*, **9**(3/4), pp. 237–263.
- [191] Quinlan, M. E., 2016. “Cytoplasmic streaming in the drosophila oocyte”. *Annu. Rev. Cell Develop. Biol.*, **32**(1), pp. 173–195.
- [192] Bonfiglio, A., Repetto, R., Siggers, J. H., and Stocchino, A., 2013. “Investigation of the motion of a viscous fluid in the vitreous cavity induced by eye rotations and implications for drug delivery.”. *Phys. in Med. Biol.*, **58**(6), pp. 1969–1982.
- [193] Maroto, J. A., Pérez-Munuzuri, V., and Romero-Cano, M. S., 2007. “Introductory analysis of Bénard–Marangoni convection”. *Eur. J. Phys.*, **28**(2), p. 311.
- [194] Dentz, M., Icardi, M., and Hidalgo, J. J., 2018. “Mechanisms of dispersion in a porous medium”. *J. Fluid Mech.*, **841**, pp. 851–882.
- [195] Hare, C., 1994. *Protective Coatings: Fundamentals of Chemistry and Composition*. SSPC (Series). Technology Publishing Company.
- [196] Bassou, N., and Rharbi, Y., 2009. “Role of Bénard–Marangoni instabilities during solvent evaporation in polymer surface corrugations”. *Langmuir*, **25**(1), pp. 624–632.
- [197] Saranjam, N., Chandra, S., Mostaghimi, J., Fan, H., and Simmer, J., 2016. “Orange peel formation due to surface tension-driven flows within drying paint films”. *J. Coat. Techn. Res.*, **13**(3), pp. 413–426.
- [198] Bunz, U. H. F. “Breath figures as a dynamic templating method for polymers and nanomaterials”. *Advanced Materials*, **18**(8), pp. 973–989.
- [199] Escalé, P., Rubatat, L., Billon, L., and Save, M., 2012. “Recent advances in honeycomb-structured porous polymer films prepared via breath figures”. *Eur. Polymer J.*, **48**(6), pp. 1001 – 1025.
- [200] Muñoz-Bonilla, A., Fernández-García, M., and Rodríguez-Hernández, J., 2014. “Towards hierarchically ordered functional porous polymeric surfaces prepared by the breath figures approach”. *Prog. Polymer Sci.*, **39**(3), pp. 510 – 554.
- [201] Zhang, A., Bai, H., and Li, L., 2015. “Breath figure: A nature-inspired preparation method for ordered porous films”. *Chem. Rev.*, **115**(18), pp. 9801–9868.
- [202] Deng, Y., Wang, Q., Yuan, Y., and Huang, J., 2015. “Vividly colorful hybrid perovskite solar cells by doctor-blade coating with perovskite photonic nanostructures”. *Mater. Horiz.*, **2**, pp. 578–583.
- [203] Kelley, D. H., and Sadoway, D. R., 2014. “Mixing in a liquid metal electrode”. *Phys. Fluids*, **26**(5), p. 057102.
- [204] Weber, N., Galindo, V., Priede, J., Stefani, F., and Weier, T., 2015. “The influence of current collectors on Taylor instability and electro-vortex flows in liquid metal batteries”. *Phys. Fluids*, **27**(1), p. 014103.
- [205] Kelley, D. H., and T, T. W., 2018. “Fluid mechanics of liquid metal batteries”. *Appl. Mech. Rev.*, **70**, pp. 020801–1 – 020801–23.

- [206] Pardo, P., Deydier, A., Anxionnaz-Minvielle, Z., Rougé, S., Cabassud, M., and Cognet, P., 2014. “A review on high temperature thermochemical heat energy storage”. *Renew. Sust. Energy Rev.*, **32**, pp. 591 – 610.
- [207] Therriault, D., White, S. R., and Lewis, J. a., 2003. “Chaotic mixing in three-dimensional microvascular networks fabricated by direct-write assembly”. *Nature materials*, **2**(4), pp. 265–71.
- [208] Boomsma, K., Poulikakos, D., and Zwick, F., 2003. “Metal foams as compact high performance heat exchangers”. *Mech. Materials*, **35**(12), pp. 1161 – 1176.
- [209] Hugo, J.-M., Brun, E., and Topin, F., 2011. “Metal foam effective transport properties”. In *Evaporation, Condensation and Heat transfer*, A. Ahsan, ed. IntechOpen, Rijeka, ch. 14.
- [210] Zhao, C., 2012. “Review on thermal transport in high porosity cellular metal foams with open cells”. *Int. J. Heat Mass Trans.*, **55**(13), pp. 3618 – 3632.
- [211] Manneville, P., 2006. *Rayleigh-Bénard Convection: Thirty Years of Experimental, Theoretical, and Modeling Work*. Springer, New York, NY, pp. 41–65.
- [212] Dykhne, A. M., Isichenko, M. B., and Horton, W., 1994. “Diffusion in laminar rayleigh-bénard convection: Boundary layers versus boundary tubes”. *Phys. Fluids*, **6**(7), pp. 2345–2351.
- [213] Medale, M., and Cerisier, P., 2007. “Study of passive dye dispersion in convective hexagonal pattern”. *Journal of Physics: Conference Series*, **64**, p. 12002.
- [214] Sano, O., 1993. “Convection diffusion in hexagonal Rayleigh-Bénard cell”. *J. Phys. Soc. Japan*, **62**(4), pp. 1202–1208.
- [215] Lester, D. R., Metcalfe, G., and Trefry, M. G., 2013. “Is chaotic advection inherent to porous media flow?”. *Phys. Rev. Lett.*, **111**, p. 174101.
- [216] Lester, D., Dentz, M., and LeBorgne, T., 2016. “Chaotic mixing in three-dimensional porous media”. *J. Fluid Mech.*, **803**, pp. 144–174.
- [217] Lester, D., Trefry, M., and Metcalfe, G., 2016. “Chaotic advection at the pore scale: Mechanisms, upscaling and implications for macroscopic transport”. *Adv. Water Resour.*, **97**, pp. 175 – 192.
- [218] Surana, A., Grunberg, O., and Haller, G., 2006. “Exact theory of three-dimensional flow separation. part 1. steady separation”. *J. Fluid Mech.*, **564**, pp. 57–103.
- [219] Bear, J., 1972. *Dynamics of Fluids in Porous Media*. Dover Civil and Mechanical Engineering Series. Dover.
- [220] Steelman, C. M., Klazinga, D. R., Cahill, A. G., Endres, A. L., and Parker, B. L., 2017. “Monitoring the evolution and migration of a methane gas plume in an unconfined sandy aquifer using time-lapse gpr and ert”. *J. Contam. Hydrol.*, **205**, pp. 12 – 24.
- [221] Bagtzoglou, A. C., and Oates, P. M., 2007. “Chaotic advection and enhanced groundwater remediation”. *J. Mat. Civil Engng*, **19**(1), pp. 75–83.
- [222] Trefry, M. G., Lester, D. R., Metcalfe, G., Ord, A., and Regenauer-Lieb, K., 2012. “Toward enhanced subsurface intervention methods using chaotic advection”. *J. Contam. Hydrol.*, **127**(1), pp. 15–29.
- [223] Piscopo, A. N., Neupauer, R. M., and Mays, D. C., 2013. “Engineered injection and extraction to enhance reaction for improved in situ remediation”. *Water Resour. Res.*, **49**(6), pp. 3618–3625.
- [224] Neupauer, R. M., Meiss, J. D., and Mays, D. C., 2014. “Chaotic advection and reaction during engineered injection and extraction in heterogeneous porous media”. *Water Resources Res.*, **50**(2), pp. 1433–1447.
- [225] Varghese, S., Speetjens, M. F. M., and Trieling, R. R., 2017. “Lagrangian transport and chaotic advection in two-dimensional anisotropic systems”. *Trans. Por. Med.*, pp. 1–22.
- [226] Rodriguez-Escales, P., Fernandez-Garcia, D., Drechsel, J., Folch, A., and Sanchez-Vila, X., 2017. “Improving degradation of emerging organic compounds by applying chaotic advection in managed aquifer recharge in randomly heterogeneous porous media”. *Water Resources Res.*, **53**(5), pp. 4376–4392.
- [227] Speetjens, M. F. M., Varghese, S., and Trieling, R. R., 2019. “Lagrangian approach to analysis and engineering of two generic transport problems in enhanced subsurface flows”. *J. Contam. Hydrol. (in press)*.
- [228] Monroe, J., and Wicander, R., 1992. *Physical Geology: Exploring the Earth*. West Publishing Company.
- [229] Zhong, S., Zhang, N., Li, Z.-X., and Roberts, J. H., 2007. “Supercontinent cycles, true polar wander, and very long-wavelength mantle convection”. *Earth Planet. Sci. Lett.*, **261**(3), pp. 551 – 564.
- [230] Cramer, F., Tackley, P. J., Meilick, I., Gerya, T. V., and Kaus, B. J. P., 2012. “A free plate surface and weak oceanic crust produce single-sided subduction on earth”. *Geophys. Res. Lett.*, **39**, p. L03306.
- [231] Reichold, J., Stampanoni, M., Keller, A. L., Buck, A., Jenny, P., and Weber, B., 2009. “Vascular graph model to simulate the cerebral blood flow in realistic vascular networks”. *J. Cereb. Blood Flow Metab.*, **29** **8**, pp. 1429–43.
- [232] Deb, P., Sharma, S., and Hassan, K., 2010. “Pathophysiologic mechanisms of acute ischemic stroke: An overview with emphasis on therapeutic significance beyond thrombolysis”. *Pathophysiology*, **17**(3), pp. 197 – 218.
- [233] Spill, F., Reynolds, D. S., Kamm, R. D., and Zaman, M. H., 2016. “Impact of the physical microenvironment on tumor progression and metastasis”. *Curr. Opin. Biotechnol.*, **40**, pp. 41 – 48.
- [234] Ghaffarizadeh, A., Friedman, S. H., and Macklin, P., 2016. “BioFVM: an efficient, parallelized diffusive transport solver for 3-D biological simulations”. *Bioinformatics*, **32**(8), pp. 1256–1258.
- [235] Macklin, P., Frieboes, H. B., Sparks, J. L., Ghaffarizadeh, A., Friedman, S. H., Juarez, E. F., Jonckheere, E., and Mumenthaler, S. M., 2016. *Progress Towards Computational 3-D Multicellular Systems Biology*. Springer International Publishing, Cham,

- pp. 225–246.
- [236] Reorowicz, P., Obidowski, D., Klosinski, P., Szubert, W., Stefanczyk, L., and Jozwik, K., 2014. “Numerical simulations of the blood flow in the patient-specific arterial cerebral circle region”. *J. Biomech.*, **47**(7), pp. 1642 – 1651.
- [237] Rejniak, K., 2016. *Systems Biology of Tumor Microenvironment: Quantitative Modeling and Simulations*. Advances in Experimental Medicine and Biology. Springer International Publishing.
- [238] Jonášová, A., and Vimmr, J., 2018. “Noninvasive assessment of carotid artery stenoses by the principle of multiscale modelling of non-newtonian blood flow in patient-specific models”. *Appl. Math. Comput.*, **319**, pp. 598 – 616.
- [239] Guckenheimer, J., and Holmes, P., 1983. *Nonlinear Oscillations, Dynamical Systems and Bifurcations of Vector Fields*. Springer, New York.
- [240] Chong, M. S., Perry, A. E., and Cantwell, B. J., 1990. “A General Classification of Three-Dimensional Flows”. *Phys. Fluids*, **2**(5), pp. 765–777.
- [241] Verhulst, F., 2006. *Nonlinear Differential Equations and Dynamical Systems*. Universitext. Springer Berlin Heidelberg.
- [242] Aref, H., 1983. “Integrable, chaotic, and turbulent vortex motion in two-dimensional flows”. *Annu. Rev. Fluid Mech.*, **15**(1), pp. 345–389.
- [243] Ott, E., 2002. *Chaos in Dynamical Systems*. Cambridge University Press, Cambridge.
- [244] Arfken, G. B., and Weber, H. J., 1995. *Mathematical Methods for Physicists*. Academic Press, San Diego.
- [245] Bajer, K., 1994. “Hamiltonian formulation of the equations of streamlines in three-dimensional steady flows”. *Chaos*, **4**, pp. 895–912.
- [246] Mezić, I., and Wiggins, S., 1994. “On the integrability and perturbation of three-dimensional fluid flows with symmetry”. *J. Nonlin. Sci.*, **4**, pp. 157–194.
- [247] Mezić, I., 2009. *Lectures on Mixing and Dynamical Systems*. Springer Vienna, Vienna, pp. 35–108.
- [248] Cartwright, J. H. E., Feingold, M., and Piro, O., 1994. “Passive scalars and three-dimensional Liouvillean maps”. *Physica D*, **76**, pp. 22–33.
- [249] Feingold, M., Kadanoff, L. P., and Piro, O., 1988. “Passive scalars, three-dimensional volume-preserving maps and chaos”. *J. Stat. Phys.*, **50**, p. 529.
- [250] Abraham, R. H., and Shaw, C. D., 1982. *Dynamics: The Geometry of Behavior (Part Three: Global Behavior)*. Aerial Press, Santa Cruz.
- [251] Beigie, D., Leonard, A., and Wiggins, S., 1994. “Invariant manifold template for chaotic advection”. *Chaos*, **4**, pp. 749–868.
- [252] Holmes, P., 1984. “Some remarks on chaotic particle paths in time-periodic, three-dimensional swirling flows”. *Contemp. Math.*, **28**, pp. 393–404.
- [253] Cheng, C. Q., and Sun, Y. S., 1990. “Existence of invariant tori in three-dimensional measure preserving mappings”. *Celest. Mech.*, **47**, pp. 275–292.
- [254] Cheng, C. Q., and Sun, Y. S., 1990. “Existence of periodically invariant curves in three-dimensional measure-preserving mappings”. *Celest. Mech.*, **47**, pp. 293–303.
- [255] Smith, L. D., Rudman, M., Lester, D. R., and Metcalfe, G., 2017. “Localized shear generates three-dimensional chaos”. *Chaos*, **27**, p. 043102.
- [256] Sen, M., and Chang, H., 1994. Process and apparatus for enhancing in-tube heat transfer by chaotic mixing, May 17. US Patent 5,311,932.
- [257] Peerhossaini, H., Le, G., and Castelain, C., 1994. Chaotic convection effect mixing exchanger, June 9. WO Patent App. PCT/FR1993/001,167.
- [258] Mackley, M., Skelton, R., and Smith, K., 1994. Processing of mixtures by means of pulsations, Oct. 13. WO Patent App. PCT/GB1994/000,641.
- [259] Logan, J., 1994. Fluid mixing device, July 5. US Patent 5,326,164.
- [260] Kwon, T., and Kim, S., 1994. Chaos screw for single screw extruder. WO1995030530A1.
- [261] Evans, J., Liepmann, D., and Pisano, A., 2000. Apparatus and method for planar laminar mixing, June 21. EP Patent App. EP19,980,903,660.
- [262] Hobbs, D., and Muzzio, F., 1998. “Reynolds number effects on laminar mixing in the Kenics static mixer”. *Chemical Engineering Journal*, **70**(2), pp. 93–104.
- [263] Ziemlewski, J., 2010. “Radical designs boost resource efficiency”. *AICHE – CEP Magazine (July issue)*, pp. 4–9.
- [264] Metcalfe, G., and Rudman, M., 2006. Fluid mixer utilizing viscous drag, Oct. 17. US Patent 7,121,714.
- [265] Metcalfe, G., and Rudman, M., 2010. Heat exchange method and apparatus utilizing chaotic advection in a flowing fluid to promote heat exchange, Apr. 6. US Patent 7,690,833.
- [266] Peacock, T., and Haller, G., 2013. “Lagrangian coherent structures: The hidden skeleton of fluid flows”. *Physics Today*, **66**(2), p. 41.
- [267] Froyland, G., Santitissadeekorn, N., and Monahan, A., 2010. “Transport in time-dependent dynamical systems: Finite-time coherent sets”. *Chaos*, **20**, p. 043116.
- [268] Mosovsky, B. A., Speetjens, M. F. M., and Meiss, J. D., 2013. “Finite-time transport in volume-preserving flows”. *Phys. Rev. Lett.*, **110**, p. 214101.
- [269] Mitchell, K. A., and Mahoney, J. R., 2012. “Invariant manifolds and the geometry of front propagation in fluid flows”. *Chaos*, **22**, p. 037104.
- [270] Gowen, S., and Solomon, T., 2015. “Experimental studies of coherent structures in an advection-reaction-diffusion system”. *Chaos*, **25**, p. 087403.
- [271] Speetjens, M. F. M., 2012. “A generalised Lagrangian formalism for thermal analysis of laminar convective heat transfer”. *Int. J. Therm. Sci.*, **61**, pp. 79–93.
- [272] Balasuriya, S., Ouellette, N. T., and Rypina, I. I., 2018. “Generalized Lagrangian coherent structures”. *Physica D: Nonlinear Phenomena*, **372**, pp. 31 – 51.
- [273] Smith, L. D., Rudman, M., Lester, D. R., and Metcalfe, G., 2017. “Impact of discontinuous deformation

upon the rate of chaotic mixing”. *Physical Review E*, **95**, p. 022213.

- [274] Smith, L. D., Umbanhowar, P. B., Ottino, J. M., and Lueptow, R. M., 2017. “Mixing and transport from combined stretching-and-folding and cutting-and-shuffling”. *Phys. Rev. E*, **96**, p. 042213.